

CERN-SPSC-2005-013

SPSC-P-326

11.6.2005

**Proposal to Measure  
the Rare Decay  $K^+ \rightarrow \pi^+ \nu \bar{\nu}$  at the CERN SPS**

**CERN, Dubna, Ferrara, Florence, Frascati,  
Mainz, Merced, Moscow, Naples, Perugia,  
Protvino, Pisa, Rome, Saclay, Sofia, Turin**

G. Anelli, A. Ceccucci\*, V. Falaleev, F. Formenti, A. Gonidec, B. Hallgren,  
P. Jarron, A. Kluge, M. Losasso, A. Norton, A. Placci, P. Riedler, G. Ruggiero, G. Stefanini  
**CERN**

S. Bazylev, P. Frabetti, E. Goudzovski, D. Gurev, V. Kekelidze, D. Madigozhin,  
N. Molokanova, R. Pismennyy, Y. Potrebenikov, A Zinchenko

**Dubna**

W. Baldini, A. Cotta Ramusino, P. Dalpiaz, C. Damiani, A. Gianoli,  
M. Martini, F. Petrucci, M. Savrié, M. Scarpa, H. Wahl

**Ferrara**

A. Bizzeti, E. Iacopini, M. Lenti

**Florence**

A. Antonelli, M. Moulson, T. Spadaro

**Frascati**

S. Gninenko, E. Guschin

**INR, Moscow**

K. Kleinknecht, B. Renk, R. Wanke

**Mainz**

R. Winston

**Merced**

F. Ambrosino, C. Di Donato, M. Napolitano, G. Saracino

**Naples**

G. Anzivino, P. Cenci, M. Pepe, M. Piccini

**Perugia**

A. Bigi, R. Casali, G. Collazuol, F. Costantini, L. Fiorini, L. Di Lella, N. Doble,  
R. Fantechi, S. Giudici, I. Mannelli, A. Michetti,  
G.M. Pierazzini, M. Sozzi

**Pisa**

G. Britvich, V. Kurshtetsov, A. Kushnirenko, L. Landsberg , V. Molchanov, V.Obraztsov,  
A. Soldatov, V. Rykalin, O. Tchikilev, O. Yushchenko

**Protvino**

N. Cabibbo, G. D'Agostini, E. Leonardi, M. Serra, P. Valente

**Rome I**

B. Peyaud, J. Derre

**Saclay**

C. Cheshkov, P. Hristov, L. Litov, S. Stoynev

**Sofia**

C. Biino, F. Marchetto, G. Mazza, A. Rivetti

**Turin**

---

\*Contact Person, email address: [augusto.ceccucci@cern.ch](mailto:augusto.ceccucci@cern.ch)

# Contents

<b>1</b>	<b>Introduction</b>	<b>4</b>
<b>2</b>	<b>Physics Motivation</b>	<b>7</b>
2.1	The $K \rightarrow \pi\nu\bar{\nu}$ decays . . . . .	7
2.2	Other physics opportunities . . . . .	10
<b>3</b>	<b>Experimental Strategy</b>	<b>11</b>
<b>4</b>	<b>The Beam for the <math>K^+ \rightarrow \pi^+\nu\bar{\nu}</math> Experiment</b>	<b>16</b>
4.1	Rationale . . . . .	16
4.1.1	Choice of Accelerator and Primary Proton Momentum . . . . .	16
4.1.2	Comparison with the FNAL Main Injector . . . . .	16
4.1.3	Choice of a Positive Kaon Beam . . . . .	17
4.1.4	Choice of Beam Momentum . . . . .	17
4.2	High-Intensity $K^+$ Beam . . . . .	17
4.2.1	Beam Design and Layout . . . . .	17
4.2.2	Beam Parameters and Estimated Performance . . . . .	19
4.3	Cost estimate of the new beam line . . . . .	28
4.3.1	SPS Availability and Scheduling . . . . .	28
4.4	The Decay Vacuum Tank . . . . .	29
<b>5</b>	<b>Detectors</b>	<b>30</b>
<b>6</b>	<b>CEDAR</b>	<b>32</b>
<b>7</b>	<b>GIGATRACKER</b>	<b>35</b>
7.1	Specification of the time resolution . . . . .	35
7.2	The fast silicon pixel detector: SPIBES . . . . .	37
7.3	Front-end Electronics and Sensors . . . . .	41
7.4	Micromegas-type TPC . . . . .	45
<b>8</b>	<b>PHOTON VETOES</b>	<b>47</b>
8.1	Considerations about the inefficiency . . . . .	48

8.2	Large angle vetoes (ANTI) . . . . .	51
8.3	Geometry of large angle vetoes . . . . .	53
8.4	Mechanical design . . . . .	53
8.4.1	An alternative structure . . . . .	55
8.4.2	Readout . . . . .	58
8.5	Cost estimation . . . . .	58
8.6	Liquid Krypton calorimeter . . . . .	58
8.6.1	Estimate of the inefficiency . . . . .	59
8.6.2	New readout . . . . .	59
8.6.3	Upgrade of the cryogenics slow control . . . . .	60
8.7	Small angle vetoes . . . . .	60
8.7.1	Geometry of the detectors . . . . .	61
8.7.2	Mechanical design . . . . .	62
8.7.3	Readout . . . . .	63
8.7.4	Costs . . . . .	63
<b>9</b>	<b>STRAW TRACKER</b>	<b>63</b>
<b>10</b>	<b>RICH</b>	<b>67</b>
<b>11</b>	<b>CHARGED HODOSCOPE</b>	<b>68</b>
<b>12</b>	<b>MAMUD</b>	<b>70</b>
<b>13</b>	<b>Trigger and DAQ</b>	<b>75</b>
13.1	Detector Control System . . . . .	87
<b>14</b>	<b>Resources and Schedule</b>	<b>88</b>

# 1 Introduction

We propose to measure the very rare kaon decay  $K^+ \rightarrow \pi^+ \nu \bar{\nu}$  at the CERN SPS to make a decisive test of the Standard Model by extracting a 10% measurement of the CKM parameter  $|V_{td}|$ . The physics motivation is given in Section 2. The proposed experiment aims to collect about 80  $K^+ \rightarrow \pi^+ \nu \bar{\nu}$  events for a  $10^{-10}$  Branching Ratio, with a signal to background ratio ( $S/B$ ) of 10:1 in two years of data taking. With respect to the Letter of Intent presented at the SPSC meeting held in Villars we have:

1. chosen to build a straw-tracker, operated in vacuum, instead of traditional drift chambers to minimise the effects due to the multiple scattering introduced by the vacuum window and the helium placed between the tracking stations,
2. envisaged the addition of a RICH counter to the layout to control better the backgrounds coming from  $K^+ \rightarrow \mu^+\nu$  and its associated radiative decay.

We propose to use 400 GeV/c protons from the SPS to perform the experiment. The advantage of using a high energy proton machine is two-fold: the cross section to make kaons increases as a function of proton energy so that fewer protons are needed to produce the same kaon flux, thus reducing the non-kaon-related accidental activity. In addition, the higher kaon energy leads to easier photon detection which simplifies the suppression of the backgrounds originating from  $K^+ \rightarrow \pi^+\pi^0$ : for example, employing a 75 GeV/c kaon beam and limiting the momentum of the reconstructed  $\pi^+$  to 35 GeV/c, there are at least 40 GeV of electro-magnetic energy deposited into the photon vetoes. This reduces significantly the probability that both photons from the  $\pi^0$  decay are left undetected because of photo-nuclear reactions and detector inefficiencies. The disadvantage of high energy protons and, consequently, of a high energy secondary beam, is that the pions and the protons cannot be efficiently separated from kaons. The consequence is that the upstream detectors which measure the momentum and the direction of the kaons are exposed to a particle flux about 17 times larger than the useful (kaon) one. It is important to point out that the magnetic spectrometers and the other principal detectors placed downstream of the decay region do not suffer from the same limitation because:

1. The protons and the undecayed kaons and pions are kept in vacuum without illuminating the detector elements.
2. The muons from pion decays are mostly contained in the non-instrumented region of the straw tracker because of the small transverse momentum released by the pion decay.

The experiment is not limited by the flux of protons that can be delivered by the SPS. We assume a duty cycle of the SPS similar to the one available during the 2003 and 2004 data taking. There are several challenging aspects for this experiment. They include:

- Performing tracking at 1 GHz total rate,  $\sim 60$  MHz/cm<sup>2</sup>, within a minimal material budget, with minimal detector dead-time and excellent time resolution.

- Achieving positive kaon identification in a high rate environment by means of a differential Cherenkov counter insensitive to pions and protons with minimal accidental mistagging.
- Constructing and operating hermetic photon vetoes to provide a  $\pi^0$  rejection of  $\sim 10^8$ .
- Achieving a muon rejection of at least  $10^5$  using a magnetised iron/scintillator detector.
- Achieve a two standard deviations  $\pi/\mu$  separation up to 35 GeV/c momentum by means of a RICH counter.
- Performing redundant measurement of the momentum of the incoming  $K^+$  and outgoing  $\pi^+$  for suppression of the tails in the reconstruction of the missing mass for two-body decays.
- Vetoing the charged particles coming from three- and four-body kaon decays.
- Minimising the accidental activity from non-kaon decays (e.g. muons from the production target and proton dump and tracks coming from pion and kaon decays occurring upstream of the decay region).

This experiment benefits from the existing infrastructure of the NA48 setup and an effort is made to reuse as much as possible of it in order to keep the overall cost at a reasonable level. Notably, we plan to re-use the NA48 liquid krypton electro-magnetic calorimeter (LKR) for photon vetoing and electron rejection.

It is important to place this initiative in the world context. So far the study of the decay  $K^+ \rightarrow \pi^+ \nu \bar{\nu}$  has only been performed with kaon decays at rest. BNL-AGS-E787 (E949) have collected data from 1995 until 1998 (2002) and have published [1] a measurement of the branching ratio  $BR(K^+ \rightarrow \pi^+ \nu \bar{\nu}) = 1.47^{+1.30}_{-0.89} \times 10^{-10}$  based on three events interpreted as signal. The follow-up experiment BNL-AGS-E949 [2] may collect more data in the future, possibly to reach 10 signal events. Plans to pursue further the decay-at-rest technique at J-PARC have been expressed [3]. As far as decay-in-flight is concerned, the CKM [4] Collaboration has proposed an experiment to measure 100  $K^+ \rightarrow \pi^+ \nu \bar{\nu}$  at the Fermilab Main Injector. The experiment was not ratified by the HEPAP P5 sub-panel for cost reasons. We have invited the proponents of that experiment to join our initiative at CERN to benefit from their long research and development in the subject of our approach. The experimental technique is described in Section 3 and in Section 4 we give a description of the kaon beam. The proposed detectors are described in Section 5-12 while a description of the trigger and

DAQ architecture is presented in Section 13. Cost estimations and the timeline of the experiment are summarised in Section 14.

## 2 Physics Motivation

### 2.1 The $K \rightarrow \pi\nu\bar{\nu}$ decays

The rare decays  $K^+ \rightarrow \pi^+\nu\bar{\nu}$  and  $K_L \rightarrow \pi^0\nu\bar{\nu}$  are extremely attractive processes to study the physics of flavour because they both are exceptionally clean modes. The hard (quadratic) GIM mechanism is active; thus, these decays are dominated by short-distance dynamics. Moreover, the short-distance amplitude is then governed by one single semileptonic operator whose hadronic matrix element can be determined experimentally by the semileptonic kaon decay; so the main hadronic uncertainties can be eliminated by experimental data. In view of these facts, the two rare kaon modes offer unique opportunities for testing the Standard Model and deepening our knowledge of the CKM matrix, which are complementary of those in  $B$  decays. Furthermore, they are extremely sensitive to possible new degrees of freedom beyond the Standard Model. For a recent review with extensive references of these decays and of the CKM matrix in general, see [5] and also [6].

At the quark level the two processes arise from the  $s \rightarrow d\nu\bar{\nu}$  process, which in the Standard Model originates from a combination of the  $Z_0$  penguin — the first two graphs in Figure 1 — and a double  $W$  exchange, the third graph.

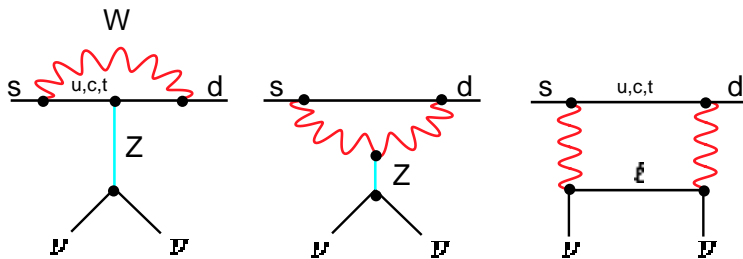


Figure 1: Graphs for  $s \rightarrow d\nu\bar{\nu}$  in the Standard Model

In these graphs the  $u, c, t$  quarks appear as internal lines. The hard GIM mechanism implies on the amplitude level  $A_q \sim m_q^2/m_W^2 V_{qs}^* V_{qd}$ ,  $q = u, c, t$ ; the top-quark contribution dominates, with a smaller contribution, in the case of the  $K^+ \rightarrow \pi^+\nu\bar{\nu}$  decay, from the charm. The up-quark contribution is in both cases negligible, so that  $s \rightarrow d\nu\bar{\nu}$  is essentially a short-distance process, well described by a Fermi-like coupling:

$$\mathcal{H}_{\text{eff}} = \sum_{l=e,\mu,\tau} \frac{G_l}{\sqrt{2}} (\bar{s}d)_{V-A} (\bar{\nu}_l \nu_l)_{V-A} , \quad (1)$$

where  $G_l$  is the effective coupling constant<sup>†</sup>. Given  $G_l$ , the branching ratios are directly related by isospin to that of the  $K_{e3}^+$  decay,

$$BR(K^+ \rightarrow \pi^+ \bar{\nu}\nu) = 6r_{K^+} BR(K^+ \rightarrow \pi^0 e^+ \nu) \frac{|G_l|^2}{G_F^2 |V_{us}|^2} \quad (2)$$

$$BR(K^0 \rightarrow \pi^0 \bar{\nu}\nu) = 6 \frac{\tau_{K_L}}{\tau_{K^+}} r_{K_L} BR(K^+ \rightarrow \pi^0 e^+ \nu) \frac{(\text{Im } G_l)^2}{G_F^2 |V_{us}|^2} ; \quad (3)$$

here,  $r_{K^+} = 0.901$  and  $r_{K_L} = 0.944$  are isospin-breaking corrections [7] that include phase-space and QED effects. The effective coupling constant  $G_l$  can be expressed as the sum of two contributions, the first arising from an internal top-quark line, the second from a charm quark:

$$G_l = \frac{\alpha G_F}{2\pi \sin^2 \Theta_W} [V_{ts}^* V_{td} X(x_t) + V_{cs}^* V_{cd} X_{NL}^l] , \quad (4)$$

where  $x_t = m_t^2/M_W^2$ . The  $X$  coefficients have been computed, including the leading QCD corrections [8] [9]. The top-quark contribution is precisely known, the main source of error arising from the uncertainty in the value of the  $t$  mass. The smaller contribution from the  $c$ -quark is affected by a larger error; averaging over the three neutrino species, the authors of ref. [5] quote the result

$$P_0(X) = \frac{1}{\lambda^4} \left[ \frac{2}{3} X_{NL}^e + \frac{1}{3} X_{NL}^\tau \right] = 0.42 \pm 0.06 , \quad (5)$$

which is reflected in a theoretical error of  $\sim 5 - 7\%$  on the determination of  $V_{td}$ . This makes the  $K^+ \rightarrow \pi^+ \bar{\nu}\nu$  one of the most attractive tools for the exploration of the unitarity triangle and also of possible degrees of freedom beyond the Standard Model — a member of a very short list of theoretically clean processes.

To evaluate the importance of eqs. (2), (3) and (4), we recall the composition of the CKM matrix in the popular Wolfenstein parametrization [10], whose accuracy is fully sufficient for the present discussion<sup>‡</sup>. The parameters  $A$  and  $\lambda$  can be defined to be positive:

$$V_{\text{CKM}} = \begin{pmatrix} V_{ud} & V_{us} & V_{ub} \\ V_{cd} & V_{cs} & V_{cb} \\ V_{td} & V_{ts} & V_{tb} \end{pmatrix} = \begin{pmatrix} 1 - \frac{\lambda^2}{2} & \lambda & A\lambda^3(\varrho - i\eta) \\ -\lambda & 1 - \frac{\lambda^2}{2} & A\lambda^2 \\ A\lambda^3(1 - \varrho - i\eta) & -A\lambda^2 & 1 \end{pmatrix} + \mathcal{O}(\lambda^4) \quad (6)$$

---

<sup>†</sup>There is a small difference between the couplings for  $\nu_\tau$  and  $\nu_{e,\mu}$ . Taking for  $G_l$  the average of the three implies a negligible (0.2%) error on the rates.

<sup>‡</sup>As discussed in [5], the final analysis would use a more exact parametrization and the modified Wolfenstein parameters  $\bar{\rho} = \rho(1 - \lambda^2/2)$  and  $\bar{\eta} = \eta(1 - \lambda^2/2)$ .

Comparing with eq. (4), we see that the charm-quark contribution to  $G_l$  depends on the well determined elements  $V_{cd}$ ,  $V_{cs}$ , and that this term is (in this approximation) a real number, so that it will not contribute to the  $K_L \rightarrow \pi^0 \nu \bar{\nu}$  decay. The theoretical prediction for this process is thus inherently cleaner than that for  $K^+ \rightarrow \pi^+ \nu \bar{\nu}$ .

Since in our approximation  $V_{ts} = -V_{cb}$ , and the latter is determined accurately from semileptonic  $B$  decays,  $|V_{cb}| = (41.5 \pm 0.8) \times 10^{-3}$ , a measurement of the branching ratios for the two decays leads to a determination of  $V_{td}$ , i.e. of the Wolfenstein parameters  $\rho, \eta$  that define the “unitarity triangle”, which is central in the analysis of the CKM matrix.

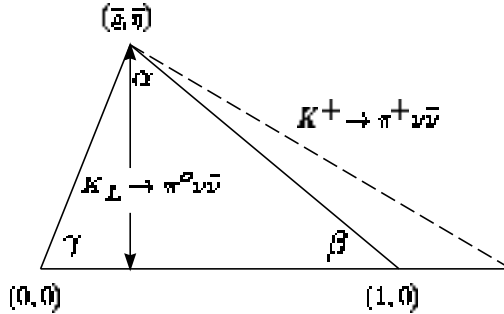


Figure 2: The unitarity triangle; the dashed line represents the measurement of  $K^+ \rightarrow \pi^+ \nu \bar{\nu}$ .

At present, the  $\beta$  angle (Figure 2, from [11]) has been determined accurately in  $B$ -factory experiments through the CP violation in  $B \rightarrow \psi K^0$  decays, a process that allows for a very clean theoretical analysis. The length of the right-hand side of the triangle is determined by the analysis of  $B^0 \bar{B}^0$  oscillations, whose theoretical interpretation requires lattice QCD.

The rate of  $K^+ \rightarrow \pi^+ \nu \bar{\nu}$  determines the absolute value of  $G_l$ , which is represented by the dashed segment in Figure 2. The displacement from 1 of the lower extremity of this segment is due to charm-quark contributions. A measurement of this rate would offer a valid alternative to the measurement of  $B^0 \bar{B}^0$  oscillations, but with different, possibly smaller, theoretical uncertainties. Combining the measurement of  $K^+ \rightarrow \pi^+ \nu \bar{\nu}$  with the existing data on  $\beta$  and  $B^0 \bar{B}^0$  oscillations offers [12] a significant test of the Standard Model.

The rate of  $K_L \rightarrow \pi^0 \nu \bar{\nu}$  offers a direct measurement of  $\eta$ , the height of the unitarity triangle. Its detection and measurement would establish the second example of direct CP violation after the measurement of  $\epsilon'/\epsilon$  in the  $K^0$  system, but with the advantage of a very clean theoretical analysis [13].

Besides their rich CKM phenomenology, the decays  $K_L \rightarrow \pi^0 \nu \bar{\nu}$  and  $K^+ \rightarrow \pi^+ \nu \bar{\nu}$  as loop-induced processes are very sensitive to new physics beyond the Standard Model. Thanks to

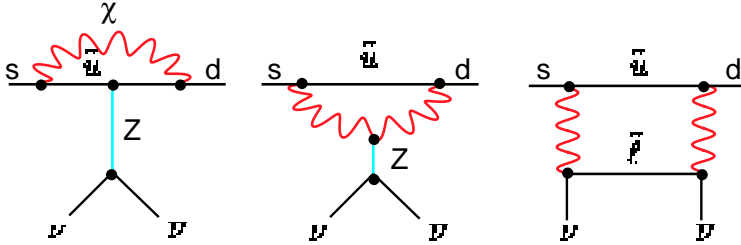


Figure 3: Graphs for  $s \rightarrow d\nu\bar{\nu}$  in supersymmetry

the cleanliness of the theoretical predictions, the measurement of these decays leads to very accurate constraints on any new physics model. Moreover, there is the possibility that these clean rare decay modes themselves lead to direct evidence of new physics when the measured decay rates are not compatible with the Standard Model. New effects in supersymmetric models, for example, can be induced through new box- and penguin-diagram contributions, which involve new particles such as charged Higgs or charginos and stops (Figure 3) that replace the  $W$  boson and the up-type quark of the SM (Figure 1). Analyses of possible post-Standard Model scenarios with direct new-physics contributions in the  $s \rightarrow d\nu\bar{\nu}$  amplitude or in  $B^0\bar{B}^0$  mixing are given in [12] and [6].

In summary: the rates of  $K^+ \rightarrow \pi^+\nu\bar{\nu}$  and  $K_L \rightarrow \pi^0\nu\bar{\nu}$  offer an accurate determination of the unitarity triangle, which is completely independent of that executed within the  $B$  system. Moreover,  $K^+ \rightarrow \pi^+\nu\bar{\nu}$  and  $K_L \rightarrow \pi^0\nu\bar{\nu}$  probe the short-distance behaviour of the Standard Model and are extremely sensitive to possible new degrees of freedom beyond the Standard Model.

## 2.2 Other physics opportunities

While we admit that the experiment focuses on just one compelling aim, we must stress that the new setup will allow us to produce many measurements on rare and medium-rare kaon decays. In particular, the good energy resolution for photons will allow us to study the radiative kaon decays with unprecedented precision. The study of these decays offers important input to the extraction of Chiral Perturbation Theory parameters. The situation is similar to the case of the NA48 experiment, which, in addition to accomplishing the measurement of  $\text{Re}(\varepsilon'/\varepsilon)$  for which it was designed, also led to many valuable by-products.

### 3 Experimental Strategy

The two undetectable neutrinos in the final state require the design of an experiment with redundant measurement of the event kinematics and hermetic vetoes to achieve a background rejection  $S/B \simeq 10$ . Particular care has to be taken to suppress the two-body decays  $K^+ \rightarrow \pi^+\pi^0$  and  $K^+ \rightarrow \mu^+\nu$  which have branching ratios up to  $10^{10}$  times larger than the expected signal. The reconstruction of the two body kinematics may suffer from reconstruction tails and backgrounds can originate if photons from  $K^+ \rightarrow \pi^+\pi^0$  are not detected or if muons from  $K^+ \rightarrow \mu^+\nu$  are mis-identified as pions. To suppress backgrounds from the two body decays, kinematics and Particle Identification (PID) have to be used in conjunction. Backgrounds from  $K^+$  three- and four-body decays are also potentially dangerous. For convenience we remind the reader of the most frequent  $K^+$  decay modes in Table 3, where they are reported together with the techniques intended to reject them. The kinematics of the most frequent  $K^+$  decays are compared to that of  $K^+ \rightarrow \pi^+\nu\bar{\nu}$  in Figure 3.

Decay Mode	Branching Ratio	Background Rejection
$K^+ \rightarrow \mu^+\nu$	63% (called $K_{\mu 2}$ )	$\mu$ PID, Two-Body Kinematics
$K^+ \rightarrow \pi^+\pi^0$	21%	Photon Veto, Two-Body Kinematics
$K^+ \rightarrow \pi^+\pi^+\pi^-$	6%	Charged Particle Veto, Kinematics
$K^+ \rightarrow \pi^+\pi^0\pi^0$	2%	Photon Veto, Kinematics
$K^+ \rightarrow \pi^0\mu^+\nu$	3% (called $K_{\mu 3}^+$ )	Photon Veto, $\mu$ PID
$K^+ \rightarrow \pi^0e^+\nu$	5% (called $K_{e3}^+$ )	Photon veto, $E/p$

Table 1: The most frequent  $K^+$  decay modes.

Two acceptance regions can be defined to be kinematically free from most of the frequent kaon decays. The kinematic of the decay under study is schematically sketched in Figure 5, where the momentum of the incoming kaon  $P_K$ , the momentum of the outgoing pion  $P_\pi$  and the angle between the mother and the daughter particle,  $\theta_{\pi K}$  are the only measurable quantities. It is convenient to use the squared missing mass variable,  $m_{miss}^2$ , defined under the hypothesis that the detected charged particle in the final state is a pion:

$$m_{miss}^2 \simeq m_K^2 \left( 1 - \frac{|P_\pi|}{|P_K|} \right) + m_\pi^2 \left( 1 - \frac{|P_K|}{|P_\pi|} \right) - |P_K||P_\pi|\theta_{\pi K}^2 \quad (7)$$

In Figure 6 the  $m_{miss}^2$  for the signal and the kaon decays with the largest branching ratios are shown for  $P_K = 75$  GeV/c. If resolution effects are ignored, the  $K^+ \rightarrow \pi^+\pi^0$  decay

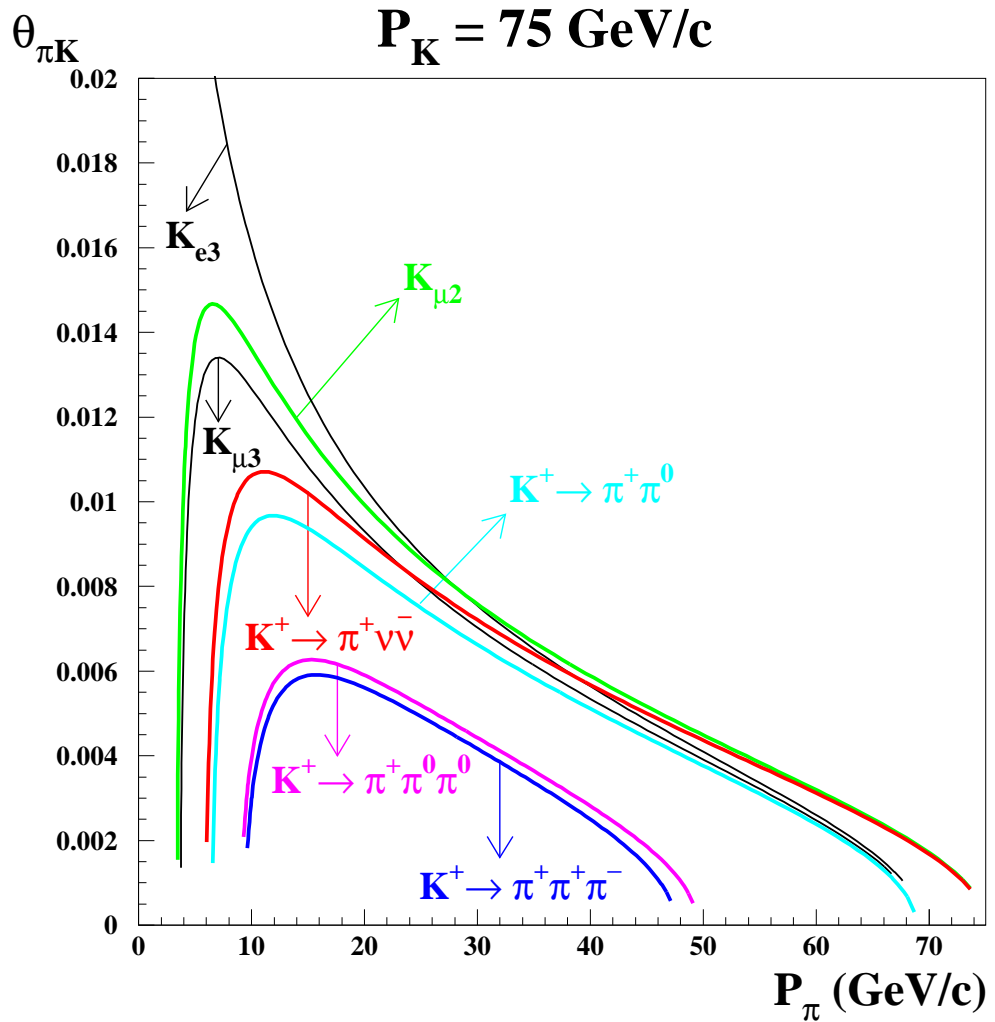


Figure 4: A comparison of the charged track angle-momentum relation for the most frequent  $K^+$  decays and  $K^+ \rightarrow \pi^+ \nu \bar{\nu}$ . For the three-body decays, the curves indicate the kinematical limit.

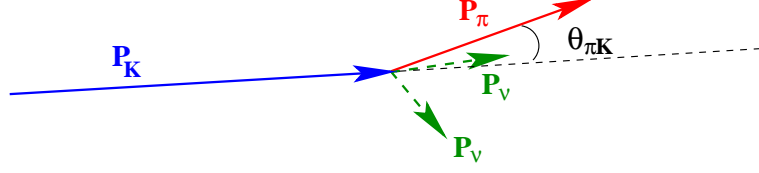


Figure 5: Kinematics of the decay under study.

is constrained to a line at  $m_{miss}^2 = m_{\pi^0}^2$ ; the  $m_{miss}^2$  of the three-pion decays shows a lower bound. The  $m_{miss}^2$  of  $K_{\mu 2}$  does not appear as a line at  $m_{miss}^2 = 0$  because it is wrongly evaluated, under the assumption that the track is a pion. For this decay the shape depends on the momentum of the particle in the final state and has  $m^2 = 0$  as the upper boundary. In conclusion, about 92% of the kaon decays are kinematically limited and their rejection relies on the reconstruction of the kinematics.

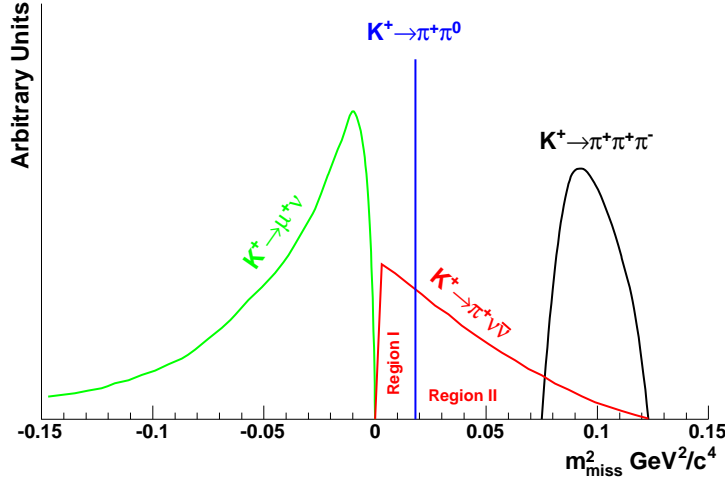


Figure 6: Distribution of the missing mass squared for the signal and the most frequent kaon decays.

Because the line of the  $K^+ \rightarrow \pi^+\pi^0$  decays lies within the signal region, we are forced to divide the signal acceptance into two different regions:

- Region I:  $0 < m_{miss}^2 < m_{\pi^0}^2 - (\Delta m)^2$
- Region II:  $m_{\pi^0}^2 + (\Delta m)^2 < m_{miss}^2 < \min m_{miss}^2(\pi^+\pi^+\pi^-) - (\Delta m)^2$

The  $\Delta m$  term depends on the  $m_{miss}^2$  resolution.

	$K^+ \rightarrow e^+ \pi^0 \nu$	$K^+ \rightarrow \mu^+ \nu \gamma$	$K^+ \rightarrow \pi^+ \pi^0 \gamma$
$BR$	$4.87 \times 10^{-2}$	$5.50 \times 10^{-3}$	$2.75 \times 10^{-4}$
Acceptance	13.4%	15.3%	17.9%
$\eta_\mu$	—	$10^{-5}$	—
$\eta_{\pi^0}$	$5 \times 10^{-8}$	—	$5 \times 10^{-8}$
$\eta_\gamma$	—	$2 \times 10^{-4}$	$10^{-3}$
$\eta_{\pi e}$	$10^{-3}$	—	—
$S/B$	30	5	4000

Table 2:  $S/B$  after selection for some backgrounds not kinematically constrained. The  $S/B$  are obtained for a signal acceptance of 10% and a signal branching ratio of  $10^{-10}$ . The  $K^+ \rightarrow \mu^+ \pi^0 \nu$  is negligible due to the simultaneous presence of  $\pi^0$  and  $\mu$ . Further suppression of the radiative  $K_{\mu 2}$  background given by the RICH has not been taken into account in this table.

Assuming the veto inefficiency on  $\pi^0$  to be of the order of  $10^{-8}$  and the muon veto inefficiency at the level of  $5 \times 10^{-6}$ , simulations have shown that  $S/B \geq 10$  with a signal acceptance larger than 10% can be achieved with  $(\Delta m)^2 \simeq 8 \times 10^{-3} \text{ GeV}^2/\text{c}^4$ . With a resolution on kaon momentum at the level of 0.3%, a resolution on the pion momentum better than 1% at 30 GeV/c and a resolution of  $\theta_{\pi K}$  of  $50 - 60 \mu\text{rad}$ , we will be able to achieve the  $m_{miss}^2$  resolution in order to reject kinematically the backgrounds at the required level.

The above specifications define the required performance of the upstream and downstream spectrometer, namely the Gigatracker and the Double Spectrometer.

Due to practical constraints on the achievable spatial resolution of the double spectrometer, the spatial resolution in the Gigatracker is not a critical issue: pixels of  $300 \mu\text{m} \times 200 \mu\text{m}$  give resolutions in kaon momentum and direction which contribute negligibly to  $m_{miss}^2$ .

A critical aspect of the experiment is that the high rate in the Gigatracker can lead to a situation in which a pion track measured in the downstream spectrometer is wrongly associated to a kaon candidate in the Gigatracker. When this happens, the kinematical rejection power is degraded. To avoid the combinatorial background, a very good time resolution of the Gigatracker is essential.

Semi-leptonic and radiative decays can populate the acceptance region because the kinematics do not constrain them. In Table 3 the signal over background expected for selected three body decays is shown together with the assumed rejection factors.

In order to suppress all  $K^+$  decay modes that might fake the  $K^+ \rightarrow \pi^+ \nu \bar{\nu}$  signal, it is necessary to render the detector hermetic with respect to photons from  $\pi^0$  originating in the  $K^+$  fiducial decay region. This can be provided, in order of increasing angular coverage, by a forward Small Angle Calorimeter (SAC), two Intermediate Ring Calorimeters (IRC-1 and 2), the Liquid Krypton Calorimeter (LKR) and, finally, 13 Large Angle Photon Veto (ANTI) counters (covering angles out to  $\approx 50$  mr.). The layout of these elements is shown in Figures 8 and 9.

There also exist decay modes (with branching ratios  $\geq 10^{-5}$ ), e.g.  $K_{e4}$  ( $K^+ \rightarrow \pi^+ \pi^- e^+ \nu$ ) and  $K_{\mu 4}$ , in which the  $e^+$  ( $\mu^+$ ) may escape detection. By analogy to the case of decays to  $\pi^0$ , it is mandatory that the  $\pi^-$  be observed and that the detector therefore be rendered hermetic with respect to negatively charged particles of momentum  $\leq 60$  GeV/ $c$ .

This function can most readily be provided by the 6 tracking detectors (chambers composed of straw tubes - described in Section 9), which form the active elements of a Double Magnetic Spectrometer. The  $\pi^-$  have to be deflected away from the +75 GeV/ $c$  beam by a distance greater than the gap in the straw chambers which surround the beam. This condition can be fulfilled for the proposed spectrometer layout with magnets providing pT-kicks of -270<sup>§</sup>) and +360 MeV/ $c$ , respectively, combined with straw chambers having an active coverage outside  $\pm 5$  cm, aligned along the central trajectory of a +60 GeV/ $c$  particle through the spectrometer. The layout of the spectrometer and straw chambers surrounding the beam are shown in principle in Figure 8.

A complementary approach could be to detect the  $\pi^-$  that remain close to the beam in a detector following the Magnetised Muon Detector MAMUD ( $p_T$ -kick = +1500 MeV/ $c$ ) at the downstream end of the experiment, where they will be deflected to the opposite side of the SAC with respect to the +75 GeV/ $c$  beam (Figure 8). However, this would require opening up the horizontal aperture of MAMUD, with a resulting reduction in acceptance for detecting muons.

---

<sup>§</sup>corresponding to the strength of the existing MNP-33 spectrometer magnet.

## 4 The Beam for the $K^+ \rightarrow \pi^+ \nu \bar{\nu}$ Experiment

### 4.1 Rationale

#### 4.1.1 Choice of Accelerator and Primary Proton Momentum

Once the attempt is abandoned to separate kaons with respect to other charged particles by super-conducting r.f. cavities (realistically limited to momenta smaller than  $30 \text{ GeV}/c$  for cavities of frequency less than  $4 \text{ GHz}$ <sup>¶</sup>), there appear to be distinct advantages in performing a charged kaon, rare-decay experiment at high energy and, in particular, at the **400 GeV/c SPS**<sup>||</sup>. Based on a simple empirical formula, fitting the measured particle production data [14], we derive that, per primary proton of fixed momentum  $p_0$ , the maximum  $K^+(K^-)$  **production** in a given momentum bite  $\Delta p/p$  and solid angle occurs at momentum  $p_K \approx 0.35 p_0$  ( $\approx 0.23 p_0$ ). Moreover, at fixed  $p_K/p_0$ ,  $K^+$  ( $K^-$ ) **production** increases as  $p_K^2$  (and therefore as  $p_0^2$ ). It follows that the number of  $K^+$  ( $K^-$ ) **decays** in a fixed fiducial length is maximum for  $p_K \approx 0.23 p_0$  ( $\approx 0.15 p_0$ ) and, at fixed  $p_K/p_0$ : the number of  $K^+(K^-)$  decays in a fixed length increases as  $p_K$  (and therefore as  $p_0$ ). Furthermore, the acceptance, efficiency and resolution of certain detector elements, e.g. photon veto counters, calorimeters and muon detectors, improve at higher energy.

#### 4.1.2 Comparison with the FNAL Main Injector

We may compare the advantages and disadvantages of the CERN-SPS with respect to the only other high energy proton machine: the FNAL Main Injector (MI). Since, in an unseparated beam, the experiment is not proton limited and both machines have similar duty cycle, there is no advantage to perform the experiment at the MI. On the contrary, the fraction of kaons at the SPS is 6 % to be compared to 4 % at the MI. Therefore, for the same fraction of kaons decaying in the fiducial volume, which depends only on the geometry of the experiment, the accidental rate due to unwanted particles per kaon is 50% smaller at the SPS, which is a considerable advantage.

---

<sup>¶</sup>The distance between the cavities has to increase as  $p_K^2$ , whereas the kaon decay length increases only as  $p_K$ . Thus the proposed [4] 216 m long,  $22 \text{ GeV}/c$ , FNAL  $K^+$  beam would suffer from a survival factor of only 0.27 without considering losses from the separation mechanism.

<sup>||</sup>400 GeV/c is the highest proton momentum of the SPS, at which a duty cycle of  $\approx 0.3$  can be sustained.

### 4.1.3 Choice of a Positive Kaon Beam

The choice of a positive rather than a negative (unseparated) beam is motivated by the fact that, at a possible beam momentum of  $75 \text{ GeV}/c$  (see 4.1.4), the ratio of production rates:  $K^+/K^-$  per  $400 \text{ GeV}/c$  proton is  $\approx 2.1$  and the ratio:  $(K^+/\pi^+)/(K^-/\pi^-) \approx 1.2$ , whilst the ratio:  $\frac{(K^+/\text{Total positive beam flux})}{(K^-/\text{Total negative beam flux})} \approx 1.0$ .

### 4.1.4 Choice of Beam Momentum

The choice of **75 GeV/c** as the central beam momentum is a compromise among the criteria for which the variations with momentum (from  $400 \text{ GeV}/c$  protons at zero production angle\*\*) are listed in Table 3. The  $K^+$  beam fluxes reported in the table are estimated using an empirical formula, fitting the measured particle production data [14]. The numbers in italics are taken from measurements made at  $60$  and  $120 \text{ GeV}/c$  from  $400 \text{ GeV}/c$  protons on  $300$  and  $500$  mm Be targets - interpolated to a  $400$  mm long target. Hence, secondary interactions in the target may contribute to the beam flux, particularly at  $60 \text{ GeV}/c$ . Moreover,  $75 \text{ GeV}/c$  appears to be nearly the maximum momentum for which a beam incorporating stages for large solid-angle acceptance, momentum selection,  $K^+$  tagging, beam momentum measurement and tracking, can be constructed using conventional beam elements and fitting into the existing length of  $102 \text{ m}$  from production target (T10) to the beginning of the NA48 decay fiducial region.

## 4.2 High-Intensity $K^+$ Beam

### 4.2.1 Beam Design and Layout

We propose to employ an unseparated beam of positive hadrons, to be derived from a readily-attainable flux of  $400 \text{ GeV}/c$  protons, in the SPS North Area High Intensity Facility [15], comprising the underground target and beam tunnel, TCC8, followed by the experimental cavern, ECN3, where the NA48 detectors are now installed. Furthermore, we plan to reuse the existing target station T10 and the present (straight) K12 beam line, of length  $102 \text{ m}$  to the exit of the final collimator, marking the beginning of the decay fiducial region and leading to the NA48 detectors (notably the liquid krypton e.m. calorimeter, LKR).

---

\*\*For the present, we assume a production angle centred around zero, though it may be worth considering another production angle: e.g. at  $75 \text{ GeV}/c$ , a  $5 \text{ mr}$  central production angle could lead to a factor 1.2 increase in  $K^+ / \text{Total beam flux}$ , however, requiring a factor 1.5 increase in primary proton flux to restore the  $K^+$  yield.

		$p_K$ (GeV/c)			
		60	75	90	120
$K^+$ beam flux at production for $3 \times 10^{12}$ incident protons	$\times 10^8$	1.1 1.3	<b>1.5</b>	1.9	2.4 2.3
$K^+$ survival factor over 102 m		0.80	<b>0.83</b>	0.86	0.89
$K^+$ / Total beam flux	$\times 10^{-2}$	5.2 6.8	<b>5.5</b>	5.6	5.2 4.7
$K^+/\pi^+$ flux	$\times 10^{-2}$	8.3 11.2	<b>8.6</b>	9.0	9.7 8.6
$K^+$ decays in 50 m	$\times 10^6$	8.9	<b>10.7</b>	11.6	11.4
$K^+$ decays in 50 m / Total beam flux	$\times 10^{-3}$	4.3	<b>3.9</b>	3.4	2.5
$K^+ \rightarrow \pi^+ \nu \bar{\nu}$ Acceptance (Region I, no $\pi^+$ momentum cut)		0.08	<b>0.11</b>	0.12	0.11
Accepted $K^+ \rightarrow \pi^+ \nu \bar{\nu}$ / Total flux	$\times 10^{-13}$	0.34	<b>0.43</b>	0.41	0.21

Table 3: Variation of relevant  $K^+$  production and decay parameters with secondary beam momentum for 400 GeV/c primary protons.

Compared to the present, simultaneous  $K^+$  and  $K^-$  beams [16], the single-charge beam begins with a triplet of radiation-resistant quadrupole magnets to collect a large solid angle acceptance at 75 GeV/c central momentum and to provide a focus in the vertical plane at the longitudinal position of the proton beam-dump (TAX). This is located (as in the present beam) at the centre of a 'front-end achromat', consisting of four, radiation-hard dipole magnets, the first pair of which displace the 75 GeV/c beam vertically downward by 100 mm onto a momentum-defining slit contained in the TAX to permit the selection of a narrow ( $\simeq 1\% \Delta p/p$ ) momentum band. The second pair of magnets then return the wanted particles onto the undeviated axis. Thereafter, a pair of quadrupoles focuses the beam through redefining collimators in both planes. In between these, it passes through a field-free bore traversing magnetic iron blocks, filling the normal gap of three large dipole magnets, which serve to sweep aside muons accompanying the beam. A further pair of quadrupoles renders the beam parallel at the location of an upgraded, hydrogen gas-filled, CEDAR differential Cerenkov counter [17], capable of tagging only the  $K^+$  in the beam. A final pair of quadrupoles produces a beam which converges slightly towards a waist, located at the downstream end of the experiment. The last 30 m length to the final collimator

incorporates a 'second achromat' of four dipole magnets and three sets of 'GIGATRACKER' detectors (SPIBES-1,2 and FTPC-3) to provide momentum and direction measurements on all particles. Upstream of the final collimator the beam is surrounded by a pair of 5 m-long, magnetic iron 'scrapers' of 60 mm horizontal and vertical aperture, respectively. They are toroidally magnetised so as to defocus  $\mu^+$  from the beam. The layout and schematical optics of the beam, calculated using TRANSPORT [18], are shown in Figure 7.

The decay fiducial region is housed in a large,  $\approx 120$  m long, evacuated tank, which is closed off by a thin ( $\approx 0.05X_0$ ) aluminium window. The centre of this window is traversed by a thin-walled beam tube (of inside diameter varying from 160 to 220 mm), which allows the beam to be transported in vacuum through the principal detectors downstream of the tank. This part of the layout is shown schematically in Figure 8. The detector components are described in later Sections. Of relevance for the beam are a **double magnetic spectrometer**, comprising tracking chambers composed of straw-tubes (ST.CH-1-6), covering the full acceptance outside the beam passage. These are interspaced by two, large-aperture dipole magnets (MNP33-1 and MNP33-2) which provide horizontal  $p_T$ -kicks of  $-270\text{MeV}/c$  and  $+360\text{ MeV}/c$ , thereby deflecting the  $75\text{ GeV}/c$  beam by  $-3.6$  and  $+4.8$  mr, respectively. Beam and associated particles (e.g. muons) of all momenta are thus centred on the axis again downstream of the LKR calorimeter, where a combined magnetised-iron hadron calorimeter and muon detector (MAMUD) is located. This is designed to produce a  $+1500\text{ MeV}/c$  horizontal  $p_T$ -kick on the beam, causing a further  $+20$  mr deflection. The beam is hence displaced 170 mm off axis  $\approx 8$  m further downstream (at the extremity of ECN3), so as to clear a 100 mm radius photon veto calorimeter (SAC). Two intermediate ring calorimeters are required around the beam: IRC-1 surrounds the centre of the aluminium vacuum window which preceeds a large,  $\approx 18$  m long, gas-filled, Ring Imaging Cherenkov counter (RICH) and IRC-2 surrounds the beam tube between the RICH and the LKR calorimeter. In addition to the LKR itself, a series of 13 large-angle, annular, photon ANTI-counters are located at intervals along the vacuum tank as shown schematically in Figure 9. This whole system of photon detectors is designed to provide hermetic veto coverage out to an angle of  $\approx 50$  mr for photons originating in the beam decay fiducial region.

#### 4.2.2 Beam Parameters and Estimated Performance

The principal parameters of the proposed high-intensity  $K^+$  beam are listed in Table 4, where the factors responsible for the flux yield are compared with those for the present K12 simultaneous  $K^+$  and  $K^-$  beam, designed for experiment NA48/2 [16]. The effective solid

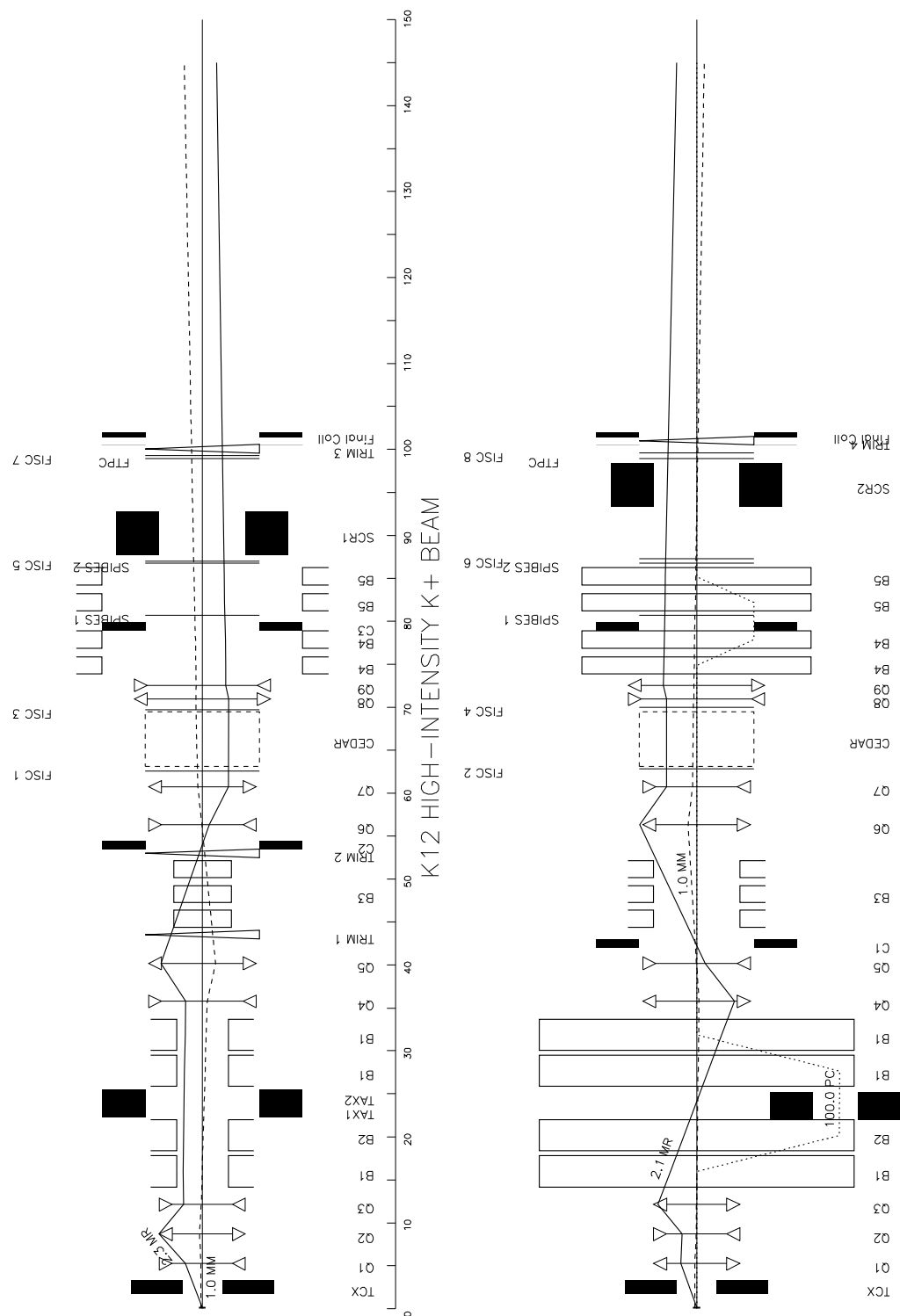


Figure 7: Schematic layout and optics of the high intensity  $K^+$  beam

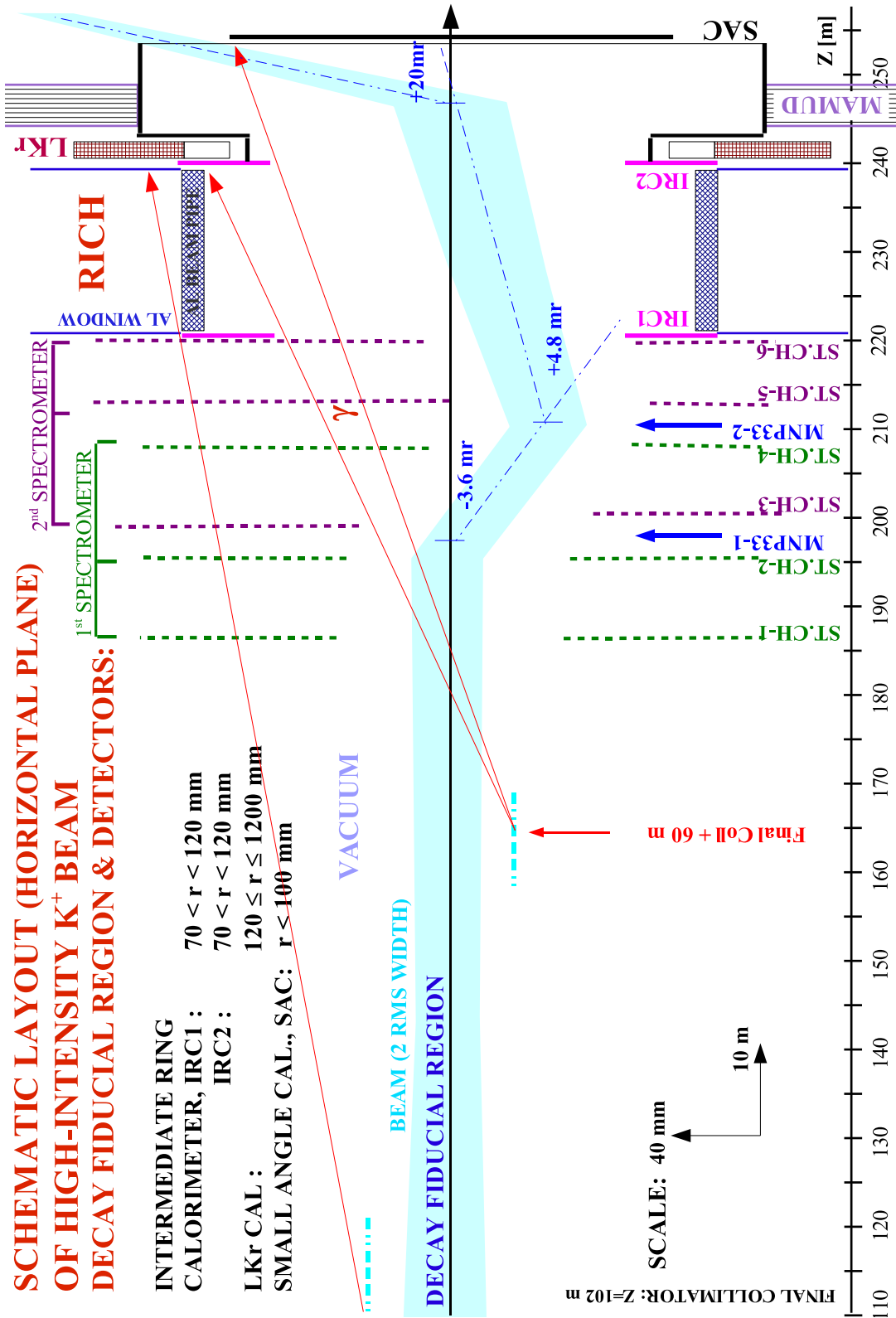


Figure 8: Schematic layout of beam and detectors incorporating the Small Angle Calorimeter (SAC) and Intermediate Ring Calorimeters (IRC1 and 2).

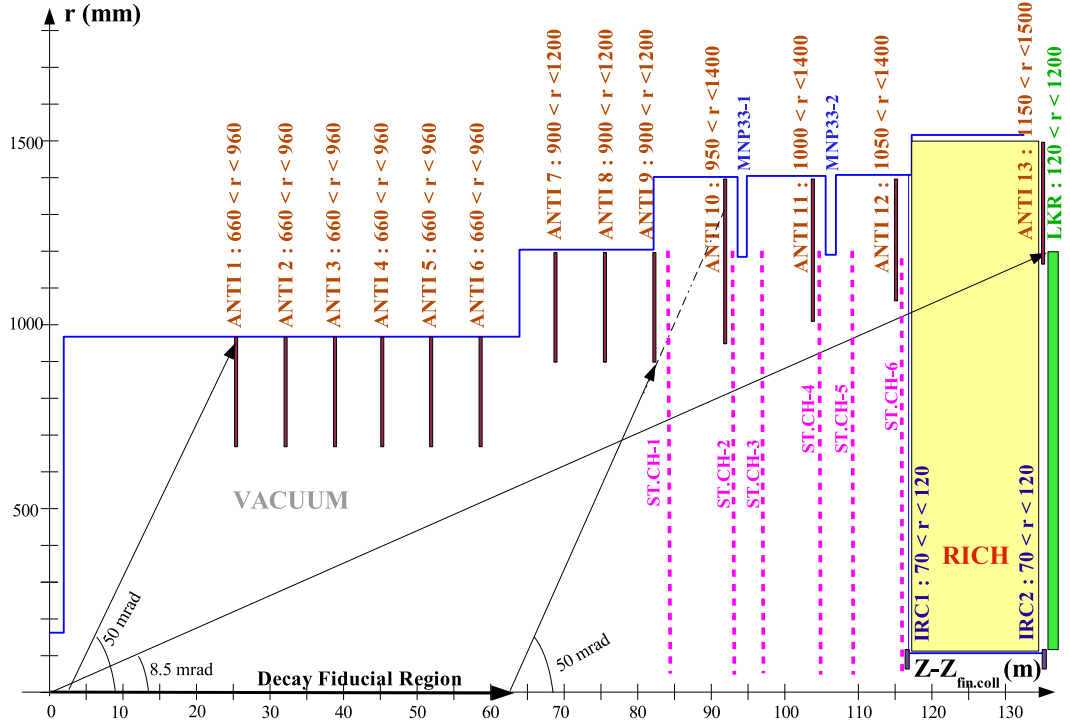


Figure 9: Schematic layout of decay fiducial region and Photon ANTI-counters.

angle and momentum acceptance, as well as the beam sizes and divergences of both beams were calculated using the ray-tracing programme TURTLE [20]. For example, the simulated momentum distribution and the spot size at the position of the first Gigatracker detector (SPIBES-1) are shown in Figure 10 and Figure 11, respectively. The particle fluxes of the present beam are taken from the actual measurements made at 60 GeV/ $c$  [14], whereas those for the proposed 75 GeV/ $c$  beam are derived from the latter by extrapolation using the empirical formula proposed in [14].

The muons accompanying a high-energy, high-intensity, secondary beam contribute a major part of the single-particle flux, to which the detectors outside the beam are exposed. The transport and decay to  $\mu^\pm\nu$  of a wide spectrum of  $\pi^\pm$  and  $K^\pm$  originating in the target has been simulated and the layout of muon-deflecting elements optimised using the programme HALO [21]. This tracks the parent particles and their decay muons inside the beam apertures and the 'halo' muons leaving the apertures through the vacuum tubes, magnet yokes and shielding surrounding the beam. Results of such calculations are given in Tables 6 and 6. As an example, the distribution of all halo muons traversing a plane of ST.CH-6 is plotted in Figure 12.

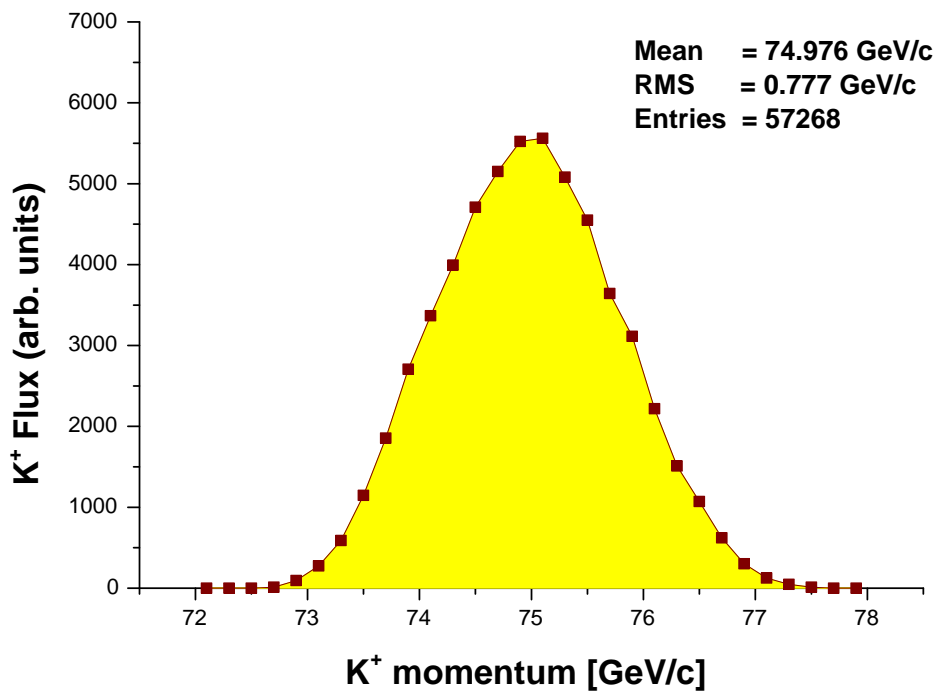


Figure 10: Beam momentum distribution.

*Y vs X at Station1 - pixels*

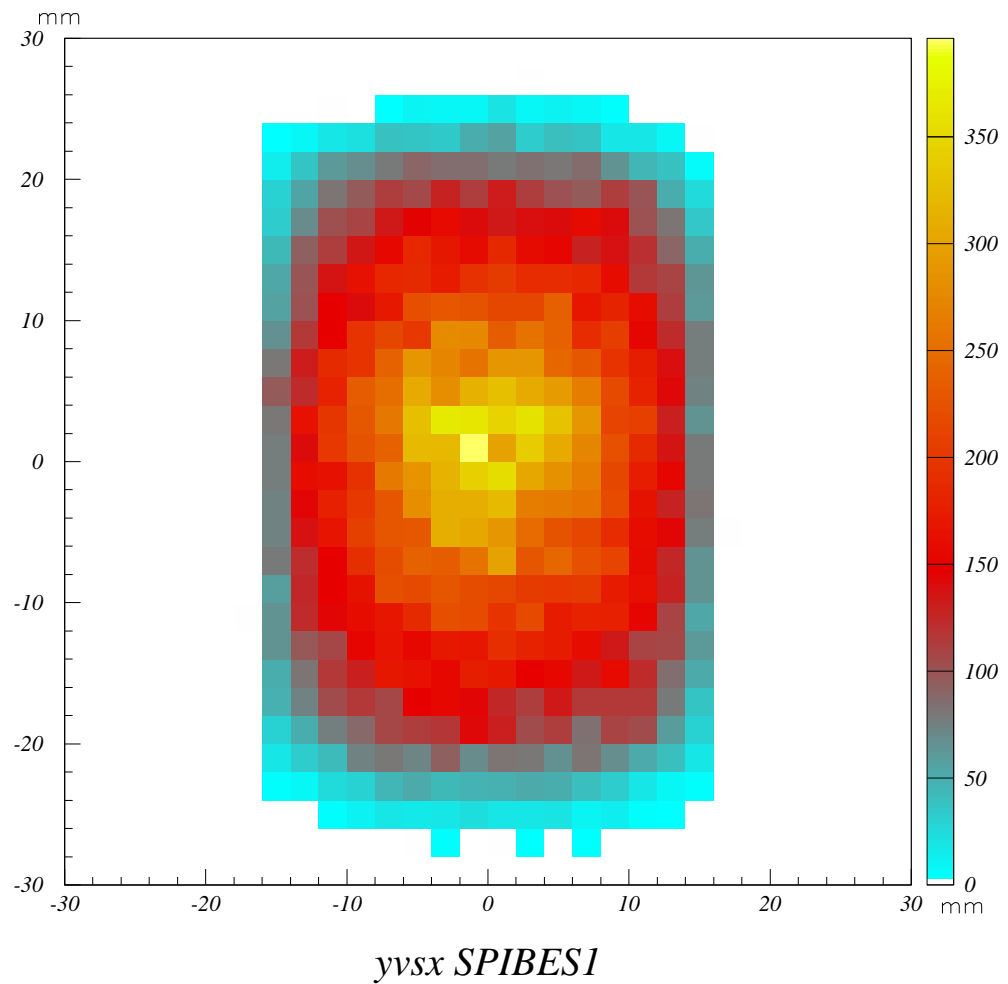


Figure 11: Beam spatial distribution at SPIBES-1.

Beam	Present K12 (NA48/2)	New High Intensity $K^+$ (NA48/3)	Factor w.r.t. present
SPS protons per pulse	$1 \times 10^{12}$	$3 \times 10^{12}$	3.0
Duty cycle (s / s)	4.8 / 16.8	same	1.0
Beam Acceptance H,V (mr)	$\pm 0.36$	$\pm 2.3, \pm 2.1$	
Solid Angle ( $\mu\text{sterad}$ )	$\simeq 0.40$	$\simeq 16$	40
Central $K^+$ Momentum $\langle p_K \rangle$ (GeV/c)	60	75	$K^+ : 1.50$ $\pi^+ : 1.35$ Total: 1.35
Momentum band $\Delta p_K$ GeV/c	$63-57 = 6$	76.5-73.5=3.0	$\simeq 0.5$
Eff.: $\Delta p/p$ (%)	$\pm 5$	$\pm 2.0$	$\simeq 0.4$
RMS: $\Delta p/p$ (%)	$\simeq 4$	$\simeq 1.0$	$\simeq 0.25$
Beam size ( $\pm 2$ RMS)(cm)	$r = 1.5$	$\pm 1.6, \pm 2.2$	
Area at Gigatracker (cm <sup>2</sup> )	$\simeq 7$	$\simeq 14$	$\simeq 2$
Divergence: RMS (mr)	$\simeq 0.05$	$\simeq 0.1$	$\simeq 2$
Decay fid. length (m) ( $\tau_{K^+}$ )	50 0.111	60 0.107	0.96
Beam flux/pulse( $\times 10^7$ ): protons	0.86	49	
$K^+$	<b>0.31</b>	<b>15</b>	<b>50</b> ( $\simeq 30$ )
$\pi^+$	3.32	150	45 ( $\simeq 27$ )
$e^+$	0.95	35	
Total beam flux per pulse ( $\times 10^7$ )	5.5	250	$\simeq 45$ ( $\simeq 27$ )
Rate (3s eff. spill length) (MHz)	18	800	$\simeq 45$ ( $\simeq 27$ )
Rate in SPIBES (MHz/cm <sup>2</sup> )	2.5	$\simeq 60$	$\simeq 25$ ( $\simeq 15$ )
Running time/yr (days)	120	100	
Overall Efficiency	0.5	0.6	
Effective number of pulses	$3 \times 10^5$	$3 \times 10^5$	1.0
$K^+$ decays per year	$1.0 \times 10^{11}$	$4.8 \times 10^{12}$	$\simeq 48$
$K^+ \rightarrow \pi^+ \nu \bar{\nu}$ Events/year (BR= $10^{-10}$ , accept. = 10%)		48	

Table 4: A comparison between the current NA48/2 beam and the future one. The figures in brackets in the last column refer to increase in rate with respect to the sum of the positive and negative NA48/2 beams.

<b>FLUX</b> $\times 10^6$ for $10^{12}$ interacting p in H $\approx 3 \times 10^{12}$ incident p on Be	$\pi^+ \rightarrow \mu^+ \nu$	$K^+ \rightarrow \mu^+ \nu$	$\pi^- \rightarrow \mu^- \bar{\nu}$	$K^- \rightarrow \mu^- \bar{\nu}$	TOTAL
$\pi$ and $K$ at exit final coll. (T10 + 102.0 m)	1551	148	0	0	1700
$\mu$ in beam at final coll.	15.0	1.6	0	0	17
$\mu$ 'HALO' at exit final coll. reaching LKR cal.	2.6	0.6	0.2	0	3
$\mu$ 'HALO' in one plane of ST.CH-1 (T10 + 186.3 m) $[2.4 \times 2.4] \text{m}^2,  x  > 8 \text{ cm}$	4.4	12.0	0.4	0.2	17
ST.CH-2 (195.1 m)	4.0	12.8	0.4	0.2	17
ST.CH-3 (200.5 m)	3.6	13.2	0.2	0.2	17
ST.CH-4 (207.7 m)	5.4	14.4	0.2	0	20
ST.CH-5 (213.1 m)	5.4	14.6	0.2	0	20
ST.CH-6 (220.3 m)	4.8	15.0	0.2	0	20
13 Large Angle ANTIs:OR	6.4	4.4	0.2	0.2	11
IRC-1: $7 < r < 12 \text{ cm}$ (220.7 m)	6.0	1.6	0	0	8
IRC-2: $7 < r < 12 \text{ cm}$ (239.7 m)	5.8	1.8	0	0	8
LKR: $12 < r < 120 \text{ cm}$ (241.1 m)	3.2	16.8	0.2	0	20
SAC: $0 < r < 10 \text{ cm}$ (254.2 m)	0	1.2	0.2	0	1

Table 5: Estimated muon halo in the high-intensity  $K^+$  beam.

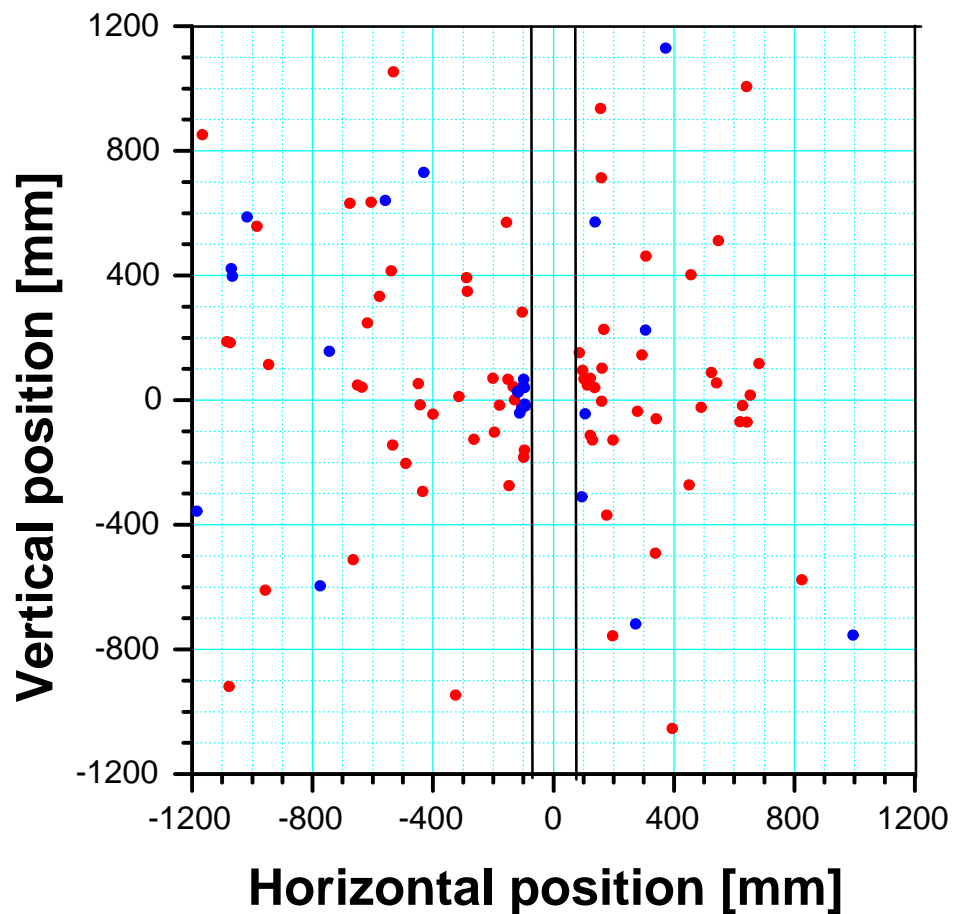


Figure 12: Distribution of all halo muons traversing a plane of ST.CH-6.

Detector	Halo rate
At CEDAR-PM's ( $8 < r < 12$ cm)	$\approx 10$ kHz/cm <sup>2</sup>
At GIGATRACKER ( $3 <  x  < 6$ cm)	$\approx 10$ kHz/cm <sup>2</sup>
Straw Chamber plane at $ x  > 5$ cm	$\approx 10$ MHz
Average/1 cm straw tube	$\approx 50$ kHz
Maximum/1 cm ( $5 <  x  < 6$ cm)	$\approx 500$ kHz
CHOD, LKR Total rate ( $4.5 \text{ m}^2$ ; $12 < r < 120$ cm)	$\approx 7$ MHz
Average	$\approx 0.2$ kHz/cm <sup>2</sup>
Maximum ( $12 < r < 16$ cm)	$\approx 2$ kHz/cm <sup>2</sup>

Table 6: Expected instantaneous muon rates in the detectors for  $3 \times 10^{12}$  ppp on target over a 3 s effective spill.

### 4.3 Cost estimate of the new beam line

The material cost of the new beam-line has been estimated to be 425 kCHF. A detailed break-down of the cost estimate and the foreseen amount of man-power for the installation is available.

#### 4.3.1 SPS Availability and Scheduling

From Table 4 we conclude that, with an effective overall data-taking efficiency (SPS and detector) of 0.6, a useful  $K^+ \rightarrow \pi^+ \nu \bar{\nu}$  acceptance of 0.1 and allowing for a 20% loss due to dead-time, about 40 events would be accumulated in a year of  $\approx 5 \times 10^5$  scheduled fixed-target proton spills (of 4.8 s duration at 400 GeV/c) for a Branching Ratio  $BR(K^+ \rightarrow \pi^+ \nu \bar{\nu}) = 10^{-10}$ . The beam and experiment presented here, requiring  $3 \times 10^{12}$  protons per pulse on target T10 ( $6 \times 10^{12}$  ppp on target T4) is entirely compatible with simultaneous running of COMPASS in the M2 beam ( $\approx 1.2 \times 10^{13}$  ppp on T6) and with experiments or tests in the remaining SPS beams H2, H4, H6 and H8. We note that the target number of SPS fixed target spills requested by COMPASS is  $7.2 \times 10^5$  per year [22], which is more than 40% larger than our request.

In the year 2006, before the new beam can be available, we request the use of the existing K12 beam. It can provide a (relatively broad-band) beam of positive hadrons (without particle-identification) around 75 GeV/c, with a flux up to 16 times that used for experiment NA48/2 [16] (Table 4). The addition of a standard (nitrogen gas-filled) CEDAR-W counter in the beam line will allow this device to be tested with new, high rate, photon detectors.

Moreover, the beam line can be used to provide beams of electrons and muons to test the detectors. The purpose of this programme is to continue the tests, started in 2004, on prototype detector elements to validate their choice for the proposed experiment. In a second phase, starting in 2007, we request that the new beam be installed, so as to tune and assess its performance and to exploit it to test and calibrate the upgraded and new detectors as they become available.

#### 4.4 The Decay Vacuum Tank

A FLUKA simulation was used to study interactions of pions, kaons and protons with the residual gas. The data were passed to a detector simulation which included the standard geometry according to the latest layout and the probability that such an interaction can cause fake triggers was computed. We conclude that the vacuum should be better than  $6 \times 10^{-8}$  mbar to keep the background to less than one fake event per year. This very challenging requirement can be relaxed by an order of magnitude by positively tagging the kaons by means of the CEDAR counter described in one of the following sections.

Out-gassing rate measurements have been done on the present vacuum tank. The value obtained, a few  $10^{-8}$  mbar l/s/cm<sup>2</sup>, is compatible with available data on out-gassing rate for normal painted steel. The required vacuum level could be achieved with a major upgrade of the vacuum system. It would require, for example, about 20 large diffusion pumps, 50000 l/s, and the associated pre-vacuum system. The cost of such a system will be about 1 MCHF, to which one must add the operation cost. We are investigating alternative solutions requiring a smaller vacuum system. In order to minimize the out-gassing rate of the present vessel, one could, for instance, glue a stainless steel liner or otherwise treat the inner surface of the tank. Tests should be performed to evaluate the performance of such a solution, and a careful analysis of the practical and reliable application of this solution to the full length of the tank. Another possibility is to replace completely the vacuum vessel by a stainless steel tube, which would have a much lower out-gassing rate. Sections of 6 meters could be prefabricated and welded together in the experimental area in order to minimize the number of flanges. The tube thickness of about 20 mm could be reduced by welding reinforcement ribs on the outside. Ribs every 4 meters would allow the thickness to be reduced to about 10 mm. We are currently investigating the cost of this solution.

## 5 Detectors

The detector elements are listed here together with a brief functional description. The principal elements are then described in the following sections. The overall beam and detector layout is shown in Figure 13.

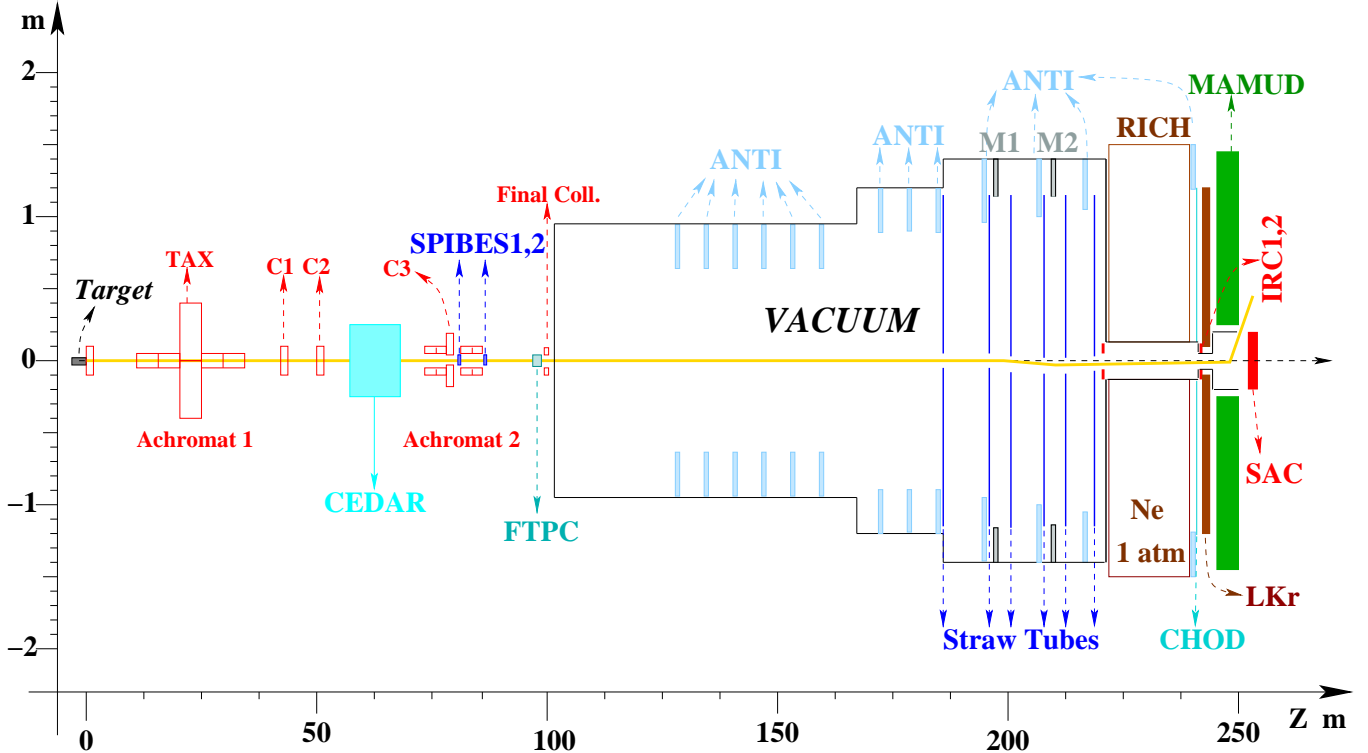


Figure 13: Detector Layout.

### 1. CEDAR

A Differential Cherenkov counter (an upgraded form of the CEDAR built for the SPS secondary beams [17]) placed on the incoming beam to tag the minority particles of interest (kaons). We assume that one of the existing counters can be made available.

### 2. GIGATRACKER

- FAST PIXEL (SPIBES)

Thin silicon micro-pixel detectors for (redundant) momentum measurement of the incoming beam with sub-nanosecond time resolution to provide a tight time

coincidence between the kaon and the pion tracks and to simplify the pattern recognition in the gas TPC 12 m downstream.

- Micromegas-based Flash-TPC (FTPC)

A gas Time Projection Chamber to measure the direction of the incoming beam particles with the least amount of material to minimise the effect of multiple scattering on the measurement of the angle between the kaon and the pion.

### 3. ANTI

A set of ring-shaped anti-counters surrounding the vacuum tank and providing full coverage for photons originating from the decay region with angles as large as 50 mr.

### 4. STRAW TRACKER

A double magnetic spectrometer measuring the direction of the out-going pion and its momentum and providing a redundant measurement of the latter. Chambers of straw tubes are proposed as the tracking detector for their capability to operate in vacuum.

### 5. RICH

A gas Ring Imaging Cherenkov counter providing muon/pion separation.

### 6. CHOD

A hodoscope for triggering and precise timing of the charged track, based on multi-gap glass RPCs.

### 7. LKR

A high-performance electromagnetic calorimeter acting as photon veto in the angular region between 1.0 and 15.0 mr. We plan to use the 20-ton NA48 Liquid Krypton Calorimeter (LKR) with properly updated electronics.

### 8. MAMUD

A magnetised hadron calorimeter and muon detector capable of identifying muons with inefficiencies smaller than  $10^{-5}$ . It also serves the purpose of deflecting the charged beam away from the photon detector (SAC) placed at the end of the hall.

### 9. IRC1-2, SAC

Intermediate ring and small angle photon veto calorimeters covering the angular regions around and in the beam.

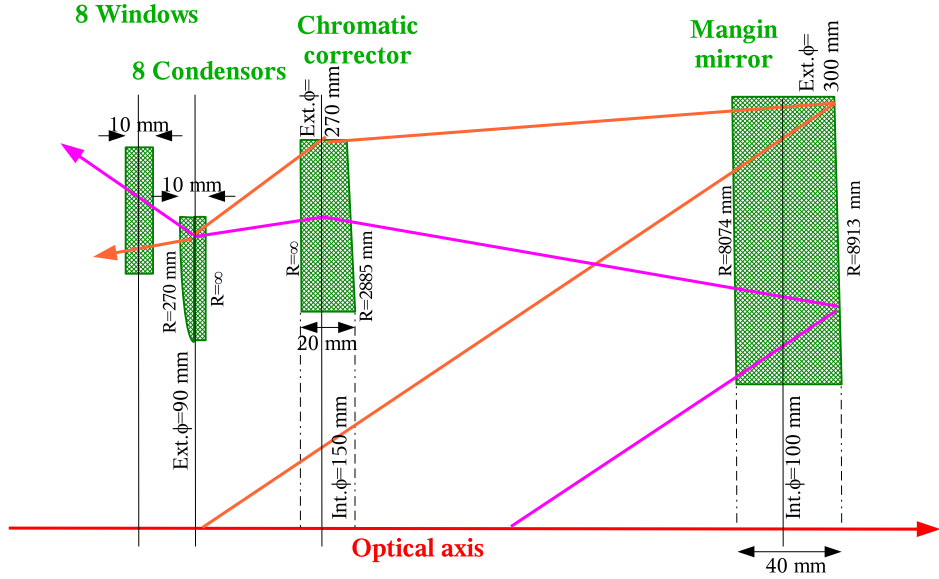


Figure 14: View of the CEDAR optics (note the distorted scale).

## 6 CEDAR

The  $K^+$  component in the beam can be tagged positively by using an upgraded version of the existing CEDAR differential Cerenkov counters [17]. This is important because a beam pion interacting with the residual gas in the vacuum tank may be mistaken as a signal if no other visible particles are produced in the process. The CEDAR counters have been built for use at the SPS and two versions exist. The North CEDAR, normally filled with Helium gas, is optimized for high energies and the West CEDAR, Nitrogen filled, for lower beam momenta. It has been verified by a ray tracing program that the West version of this instrument would function well for our application with hydrogen gas instead of nitrogen, thus reducing significantly the scattering of the beam in the gas.

As shown in Figure 14 (taken from [17]), the Cerenkov light produced in the gas is reflected by a Mangin mirror via a chromatic corrector lens through a diaphragm and via condenser lenses onto 8 locations for photon detectors. By reducing the diaphragm aperture around the passage of photons from  $K^+$  only, the light from pions and protons is blocked. To manage the 50 MHz rate from the kaon component in the beam, it is proposed to replace

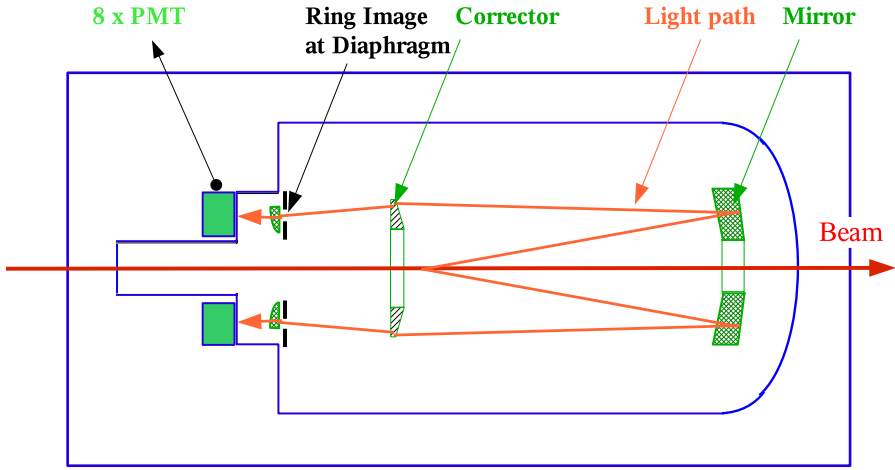


Figure 15: Schematic layout of the CEDAR counter.

the present photomultipliers by e.g. eight, 32-channel, linear array multi-anode PM's or by 32 individual 10 mm photomultipliers. It can be shown that the upstream 1.2 metres of the gas volume, surrounded by a steel tube, shown in Figure 15, contributes only very marginally to the efficiency and can thus be replaced by an extension of the beam vacuum. As shown in Figure 16, the size of the light spot at the location of the photon detectors is calculated to be  $32 \times 7 \text{ mm}^2$ , well matched to typical sizes of such array multi-anode photon multipliers. The singles rate on each pixel would then be of the order of 3 MHz, which can be handled by a high performance 1 GHz 8 bit flash-ADC system. Among advantages of such a system are continuous recording of the detector signals allowing rigorous assessment of the systematic uncertainties. A read out system based on the LHCb board TELL1 and recently available low-cost commercial ADC chips is under study [19].

A preliminary estimate for the cost of the modifications of the CEDAR counters to work with Hydrogen and different photon detectors has been made. It comprises mechanics, photon detectors, front-end electronics and cabling for a total of 450 kCHF.

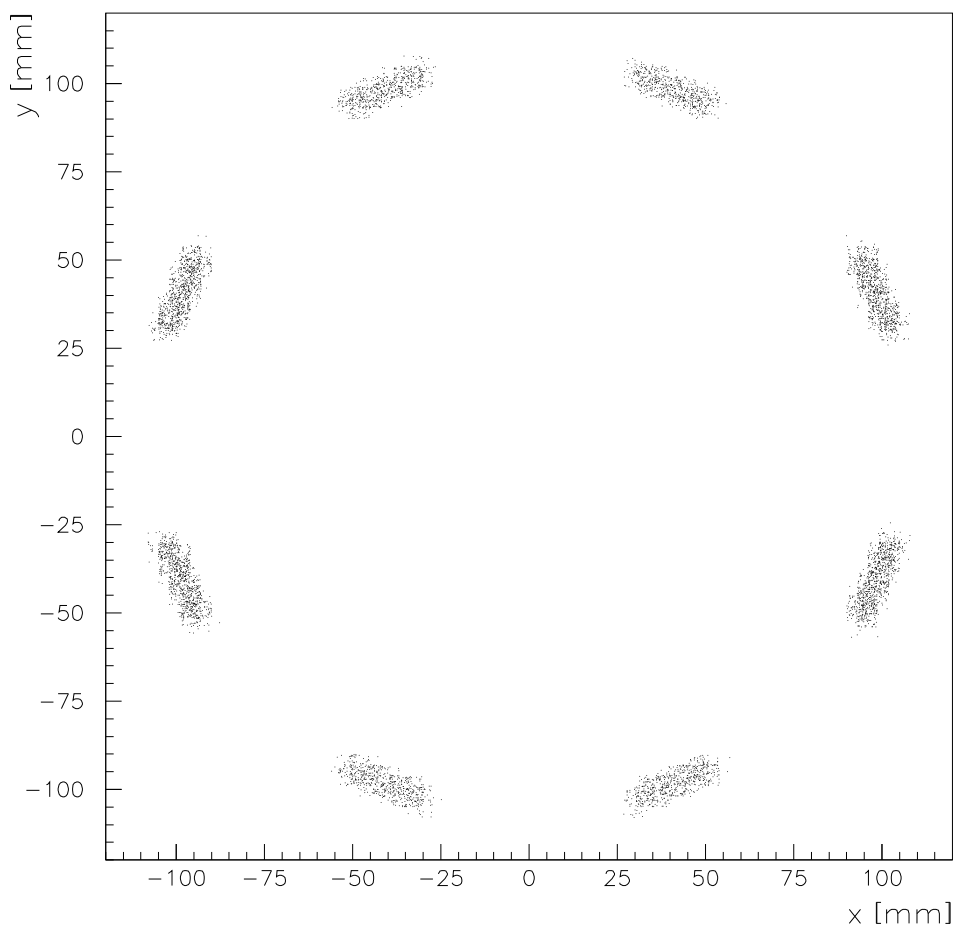


Figure 16: Spot of the Cherenkov light on the photon detectors.

## 7 GIGATRACKER

### 7.1 Specification of the time resolution

This experiment requires tracking of incoming beam particles with demanding performance. The average particle rate ( $\sim 60$  MHz/cm $^2$ , total rate up to 1 GHz) is about a factor of two larger than that expected for the innermost pixel layer of the proton-proton experiment CMS at the LHC and is therefore manageable. However, the limited material budget ( $< 1\% X_0$ ), the high rate and the required time resolution of  $\sim 150$  ps are technologically challenging. The Gigatracker information must be combined with the downstream double spectrometer data to reconstruct events and to reject the background from two-body  $K^+$  decays, by means of kinematic variables such as the missing mass squared ( $m_{miss}$ ), which depend on  $P_K$ ,  $P_\pi$  and  $\theta_{\pi K}$  (see equation 7). The planned beam spectrometer is based on two detector types: two stations of thin silicon pixel detectors which will provide two-dimensional track information and a momentum measurement with  $\sim 0.3\%$  resolution, and a micromegas-based TPC, read-out by high speed FADCs to measure the incoming charged track direction. We call Gigatracker the hybrid detector formed by the silicon pixel layers and the gaseous detector. The silicon pixel detectors are chosen to provide excellent time and position resolution. The micromegas TPC is preferred in the third station because the angular resolution is less affected by multiple scattering.

Since the flux of protons that can be delivered by the SPS to the T10 target is not a limitation, the overall performance of the experiment depends directly on the performance of the Gigatracker.

The relation between the fraction of misidentified tracks and the time resolution  $\sigma_t$  of the Gigatracker has been quantified by studying the resolution of  $m_{miss}^2$  for the background events  $K^+ \rightarrow \pi^+\pi^0$ . In case of events with only one track in the Gigatracker, simulations based on GEANT4 have shown that the ratio of signal to  $\pi^+\pi^0$  background ( $S/B$ ) is  $\sim 100$  for a signal acceptance of 10% and a  $\pi^0$  rejection inefficiency of  $2 \times 10^{-8}$ . For events with two tracks in the Gigatracker, the kaon candidate can be determined using the *best CDA* criterion, where CDA is the closest distance of approach between the incoming track and the outgoing  $\pi^+$  track. The quality of this criterion depends on the ratio between the beam size ( $\delta(x)_{rms} \sim 0.8$  cm and  $\delta(y)_{rms} \sim 1.1$  cm at the third station of the Gigatracker) and on the CDA resolution ( $\sigma(CDA) \sim 1.4$  mm with the proposed layout). In our design the probability of wrong matching is 8.6%. Within  $\pm 2\sigma_t$ , with  $\sigma_t = 150$  ps, roughly 36% of the events have more than one track in the Gigatracker and in  $\sim 3.1\%$  of them, the incoming

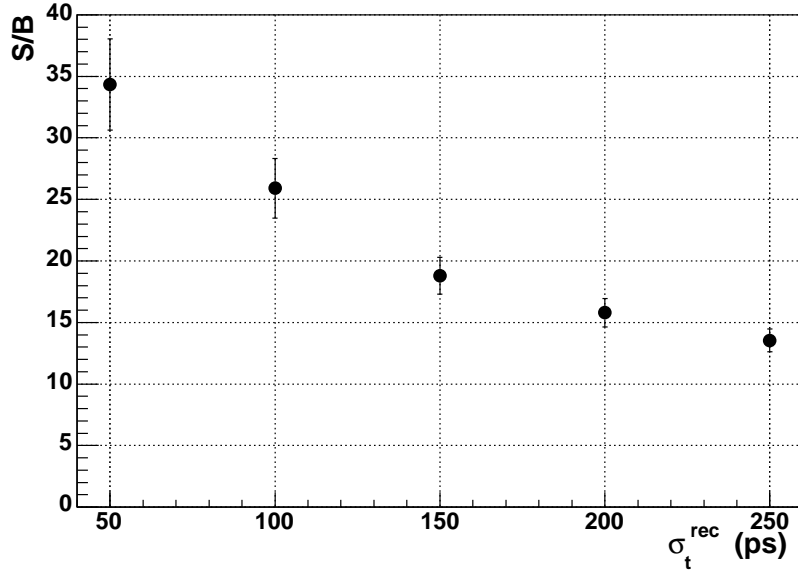


Figure 17:  $S/B$  as a function of the time resolution of the reconstructed beam track  $\sigma_t^{rec}$  if the events with more than one track in the Gigatracker are kept. The corresponding  $\sigma_t$  per SPIBES is  $\sqrt{(2)}\sigma_t^{rec}$

and outgoing tracks are wrongly matched. Because of the beam divergence ( $\sim 100 \mu\text{rad}$ ), the  $m_{miss}^2$  resolution for those events is 3.5 times worse and the  $S/B$  ratio deteriorated from  $\sim 100$  to  $\sim 25$ , as shown in Figure 17. In Figure 17 the dependence of the  $S/B$  ratio is given as a function of the reconstructed time resolution  $\sigma_t^{rec}$  in the Gigatracker and the corresponding  $\sigma_t$  per SPIBES is derived with the factor  $\sqrt{n}$ , where  $n$  is the number of SPIBES stations. In conclusion, keeping the events with more than one track in the Gigatracker increases the background. As a consequence, the design value for the time resolution of the Gigatracker is  $\sigma_t = 150$  ps to match the sensitivity of the proposed experiment.

State-of-the-art pixel assemblies (ALICE) deploy silicon sensors of  $200 \mu\text{m}$  thickness coupled to  $150 \mu\text{m}$  thick read-out chips[23][24]. The material budget of the ALICE SPD detector layer, consisting of sensors, read-out chips, support structure, cooling and multi layer flex cable is  $1\% X_0$  per layer, which limits the momentum resolution. Tests are required to reduce the read-out chip and overall thicknesses.

The Si-pixel detector is a good candidate to achieve the required time resolution. The capacitance of a single pixel is typically 200 fF including the input capacitance of a fast pre-amplifier and the stray capacitance to the neighboring pixels. A threshold-to-noise ratio of 17 has been achieved with  $0.25 \mu\text{m}$  CMOS process and for a 25 ns peaking time (Alice/LHCb).

Simulation of a  $200\text{ }\mu\text{m}$  thick silicon detector with 3 ns shaping time gives a noise contribution to the time resolution of 50 ps with a  $0.25\text{ }\mu\text{m}$  CMOS process. It appears feasible, therefore, to reach a time resolution of the order of 150 ps for minimum ionizing particles. This must be demonstrated by R&D and prototype testing.

In conclusion, since the Si-pixel detector is a promising option to achieve the stringent specifications of the experiment, the development of a prototype function ASICs (pre-amplifier, discriminator and high resolution TDC) is required, for tests in a high intensity particle beam. This prototype study will then be followed by the design of a full-scale pixel ASIC. In the final design we might use the  $0.13\text{ }\mu\text{m}$  CMOS process currently being investigated for HEP applications.

## 7.2 The fast silicon pixel detector: SPIBES

The silicon pixel beam spectrometer for the possible experiment has demanding requirements, some of which are recalled below:

- Minimal material budget ( $\sim 0.4\% X_0$  per SPIBES station). This specification can be reached for a pixel assembly deploying silicon sensors of  $200\text{ }\mu\text{m}$  thickness coupled to  $100\text{ }\mu\text{m}$  thick read-out chips (for a total of  $0.32\% X_0$  of silicon). The contribution of the bump-bonding material ( $0.01\% X_0$ ) and of a  $120\text{ }\mu\text{m}$  thick fiber support acting as cooling substrate ( $0.06\% X_0$ ) leads to  $0.36\% X_0$ . The detectors may be operated either in air or vacuum. In the first case, in order to preserve the vacuum in the beam pipe, the material for mylar windows ( $100\text{ }\mu\text{m}$  thick =  $0.035\% X_0$ ) must be taken into account.
- A signal speed TCAD simulation of charge collection for  $200\text{ }\mu\text{m}$  thick silicon pixel detector shows that the duration of the current signal is  $\sim 3$  ns (see Figure 18) for an electric field of  $10\text{ kV/cm}$ , or higher. Owing to the contribution of the holes to the current, the tail is enhanced for the proposed geometry compared to the simulated one. A simulation of the front-end circuitry, which neglects the time-walk of the signal, indicates that the contribution from thermal, leakage and feedback system noise to the time resolution is of the order of 50 ps for the average pulse height corresponding to 18000 electrons (Figure 7.2). However, the signal is smaller in case of charge sharing between adjacent pixel cells.
- An on-chip TDC resolution of 150 ps is required to control the amount of background due to wrong matching of the incoming and outgoing tracks when accidental tracks

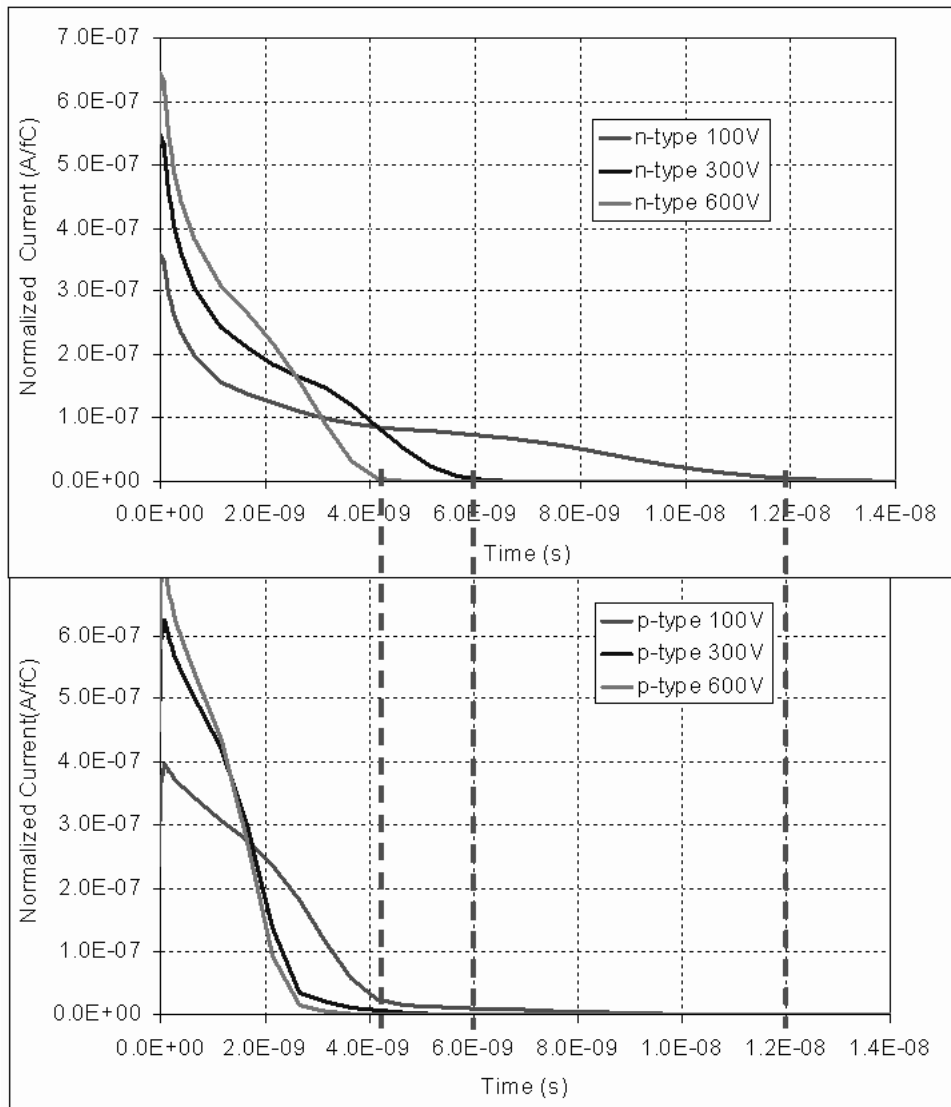


Figure 18: Simulations of the signal current as a function of time for both n-type and p-type substrates for a Alice-like layout of pixels  $425\mu m \times 50\mu m$

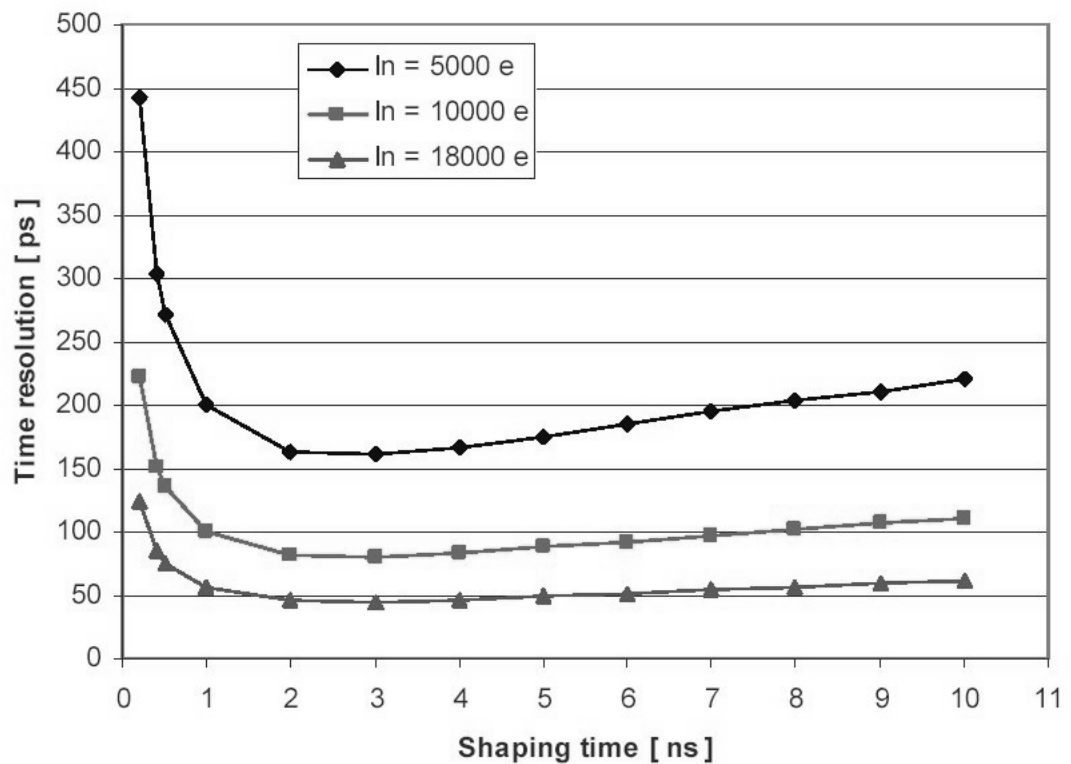


Figure 19: Simulation of the time resolution as a function of shaping time for different pulse heights.

are present in the Gigatracker.

- Figure 7.2 shows the resolution of the kinematic  $m_{miss}^2$  variable and the contribution of the Gigatracker. The Gigatracker has been simulated with two silicon pixel stations and a FTPC station. For each silicon layer a thickness of 0.4%  $X_0$  (which comprises sensor, readout chip and support) and a pixel cell size of  $300 \mu\text{m} \times 200 \mu\text{m}$  have been assumed. It follows that for the chosen pixel size the position resolution and the contribution to the  $m_{miss}^2$  resolution due to the Gigatracker is not critical for the simulated setup.

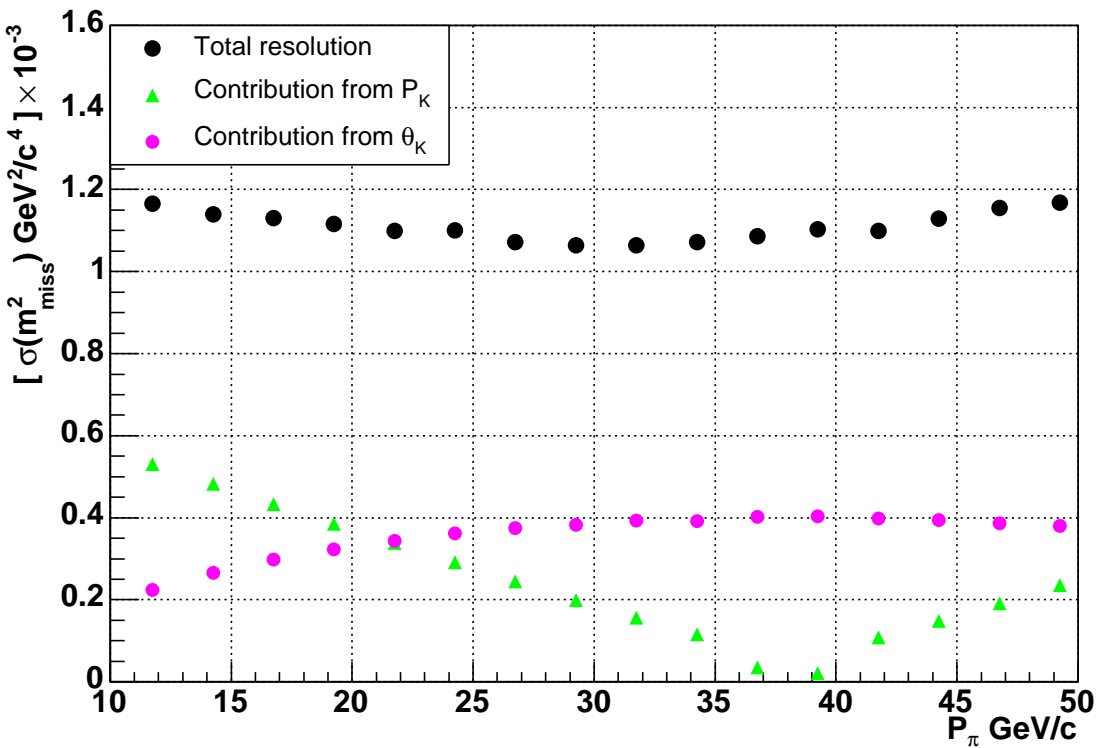


Figure 20: Contribution to the  $m_{miss}^2$  resolution due to the Gigatracker with pixel cell size of  $300\mu\text{m} \times 200\mu\text{m}$

The beam size fits the SPIBES dimensions, which are dictated by the maximum dimension of the photolithographic process for the readout chip to 20-21 mm. A possible design, that minimizes the material budget, is to cover one of the two dimensions of the beam (i.e. horizontally) with two readout-chips without overlap and with some lateral space left for

power and read-out busses. The beam area at the Gigatracker has been adapted accordingly to  $36(x) \times 48(y) \text{ mm}^2 = 17.3 \text{ cm}^2$  and therefore the beam intensity is  $\sim 60 \text{ MHz cm}^{-2}$ . However the beam flux is not uniform and the beam intensity varies up to the maximum rate of  $150 \text{ MHz /cm}^2$  in the center of station three.

The radiation environment must also be considered. In order to evaluate the average fluence in 100 days of running one needs to normalise the flux of particles ( $7.2 \times 10^{13} \text{ particles / cm}^2$  or  $2.4 \times 10^{14} \text{ particles / cm}^2$  in the center) to the 1 MeV neutron equivalent fluence. We use a conversion factor equal to 0.74, as derived from the ratio of the displacement damage cross section for 24 GeV pions ( $\sim 35 \text{ MeV mb}$  [25]) and 1 MeV neutrons ( $\sim 95 \text{ MeV mb}$ ), including a safety factor of 2. The accumulated design fluence for the Gigatracker sensors is  $1.8 \times 10^{14} \text{ 1MeV neutrons/cm}^2$  maximum, corresponding to a radiation exposure total dose (estimated for 100 days operation) of  $\sim 10 \text{ Mrad}$ .

The p-in-n material will be type inverted and the depletion voltage will increase with the particle fluence. Annealing of the current and the depletion voltage will depend on the operating temperature. We plan, therefore, to operate the SPIBES stations up to a maximum defined fluence at which stable parameters and signal quality can be guaranteed, and to replace the detector planes which exceed this fluence.

### 7.3 Front-end Electronics and Sensors

These requirements need novel developments in some key technologies, such as sub-micron electronics. The aim of this section is to outline a road map for the study of the problems and the implementation of the most effective solution within the time constraints of the start of the proposed experiment.

This section is based on the experience of the PH/MIC group as well as the PH/ED group at CERN who worked on the ALICE silicon pixel detector (SPD). The SPD project has required complex front-end electronics in the  $0.25 \mu\text{m}$  CMOS process, together with state-of-the-art techniques to match the severe constraints in material budget (wafer thinning, etc). The CERN-PH/MIC and PH/ED groups have been responsible for the design of the SPD pixel chip and are studying high speed designs that could be applicable to this project.

#### 1. Pixel detector technology

The only pixel technology sufficiently mature for consideration in the time frame of the project is the one based on hybrid pixels. Each pixel cell on the silicon sensor is connected to a pixel cell on the readout chip using a micro solder point (bump-bond

e.g. made of Pb-Sn). Monolithic pixels have been investigated in recent years but have not yet reached the stage at which they could be considered a realistic option. More recently, a detailed study has been started of devices based on the deposition of a layer of amorphous silicon or other suitable material on the surface of a readout chip. Although promising results have been obtained, this technology is still in its infancy. It is proposed, therefore, to use hybrid silicon pixel detectors and to optimize the sensor and readout chip thicknesses in order to comply with the material budget constraints. In the ALICE SPD, one of the most advanced current designs, pixel chips of  $150\text{ }\mu\text{m}$  thickness (thinned 200 mm diameter wafers) are bump-bonded to  $200\text{ }\mu\text{m}$  thick Si sensors. To reduce further the material budget, bump-bonding of even thinner silicon elements is required.

## 2. Silicon sensors

The sensor thickness will have to be optimized taking into account the trade-off between speed and collected charge for different designs. Detailed simulations and direct measurements are required. Sensor wafers of thickness  $\leq 200\text{ }\mu\text{m}$  can be obtained from commercial suppliers but production and bump-bonding yield need to be investigated; this work could start immediately using available pixel chips. Radiation hardness is another critical issue to be studied; the experience gained in the development of Si tracking detectors for the experiments at the LHC will be very valuable. A 150 ps time resolution seems realistic if the charge detected by the sensor is collected within few nanoseconds. An intense effort should be devoted to investigate high speed silicon sensors.

## 3. Pixel chip

The pixel chip will be a mixed-signal ASIC of high complexity. The chip architecture will require a detailed study and thorough simulation. The most challenging functional blocks will be:

- (a) fast preamplifier and shaper
- (b) low time walk discriminator
- (c) high resolution TDC.

Possible chip and TDC architectures have been investigated [26]. simulations using the hardware description language VHDL to determine the efficiency for different con-

figuration have been performed.

Possible TDC implementation are:

- TDCs based on delay line elements, where a reference signal (such as the clock) is propagated through the delay line and the status of all delay elements and thus the propagation of the first signal in the delay chain is stored in a register at the arrival of the signal to be timed. These designs are based on the principle that the variation of the delay elements is small. This basic design principle has been employed in the HPTDC design by the micro electronics group at CERN[27]. Using this architecture the TDC is located at the periphery of the pixel chip and all pixel signals coming from the discriminators are routed across the matrix to the TDC. As neither routing space nor placement space on the chip allow the implementation of one TDC element per pixel, a given number of pixels must be combined to a super-pixel segment and share one TDC element.
- An alternative approach is to propagate the discriminator signal through the delay chain and store the status of the delay chain upon arrival of a reference clock signal. The delay chains are operating only when a pixel cell has been hit. As the size of the delay chain is larger than the pixel size, again several pixels would share one TDC element.
- One TDC per pixel cell might be implemented using analog circuitry based on capacitors as reference elements.

In any of these options each channel will need calibration. As the beam profile is not uniform the individual pixel hit rate is varying. The architecture incorporating the combination of several pixels to a super-pixel results in a lower average hit rate arriving at the TDC. Studies of pixel segmentation to create super-pixels must show how the TDC design data rate can be reduced compared to maximum rate. In addition, it must be considered that the required time resolution needs a time walk compensation.

The estimated data rate produced inside the chip is  $\sim 30$  Gbit/s for each SPIBES station, for an average particle rate of  $\sim 60$  MHz  $\text{cm}^{-2}$ , 100 MHz clock frequency and 34 bits per data word (two time measurements and the address of the hit pixel). A trigger matching unit will provide a data rate reduction factor of  $\geq 10$ .

Due to the given specifications the pixel size, the time resolution and the data rate are strongly interconnected. The implementation of a pixel chip for the Gigatracker must meet different requirements and an optimum must be found.

Chip test structures must verify the principle and give information concerning the influence on the analogue circuitry caused by the digital data read-out and processing via the chip substrate. A preliminary design of each block will be done in the  $0.25\text{ }\mu\text{m}$  process using Multi Project Wafers (MPW) runs for cost considerations. For the full design, the speed and device density requirements might need moving to the  $0.13\text{ }\mu\text{m}$  process. The study of this technology has started recently and the design of such a complex structure is expected to require an effort of several man-years.

#### 4. Front-end hybrid

The ALICE SPD pixel chips are connected to a substrate carrying power distribution, signals and data buses. The substrate is a low-mass multilayer flex, such as polyimide/aluminum. In addition to the pixel chip, the readout electronics is connected directly to the sensor/readout chip assembly for clock and trigger distribution, data multiplexing and transmission, and controls. This requires one or more ASICs in the immediate vicinity of the pixel chips, possibly on the same substrate. For this project, it would be desirable to have the power, data buses and the multi-chip-module (MCM) functionality placed at the periphery of the detector plane, in order to minimize the material budget. The feasibility of such a scheme needs to be investigated, including the implications for cooling.

Considerable experience has been gained in the developments of the Si trackers for the LHC experiments.

#### 5. Mechanics and cooling

The power dissipation in the pixel chip may reach  $\sim 2\text{ W/cm}^2$ , possibly more on account of the high speed required. An efficient cooling system is mandatory. This is of course not easily compatible with the low mass requirements. It is planned to study the feasibility and performance of thin substrates consisting of high thermal conductivity carbon fiber composites, cooled at the periphery to reduce the material to the minimum. Expertise has been gained in the ALICE SPD on composite materials and two-phase cooling systems. Other advanced technology solutions, such as micro-channel cooling, are being developed elsewhere and might be considered if compatible with the detector layout.

#### 6. Timescale and resources

A preliminary time scale and cost of the SPIBES detector, based on the experience

gained in other silicon pixel detector projects and on current engineering run prices, is given in table 7. Two options are listed: technology A (based on  $0.25\text{ }\mu\text{m}$  CMOS process) and B (based on  $0.13\text{ }\mu\text{m}$  CMOS process). The baseline technologies are essentially those already adopted in the most advanced current designs, further extended to the limits of feasibility. The pixel read-out chip might require developments in the  $0.13\text{ }\mu\text{m}$  CMOS process. New solutions may have to be worked out for the hybrid and cooling. Preliminary work should start without delay, particularly on the definition and simulation of the front-end architecture. The front-end ASIC development will require the contribution of several experienced designers for a period of two to three years. Testing is a key activity that requires close collaboration of physicists and designers. A good definition of the DAQ environment is needed to develop a matching back-end readout and an efficient calibration system.

## 7.4 Micromegas-type TPC

The multiple scattering caused by the material of the last station of the Gigatracker impacts directly on the resolution of the opening angle between the incoming kaon and the charged pion and hence it has to be minimized. The state-of-the-art gaseous detector developed for NA48/2 couples excellent space resolution to a minimal material budget. The NA48/2 detector, called KABES, is made of MICROMEGAS-type chambers read-out in TPC mode. The following performance has been achieved [16] [28].

- Position Resolution  $\approx 80\text{ }\mu\text{m}$
- Time resolution  $\approx 0.7\text{ ns}$
- Rate per micro-strip  $\approx 2\text{ MHz}$

In this proposal, such a detector must perform the tracking of a 1 GHz hadron beam (about 10 times more intense -per unit area- than the combined positive and negative beams of NA48/2), contributing less than  $10\text{ }\mu\text{rad}$  to the angular resolution. Effort has to be made to:

- Shorten the detector signal employing a micro-mesh with thinner amplification gap.
- Improve the time resolution.
- Reduce the double pulse resolution, sampling each strip continuously by means of 1 GHz FADC.

Table 7: Estimate of cost and spending profile for the Gigatracker SPIBES based on current engineering run prices.

	<b>2005</b>	<b>2006</b>	<b>2007</b>	<b>2008</b>	<b>2009</b>
	kCHF	kCHF	kCHF	kCHF	kCHF
<b>Sensors, support, readout</b>					
sensors	22.5	37.5	75		
test instrumentation	15	45	15		
tooling	15	30	30		
support and cooling		30	30		
readout and PCB	15	30	45		
<b>Sensors, support, readout subtotal</b>	<b>67.5</b>	<b>172.5</b>	<b>195</b>		
<b>Common electronics developments</b>					
PreAmp, Discr 0.25μm (MPW)	15	15			
test structures (I) 0.13μm (MPW)	82.5				
TDC 0.13μm (MPW)		82.5	82.5		
bump bonding (400Euro/placement)	15	22.5	75	75	
<b>Common electronics dev. subtotal</b>	<b>112.5</b>	<b>120</b>	<b>157.5</b>	<b>75</b>	
<b>Microelectronics tech. choice A</b>					
FE 0.25μm ( 2 eng. runs)			375		
FE 0.25μm ( production run)				150	
<b>Microelec. tech. choice A subtotal</b>			<b>375</b>	<b>150</b>	
<b>Microelec. tech. choice B</b>					
test structures (II) 0.13μm (~40 mm <sup>2</sup> , MPW)		225			
FE 0.13μm ( 2 eng. runs)			1455		
FE 0.13μm ( production run)				150	
<b>Microelec. tech. choice B subtotal</b>		<b>225</b>	<b>1455</b>	<b>150</b>	
<b>A totals</b>	<b>= 1425 kCHF</b>	<b>180</b>	<b>292.5</b>	<b>727.5</b>	<b>225</b>
<b>B totals</b>	<b>= 2730* kCHF</b>	<b>180</b>	<b>517.5</b>	<b>1807.5</b>	<b>225</b>

- Consider a smaller micro-strip pitch.

Another aspect that has to be taken into account is the space-charge effect due to ion build-up. The design of the experiment relies on the ability of the KABES detector to function at the required intensity. To a large extent this was already validated in 2004 during the test which took place at the end of the NA48/2 data taking.

For the proposed experiment this gaseous detector is dubbed Flash-TPC because, in order to achieve the required double pulse resolution to make the pattern recognition feasible in a detector without intrinsic bi-dimensional segmentation, each micro-strip will be read by FADCs of the type or similar to those employed for the proton tagger of the original NA48 experiment. The pattern recognition is complicated by the long drift time (about 600 ns) and the time resolution is unlikely to reach 150 ps because of gas diffusion. For these two reasons the FTPC is preceded by the fast pixel detectors (SPIBES).

## 8 PHOTON VETOES

To suppress the dominant background originating from the decay  $K^+ \rightarrow \pi^+\pi^0$  to the specified level, the average inefficiency for the rejection of the  $\pi^0$  should be  $\approx 10^{-8}$ . To do so, photon vetoes with hermetic coverage up to 50 mr for photons originating from kaon decays occurring in the decay region (from 5 to 65 metres after the final collimator) have to be envisaged. With such a configuration, only  $\approx 1.6\%$  of the events have one photon from  $\pi^0$  left undetected. The geometry of the experiment suggests to partition the detector into three different angular regions instrumented by three different detector technologies.

- Large angle vetoes (ANTI), hermetic between 8.5 mr and 50 mr, distributed along the decay volume spaced by 6 metres in the upstream region and by 12 m downstream, according to the layout in Figure 9.
- Liquid krypton calorimeter (LKR), covering angles between 1 and 8.5 mr.
- Small angle vetoes, covering the region down to zero degrees (SAC) and the zone around the inner radius of the RICH (IRC1) and of the LKR (IRC2) calorimeter, with suitable overlap in the angular acceptance to cover the beam pipe and with an inner radius smaller than that of the beam pipe.

The kinematics of the  $K^+ \rightarrow \pi^+\pi^0$  decay is such that a low energy photon at large angle (which is typically more difficult to detect) is paired with a high energy one hitting the LKR or the small angle vetoes where very high detection efficiency can be expected.

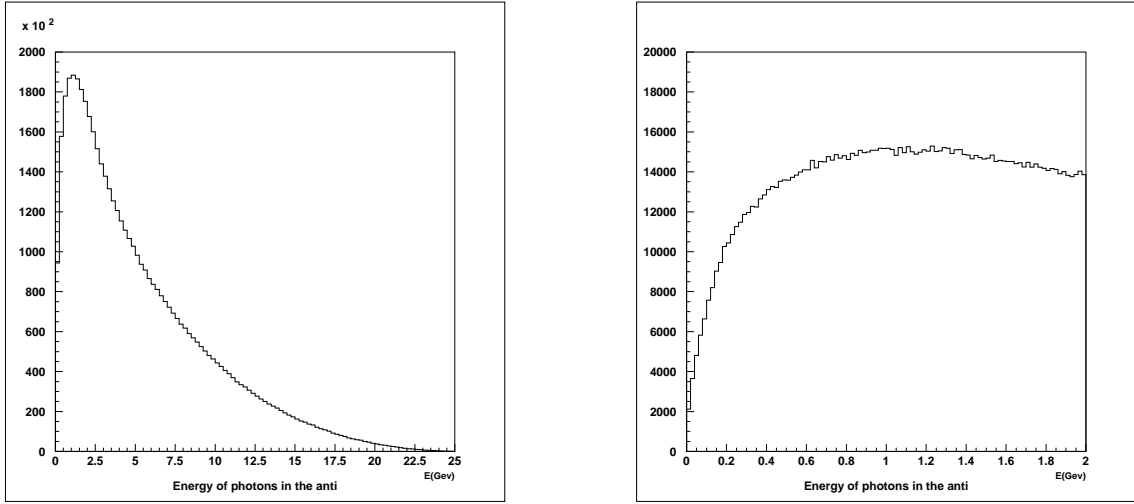


Figure 21: Distribution of energy in the ANTI ( the RHS is a zoom).

## 8.1 Considerations about the inefficiency

A simulation of the decay kinematics and of the geometrical acceptance has been made, to compute an average photon detection inefficiency using two different definitions of the energy dependence of the inefficiency of the single counters (see Table 8): the first realistic and the second based on the values used in the CKM proposal [29] and those obtained in several measurements done by E787, ES147, ES171 [30].

The results shown refer to  $10^7 K^+ \rightarrow \pi^+\pi^0$  decays generated. The energy of the photon in the ANTI ranges from less than 10 MeV to 25 GeV (Figure 21). The minimum photon energy in the calorimeter is 1 GeV (Figure 22), while in the IRC and SAC it is  $\approx 6$  GeV (Figures 23 and 24).

The average  $\pi^0$  inefficiency is reported in Table 9, with and without imposing a cut on the momentum of the charged pion between 8 and 40 GeV. We also report the fraction of events with an inefficiency of more than  $10^{-7}$  which mainly contribute to the average inefficiency. This fraction is defined as the ratio between the number of inefficient events and the total number of the accepted events. An in-depth look at inefficient events shows that these are characterized by one low energy photon either outside the acceptance of the ANTI or inside it, but with very low energy and high inefficiency. The other photon hits the LKR calorimeter with an energy larger than 35 GeV or the first IRC with an energy larger than 60 GeV. It is then mandatory to have an inefficiency of the LKR better than  $10^{-5}$  at those energies for a lower contribution to the average  $\pi^0$  rejection inefficiency.

This parameter for the LKR calorimeter is even more stringent than the inefficiency at low

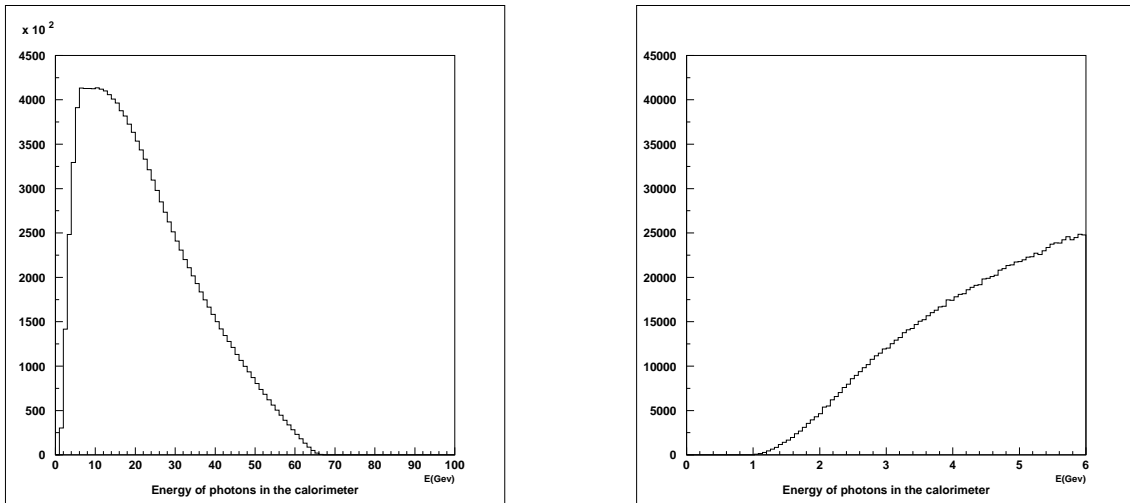


Figure 22: Distribution of energy in the LKr.

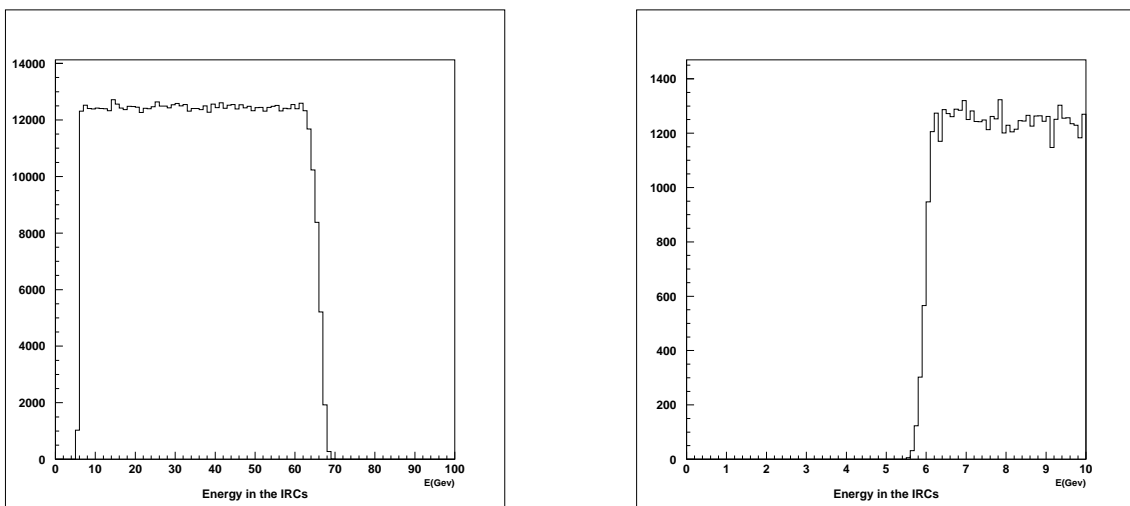


Figure 23: Distribution of energy in the IRCs.

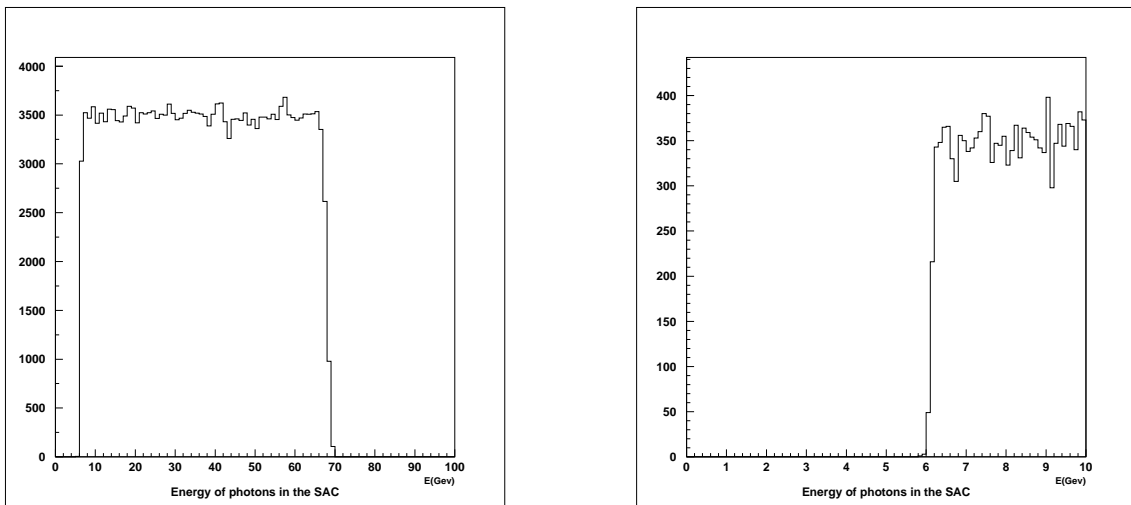


Figure 24: Distribution of energy in the SAC.

	Detector and energy range	Photon detection inefficiency
Realistic choice	ANTI E < 50Mev	1
	ANTI 50 MeV < E < 1 GeV	$10^{-4}$
	ANTI E > 1GeV	$10^{-5}$
	LKR E < 1Gev	$10^{-3}$
	LKR 1 GeV < E < 3 Gev	$10^{-4}$
	LKR 3 GeV < E < 5 Gev	linear btw $10^{-4}$ and $10^{-5}$
	LKR E > 5Gev	$10^{-5}$
	IRC1, IRC2, SAC	$10^{-6}$
Optimistic choice	ANTI E < 100Mev	0.1
	ANTI 100 MeV < E < 250 MeV	$3 \cdot 10^{-4}$
	ANTI 250 MeV < E < 1 GeV	linear btw $3 \cdot 10^{-4}$ and $10^{-6}$
	ANTI E > 1GeV	$10^{-6}$
	LKR E < 1Gev	$10^{-4}$
	LKR 1 GeV < E < 3 Gev	$10^{-5}$
	LKR 3 GeV < E < 5 Gev	linear btw $10^{-5}$ and $10^{-6}$
	LKR E > 5Gev	$10^{-6}$
	IRC1, IRC2, SAC	$10^{-6}$

Table 8: Inefficiency figures used in the simulation.

	Average inefficiency	Fraction of ineff. events
Conservative choice		
Without pion momentum cut	$1.6 \cdot 10^{-7}$	1.59%
With pion momentum cut	$3.3 \cdot 10^{-8}$	0.34%
Realistic choice		
Without pion momentum cut	$1.5 \cdot 10^{-8}$	1.51%
With pion momentum cut	$3.0 \cdot 10^{-9}$	0.28%

Table 9: Total average inefficiencies.

energy: in fact, one photon hitting the calorimeter with an energy in the range 1-5 GeV has the other photon hitting either the LKR calorimeter, the IRCs or the SAC with higher energy or the ANTI with an energy between 0 and 1.5 GeV (Figure 25): the fraction of photons in the ANTI with energy below 300 MeV, where the inefficiency starts to increase, is less than 3%. In addition, if one could detect all the photons not hitting the vetoes (about 1% of the total) with 1% inefficiency, the average  $\pi^0$  inefficiencies in Table 9 would drop respectively to  $9.3 \cdot 10^{-9}$ ,  $6.2 \cdot 10^{-9}$ ,  $3.9 \cdot 10^{-10}$ ,  $2.1 \cdot 10^{-10}$ .

A detailed simulation, using GEANT4, of the possible detector structures has started, with the aim of evaluating the inefficiency for the photon detection at different energies, impact points and angles. We feel confident that the current status of the GEANT4 physics description is sufficiently accurate: indeed we have done a simulation of structures (2mm Pb/6mm Scintillator) for which experimental results on the inefficiencies exist [31] and the comparison in Figure 26 shows good agreement.

A strong point of the proposal is that the LKR exists and its performance has a veto can be tested in situ employing kaon decays from the current K12 beam. In fact, to this purpose, we have accumulated a data sample in 2004 but more data, collected without zero suppression, should be accumulated, for example during the 2006 SPS proton run. It is also planned to test different prototypes of the ANTI counters at energies lower than 1 GeV, investigating the use of a tagged photon beam to compare the different solutions.

## 8.2 Large angle vetoes (ANTI)

The large angle vetoes will cover a surface of about 27 m<sup>2</sup>: besides the requirement of efficiency, the cost is also an important factor. The design is based on a lead-scintillator sandwich with WLS fiber readout.

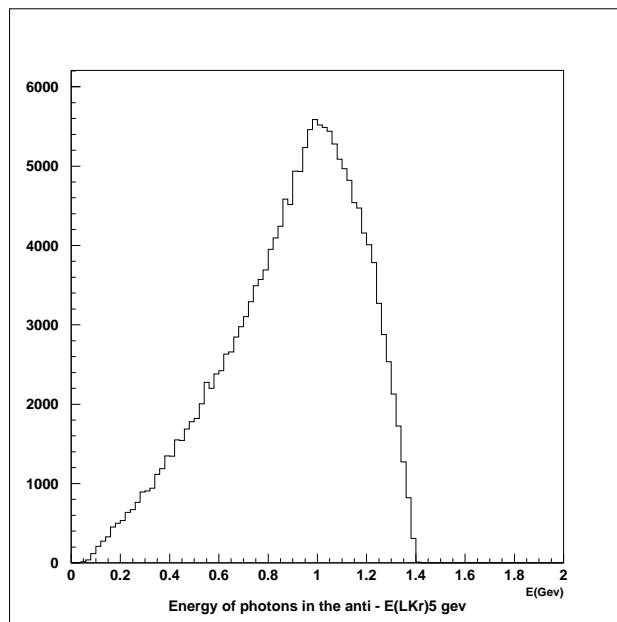


Figure 25: Energy in the ANTI when  $1 \text{ GeV} < E_{LKR} < 5 \text{ GeV}$ .

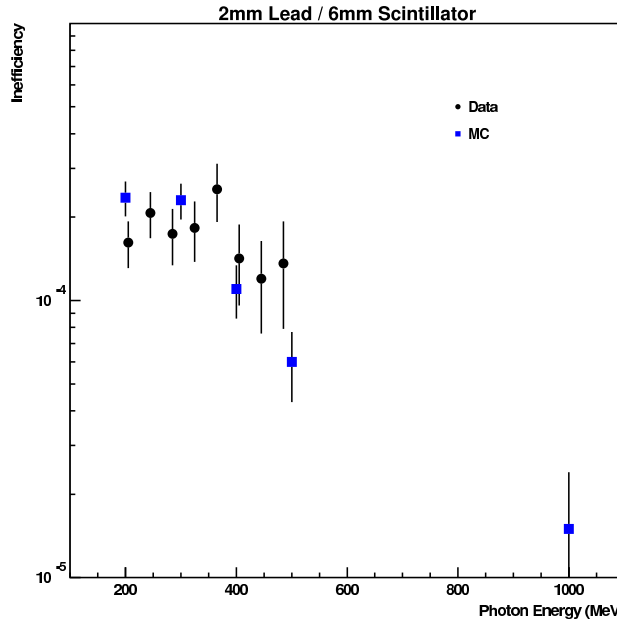


Figure 26: Data-MC comparison for 2mm Pb/6mm Scintillator.

### 8.3 Geometry of large angle vetoes

It is planned to equip the decay tank with 13 calorimeters, 16  $X_0$  deep, as shown in Figure 9. Each counter is composed of 80 layers of 5 mm scintillator and 1mm lead sheets, arranged in annular coronas (Figure 27). Each corona is divided azimuthally into 16 sectors, each one covering 22.5 degrees in  $\phi$ .

Consecutive layers of each sector are staggered to avoid cracks. Each scintillator tile has grooves where 8-10 WLS fiber are glued. The way of making the grooves will be a matter of optimization: the simplest one with few radial or parallel grooves should be compared, in terms of light yield and uniformity of light collection, with a solution with curved paths for the fibers on the scintillator surface. Fibers from alternate layers are collected by a photomultiplier to provide a redundant read-out. An additional segmentation of the readout is made using a pair of PMs (green extended photocatode) for the front and a pair for the back. This readout setup will give a segmentation front/back which could be used i.e. in the trigger to separate photon showers (with a greater amount of energy in the front part) from the muons from the halo which will give an uniform signal along the path. Muons will play a significant role to monitor the entire ANTI system.

The technique of scintillator plus WLS fibers, with a proper construction, will give around 20 photoelectrons/MIP for each layer.

### 8.4 Mechanical design

In Figure 28 we show a sketch for the mechanical layout of the large angle photon vetoes. As it is already mentioned in the section 4.4, the vacuum in the decay tank should be kept at a value of at least  $3 \cdot 10^{-7}$  mbar, in order to minimize background due to beam-gas interactions. A design of the veto counters as in the original NA48, with scintillators placed in pockets outside the thick decay tube, would lead to insufficient photon detection efficiency. It is therefore necessary to install the counters inside the vacuum tank, separating them from the high vacuum region with a thin wall in order to minimize the effect of scintillator outgassing. The stack of scintillator and lead is supported by a  $\approx 1$  cm thick back plate through a set of rods going from the front to the back. The plate is welded to a special section of the vacuum tank, connected to it via flanges and O-rings. A thin layer of 0.8 mm Al to cover the front and the lower part of the detector is glued to the back plate and to a smaller plate on the front. This detector volume is pumped through an aperture on the lateral surface of the section to a manifold connecting all the ANTI pockets. The manifold is also connected,

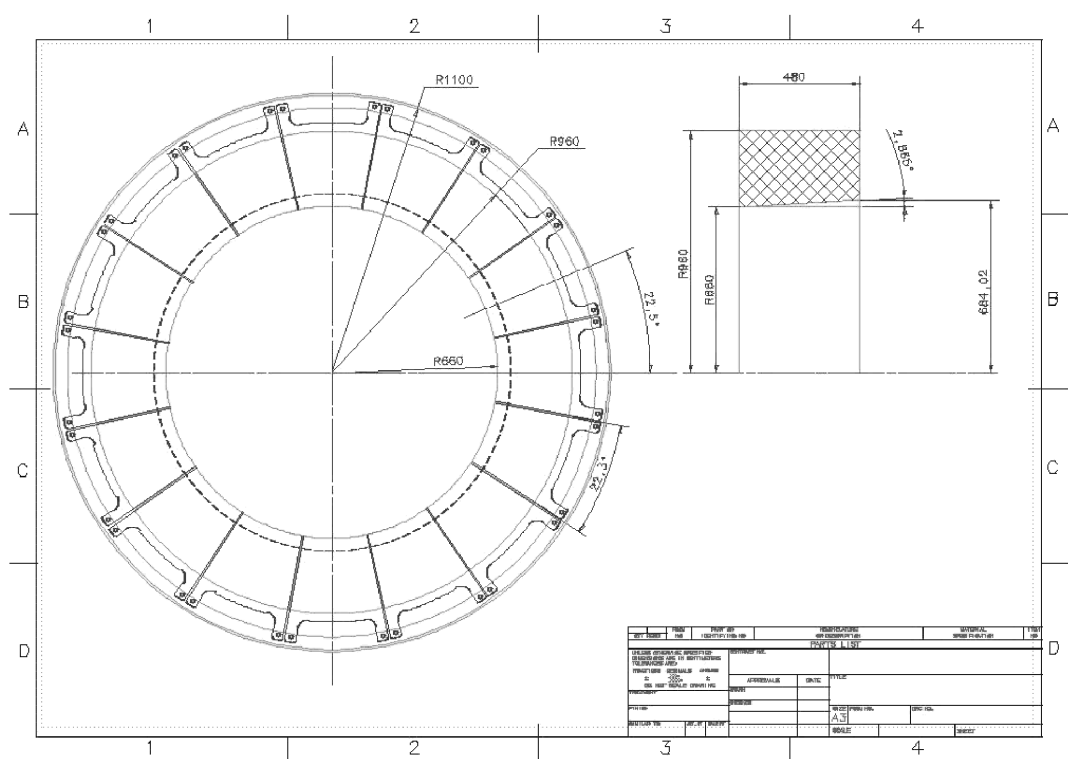


Figure 27: Transverse section layout of an anti ring.

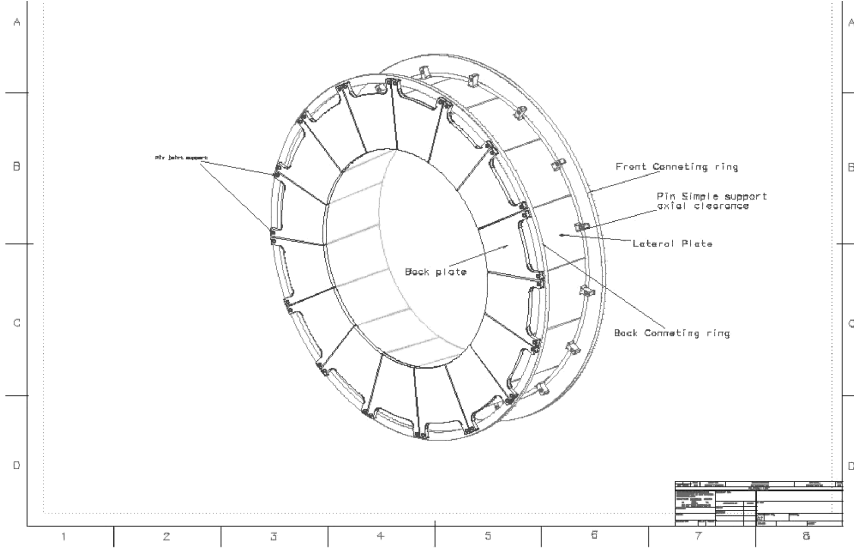


Figure 28: Mechanics of an anti ring.

through a calibrated leak, to the main volume to control the pressure difference. Fibers from the detector are glued to 4 plexiglass cylinders passing through the section with a vacuum seal. The other base of the cylinder is connected to the phototube outside the vacuum. An additional plexiglass feed-through is planned to bring to the PMs a light signal for calibration and monitoring.

#### 8.4.1 An alternative structure

We are also evaluating a design with a lead structure with embedded scintillating fibers (known as "spaghetti calorimeter"), modeled on the calorimeter of the KLOE experiment [32]. Such a detector can be built by stacking together a series of layers composed of a thin lead foil, with a regular array of machined grooves in which the scintillating fibers are aligned and glued (Figure 29). This kind of arrangement guarantees the most uniform filling, and thanks to the very thin absorber, an almost homogenous structure with good energy and time resolution [32, 33]. A modular detector can be built with geometries not limited to straight prisms, such as a C-shaped one (Figure 30), only limited by the minimum bending angle of the fibers.

Reading from both sides of the fibers allows the determination of the impact point (with  $\approx 1$  cm accuracy at 1 GeV, given the timing performances), deriving it from the time difference between the two ends, provided that the time measurement (TDC) is included in the read-

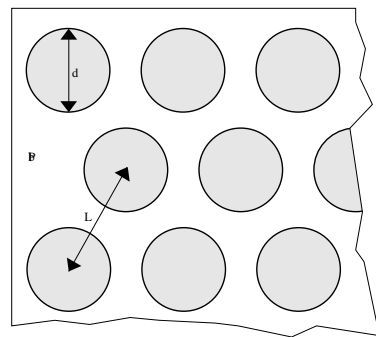


Figure 29: Schematic view of the cross section of a lead/scintillating fibers spaghetti calorimeter:  $L$  is the distance between the adjacent fibers, while  $d$  is the fiber diameter.

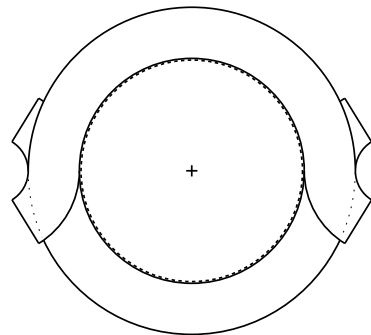


Figure 30: Schematic view of a possible layout of C-shaped lead/scintillating fibers spaghetti calorimeter modules.

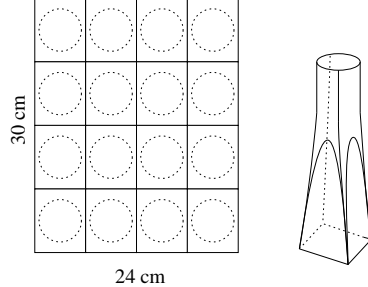


Figure 31: Schematic view of a possible readout with Winston concentrator light guides.

out electronics. The readout granularity can be easily adjusted if the light collection is performed by means of light guides. Of course the efficiency will be limited at least by the ratio of the photocathode area to the cell area. The longer the single module the smaller will be the total number of photomultiplier tubes and electronics channels needed. This has to be balanced with the increasing length of the module, thus with the reduction of the light yield due to attenuation length of the fibers (3 m).

Considering a cell size of  $6 \times 7.5 \text{ cm}^2$ , read out by 2 inch photomultiplier tubes (standard bialkali), the different rings will then be equipped with a grid of  $4 \times 4$  (smallest rings) to  $4 \times 6$  (largest ring) phototubes per side (Figure 31). Taking into account the experience of the KLOE calorimeter, a plexiglas Winston concentrator light guide with an area ratio of 2.7 should provide a light collection efficiency in excess of 90%, since the refraction indices for the fiber core, cladding and light guide material are such that  $n_{\text{core}}/n_{\text{cladding}} < n_{\text{plexiglas}}$ . Another important parameter is the light yield: for blue-emitting plastic scintillating fibers (Bicron type BCF-12 or the Kuraray type SCF-81) this is of the order of 5 photo-electrons (p.e.) when a 1 mm fiber is crossed by a minimum ionizing particle (at 1 m from a standard bialkali photocathode) [34]. Taking into account a trapping efficiency of the fiber of 3% ( $n_{\text{core}} = 1.6$ ,  $n_{\text{cladding}} = 1.49$ ), a maximum light attenuation when the photon hits a 4 m long module of about 50%, a light guide efficiency of 90% and a photocathode quantum efficiency of 25%, a light yield of 24 p.e./MeV per side for a minimum ionizing particle can be estimated.

Since the energy deposited by minimum ionizing particles is equivalent to that of 30 MeV photons, this translates into 0.8 p.e./incident MeV for photons. The effect of a threshold of a few p.e. on the inefficiency should be small (as compared to sampling fluctuations, punch-through and other effects such as the photonuclear interactions) above a few tens of MeV.

It is planned to make an extensive series of tests on the characteristics of the base elements, like

- Light yield of various types of scintillator plates
- Performances of scintillating fibers
- Measurements of degassing rates of materials in vacuum

Moreover, it is planned to build prototypes of both solution with extensive tests in the lab and on a photon beam to assess the good and bad points of both solutions in term of inefficiency, time resolution, trigger capabilities and costs.

#### 8.4.2 Readout

The signals from the photomultipliers should be processed to give a fast trigger veto signal, to have a precise measurement of the time of the photon and to make a pulse height analysis on a time window across the event. The signal expected from the PMs should not need to be amplified. However a splitter might be needed to provide an output for the trigger and one or more outputs for the digitization. The trigger logic could be implemented either with a traditional logic (discriminators, fast logic) or with a more flexible system based on Flash ADCs with a clock period of around 4-6 ns, coupled to FPGAs where the trigger logic is implemented and which provide a trigger decision every clock cycle. The readout of the  $\approx 1000$  channels could be done with the same type of hardware which will be designed for the LKR calorimeter, with a proper adjustment of the shaping time. The definition of the shaping time and of the digitization clock should not be a problem, as the rate for each channel is low and double pulse resolution will not be an issue: a longer shaping could allow to use 40 or 80 Mhz without degrading time resolution.

### 8.5 Cost estimation

The cost estimation for the ANTI is reported in Table 10. The first estimate of the cost for the KLOE like structure is similar, keeping into account the cost of the fibers in place of scintillator and WLS fibers.

### 8.6 Liquid Krypton calorimeter

It is intended to exploit the LKR calorimeter as a photon veto in the intermediate angular region. The very good performances of the calorimeter [35] [36] will be used also to precisely

Item	Cost (kCHF)
Scintillator	1700
Lead	100
WLS fibers	400
Photomultipliers	700
Mechanics	600
High voltage	300
Trigger and readout	400
Total	4200

Table 10: Estimation of the cost of the ANTI-counters.

measure the electron energy in order to reject the background from  $K^\pm \rightarrow \pi^0 e^\pm \nu$ .

### 8.6.1 Estimate of the inefficiency

It is necessary to have an inefficiency in the photon detection of  $10^{-5}$  above 1 GeV and in particular better than  $10^{-5}$  above 35 GeV. Data taking for a measurement of the inefficiency has been done in 2004, adding a small angle calorimeter in the forward region and selecting  $K^+ \rightarrow \pi^+ \pi^0$ . However the statistics collected is not enough and the zero-suppression mechanism used was not optimized for vetoing.

We are considering to collect more data in 2006, reading the calorimeter without zero suppression to reduce the inefficiency at low energies. A detailed beam request for 2006 is being prepared. In parallel, we are studying the LKR photon detection inefficiencies with other data sets collected in NA48/2, like  $K^\pm \rightarrow \pi^+ \pi^0 \pi^0$  or  $K^\pm \rightarrow \pi^+ \pi^0 D$ , to extract inefficiency figures.

Another possible limitation to the low energy inefficiency was thought to be the contribution of the photonuclear interactions in the material in front of the LKR active volume (mainly a 7 cm Stesalite plate). A GEANT4 simulation of this structure has shown however that the contribution to the inefficiency is less than  $2 \cdot 10^{-6}$ .

### 8.6.2 New readout

The current LKR read-out electronics is housed in Fastbus modules. A new readout electronics for the calorimeter, possibly replacing also the current transceivers is being considered to cope with the discontinued support for Fastbus electronics at CERN.

An interesting possibility is to use a generalised version of the integrated circuits used in the ALICE TPC readout. This development, done by CERN in collaboration with several partners, may lead to a compact design, with all the features needed, including the digital processing power needed either to zero suppress the data or to make a lossless compression of them. We feel indeed mandatory to be able to read all the cells of the calorimeter for each event and make a smart zero suppression in software. Network bandwidths and CPU power are not anymore a bottleneck. A first estimate for the cost of 15000 read-out channels is about 1500 kCHF.

### 8.6.3 Upgrade of the cryogenics slow control

The use of the LKR calorimeter for the proposed experiment implies an upgrade to the cryogenics control system. This system, built in 1995, despite its robustness and very good performance, suffers from several problems:

- The front-end hardware has still some spare parts, but there is no more expertise at CERN
- The supervision software (FactoryLink) is obsolete at CERN since several years
- The supervision hardware is not maintained anymore

Different possibilities have been discussed with AT/ECR and the more realistic one is a complete remake (HW and SW) of the system, with support and consultancy from AT/ECR and with a manpower contribution from the Collaboration. The estimate of the cost is 500 kCHF.

## 8.7 Small angle vetoes

There will be two types of small angle vetoes: two covering the beam tube which will go through the calorimeter and the RICH (IRC 1 and 2) and one covering the region down to 0 degrees after the MAMUD detector, where the charged beam has been deflected (SAC). The two types of detector will be at least  $16 X_0$  deep in order to keep the punch through probability below  $10^{-7}$ . We are actually comparing two solutions: the first based on shashlyk technique [37] with a sandwich of lead and scintillator and longitudinal WLS fibers and the second based on PbWO<sub>4</sub> crystals. Both solutions will provide photon detection inefficiencies of  $10^{-6}$  or better at the high energies involved. In both cases, for IRC1 and IRC2, the more

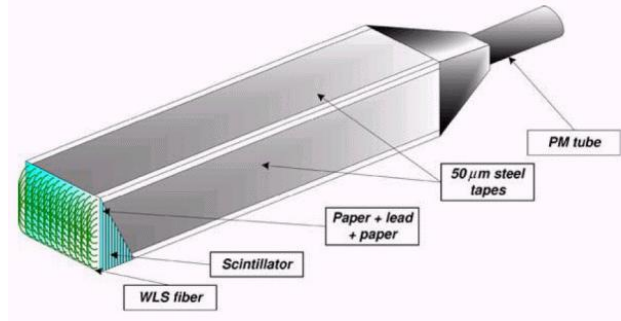


Figure 32: The concept of a shashlyk calorimeter.

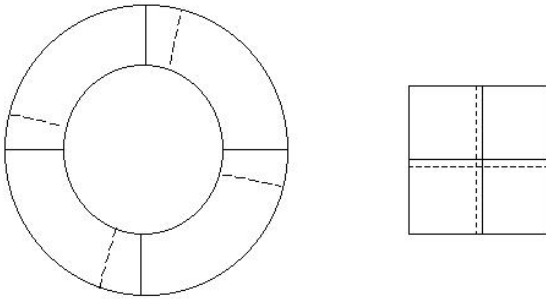


Figure 33: Staggering of consecutive layers.

challenging problem is the connection of the detector (a ring around the beam pipe) to the HV power supply and the readout electronics.

### 8.7.1 Geometry of the detectors

- Shashlyk technique: A suitable structure will be made with 100 layers of 1mm (Pb) + 2mm (Sci), for a total of  $\approx 17 X_0$  and with a fiber spacing of 9.5 mm. The readout will be made with a PM on the back (Figure 32). For IRC1 and IRC2 the lead and scintillators will be shaped in circular coronas sectors (inner diameter 14 cm, outer diameter 24 cm) which will be mounted staggered in order to avoid cracks. Similarly, for the SAC, the successive layers will be staggered after a proper cutting (Figure 33).
- PbWO<sub>4</sub> structure: A first proposal for IRC1 and IRC2 has 3 rings (inner and outer radius of 7 and 12 cm) longitudinally adjacent, each one made of 16 crystals with a trapezoidal shape (Figure 34). The readout will be made either using small APDs on the internal face or using PMs on the outside face. This solution should be improved,

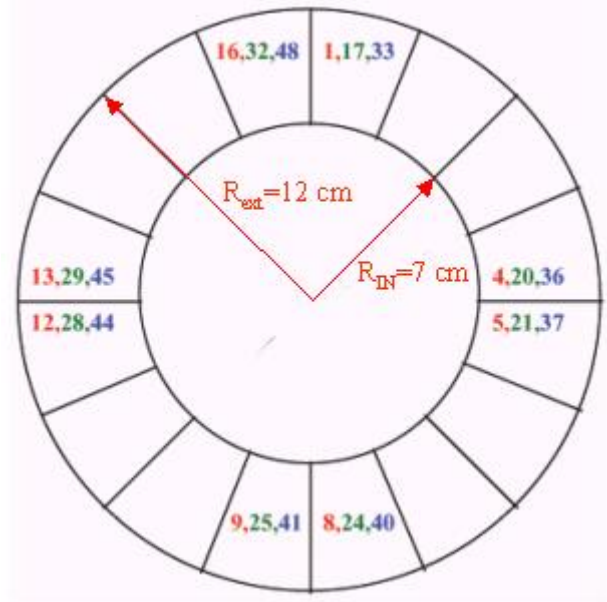


Figure 34: *Layout of the crystals in the IRCs.*

as the proposed position of the readout devices is not acceptable, because in one case APDs will extend too much into the beam and in the other there is too much material (PMs, etc.) in front of RICH and calorimeter at low angles. The optimal possibility is to read the crystals from the face opposite to the particle entrance. To fulfill this requirement for the readout, a design should be envisaged with only one ring with suitably shaped crystals to avoid cracks, for example with crystals whose lateral faces are bent with respect to the longitudinal direction. The implementation of the SAC is done with standard prism crystals, arranged in a  $8 \times 8$  matrix and installed with an angle between its axis and the beam to avoid cracks.

### 8.7.2 Mechanical design

IRC 1 will be supported by a light carbon fiber tube which will be connected to the flange of the beam pipe. IRC 2 will be mounted on a section of the beam pipe which will be put in place and welded to the beam tube. A more detailed study will be done on the possibility to support the detectors with thin wires across the area of the RICH and of the LKR calorimeter. The SAC could be inside a closed box hung in the proper position downstream of MAMUD. Weights should not be a problem: in both solutions, IRC1 and IRC2 will be  $\approx 40$  kg and the SAC  $\approx 55$  kg.

### 8.7.3 Readout

The readout of the small angle vetoes could follow the same scheme as the one for the large angle vetoes. Indeed, a standardization of the electronics is more than recommended

### 8.7.4 Costs

The estimation of the costs for the materials needed for the two solutions varies from 150 kCHF to 300 kCHF, depending on the type of technology and the type and number of photodetectors. The cost of the mechanics will be around 40 kCHF. We estimate that the read-out electronics and HV system will cost 10 kCHF.

## 9 STRAW TRACKER

To minimize the multiple scattering of the outgoing pion it is proposed to operate the magnetic spectrometer in vacuum upstream the decay region. This means that the decay and spectrometer regions are not separated and share a common vacuum volume. A straw tracker is considered as one of the most promising detectors to be operated in vacuum. In addition, the straw tracker could be designed without internal frames and flanges. The latter is rather important to diminish the background arising from the beam halo particle interactions. The proposed design of the straw detector is partially based on the experience accumulated during the production and exploitation of a similar straw trackers built for the COMPASS and ATLAS experiments. The straw tracker has to be made of several straw planes (layers). One view consists of two staggered planes (double layer), to solve the left-right ambiguity in hit coordinate reconstruction as shown in Figure 35. All straws in a double layer are glued together to provide the necessary rigidity and gas tightness. To fit easily into the decay volume, 2.3 m diameter tube, an octagonal shape is proposed for each double layer (view). The straw planes are fixed to aluminium frames also having octagonal shapes. A central region of 10 cm width, corresponding to the (deviated) beam passage in each of the views, is not covered by the straws (see Figure 36). The corresponding acceptance loss is less than 10% while the total muon halo rate in a plane of straws is less than 10 MHz. All the double layers (views) have identical design and contain straws with a maximum sensitive length of 2300 mm. Four views are coupled to form a chamber. Each view is rotated with respect to another by 135 degrees. Such chamber measures four coordinates (X/Y/U and V) of particle hits. The central part of the chamber has areas with different number of measured coordinates. As an example, Figure 37 shows the central part of a four-

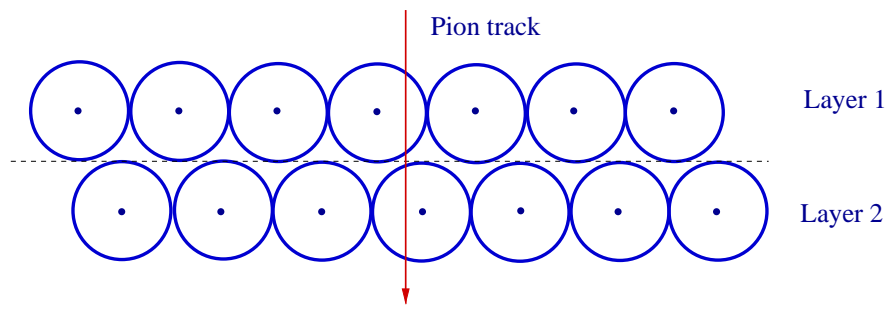


Figure 35: A cross section schematic view of a double layer (view).

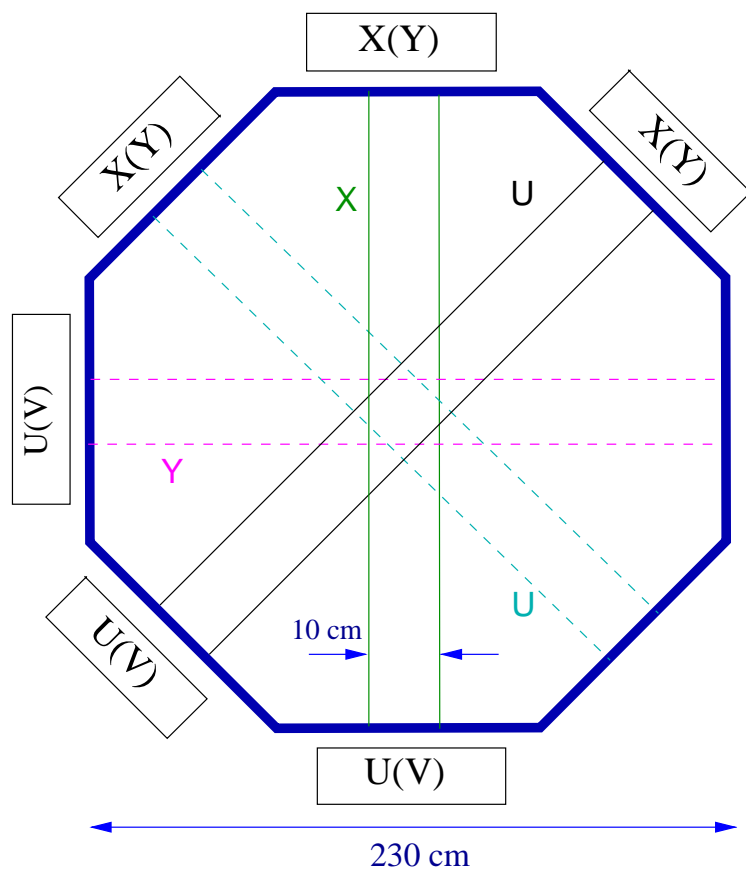


Figure 36: Two view chamber -  $(X,Y)$  and  $(U,V)$ , sketch.

view straw chamber with the regions in which only a limited numbers of views are available. A straw diameter of 9.6 mm is proposed for the main part of the chambers as a compromise

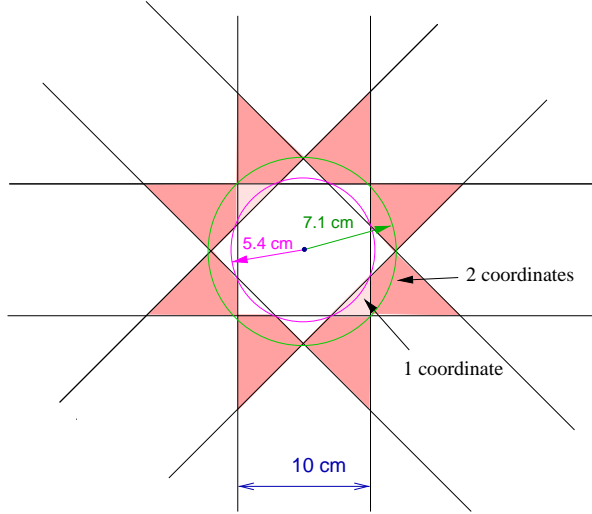


Figure 37: One and Two coordinate regions at use of (X,Y) and (U,V) chambers together.

between the rigidity (which depends on the diameter) and cost of production.

For the innermost straws approaching the beam, a straw diameter of 4.8 mm is proposed. Each straw is fabricated by winding two kapton films,  $12\ \mu\text{m}$  and  $25\ \mu\text{m}$  thick, to provide the necessary rigidity and gas-tightness (see Figure 38). The inner  $25\ \mu\text{m}$  kapton film is the thinnest carbon-loaded film available on the market. Each half layer contains 112 straws of 9.6 mm and 16 straws of 4.8 mm diameter, separated by 10 cm of empty space, as explained above. So, each chamber measures four coordinates and consists of 2048 channels. A sketch of a chamber is shown in Figure 36.

The Front-End Electronic (FEE) boards are placed near one edge of the straw, termination plates are placed near the opposite edge. The neighboring straws of each half of the layer are glued to one another. The amount of glue does not exceed 60% of the straw film weight. Gold plated tungsten wires  $30\mu\text{m}$  in diameter are used as anodes. Three polycarbonate spacers are implemented to support the wires of the longest straws and keep them in place. Each spacer weighs 25 mg. Two carbon wires will be used to fix the straw layer planarity excluding possible bending in Z- direction. The inner film ( $25\mu\text{m}$  thick) will be aluminized outside with a  $0.2\mu\text{m}$  thick layer. In total, the average thickness of the chamber is  $4 \times (80 - 90)\mu\text{m}$ . A gas leak test is foreseen for each straw before assembly, and each complete straw layer should be checked as well. A special vacuum system should keep good vacuum nearby the periphery of the chamber to avoid gas diffusion. To avoid space resolution drift, the chambers temperature

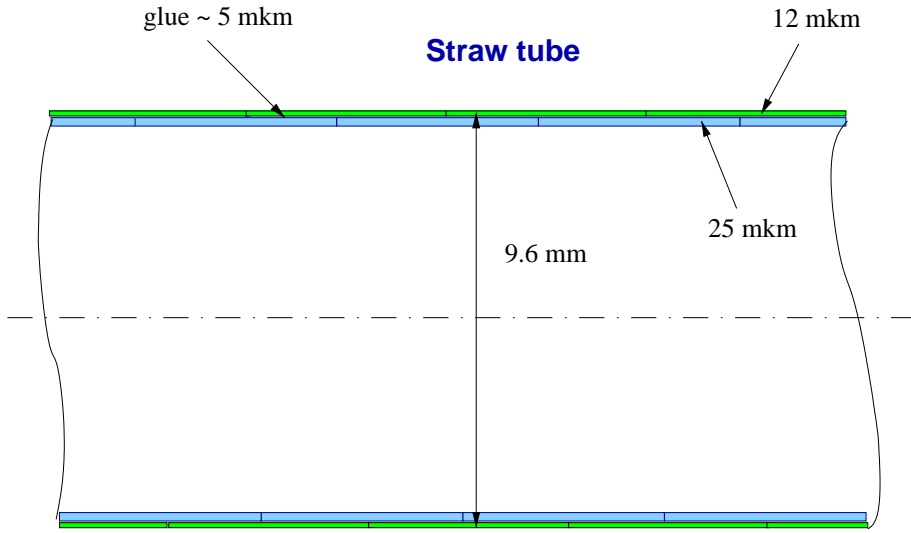


Figure 38: Straw tube schematic view.

should be kept in a range of  $\pm 1$  degree. Gas system and HV system should provide the necessary stability. The signals from the FEE will have a typical rise time of about 12 ns with a total width of about 100 ns, and special attention should be paid to the noise. The discriminator threshold should be less than 3 fC. The amount of material for each four-view chamber crossed by a track corresponds to 0.4 % of a radiation lengths ( $X_0$ ), including a typical gas mixture of Ar+CO<sub>2</sub> (80%+20%). The space resolution of a hit coordinate (view) reconstruction is expected to be  $\approx 130\mu\text{m}$ . To provide a redundant measurement of the pion momentum a double magnetic spectrometer is foreseen. For this purpose an additional MNP33 dipole magnet, similar to the one used in the NA48 experiments, is required. The magnet cost estimate amounts to about  $\approx 1170$  kCHF.

At least six tracker chambers are required for reliable reconstruction of the pion track kinematics, angle and momentum. Two chambers will be installed in each of three reagions: upstream of the first magnet, between the magnets, and downstream of the second magnet. Each of the chambers measures hit space position, based on known Z-coordinate (see Figure 39). A rough cost estimation for production of six chambers ( $\approx 11\,000$  channels in total) is around 630 kCHF. This cost does not include the expenses of motherboard and termination board productions with corresponding components (C, R, connectors), and the cost of the FEE, HV power supplies, gas and cooling systems, temperature monitoring and

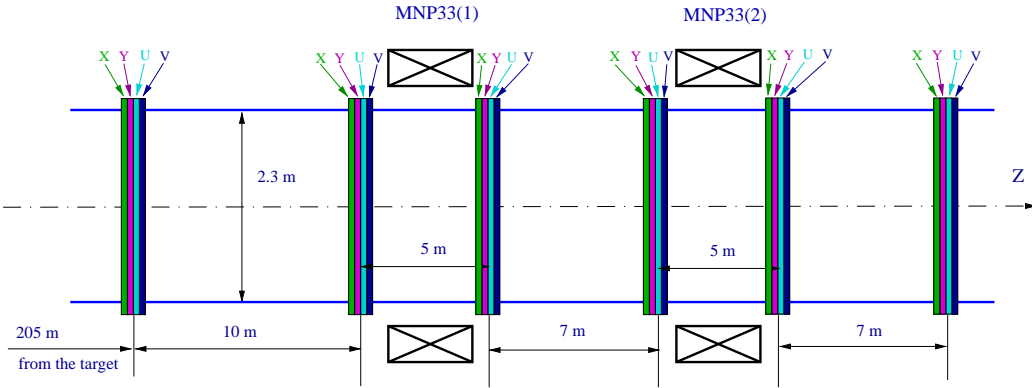


Figure 39: Schematic view of straw chamber positions in the spectrometer.

other auxiliaries. Major contributions to this cost and some estimates of additional expenses are presented in Table 11.

Item	Number	Unit cost, (CHF)	Price (kCHF)
Straws	11 000	20	220
Al frame and other element for double layer	24	15 000	360
Design, fabrication and test			250
Front end electronics	11 000	25	275
HV power supplies			250
Gas and cooling systems			250
<b>Total</b>			1605
read-out Electronics			750

Table 11: Cost estimate for the Straw Tracker.

## 10 RICH

The rejection of background originating from  $K^+ \rightarrow \mu^+ \nu$  ( $K_{\mu 2}$ ) requires the identification of the muon. This is mainly achieved by means of the MAgnetised MUon Detector described in Section 12 and by imposing that, under the hypothesis that the outgoing particle is a

pion, the squared missing mass is positive. However,  $K_{\mu 2}$  is the most frequent decay and the event mis-reconstruction can contaminate the signal region. In this proposal, the muon rejection of MAMUD is assumed to be  $10^5$ . Simulations show that it can be further improved only tightening the signal selection with significant loss of reconstruction efficiency. To keep good reconstruction efficiency we propose to use a fast RICH counter to further separate pions from muons up to momenta of 35 GeV/c. RICH spectrometers were proposed by CKM experiment at Fermilab [29] and by the re-designed version (KPLUS) [44] to provide a velocity measurement. The design of the KPLUS RICH is available [45] and we plan to adapt it to our layout. Under a particle mass hypothesis, the velocity measurement converts into a precise redundant measurement of the particle momentum. Conversely, if the momentum is measured by the magnetic spectrometer, the RICH can be used for particle identification. In our design we measure the momentum of the outgoing particle redundantly employing the double magnetic spectrometer, and the RICH will be used purely for particle identification. We estimated that a two sigma separation between pions and muons at the high end of the charged pion momentum spectrum will be sufficient to reduce the background originating from  $K_{\mu 2}$  and  $K^+ \rightarrow \mu^+ \nu \gamma$  to a negligible level.

## 11 CHARGED HODOSCOPE

The charged hodoscope, together with the vetoes, the LKr calorimeter and, possibly, the differential Cherenkov (CEDAR), is intended to build the event trigger and, therefore, it must possess a very good efficiency for detecting a MIP in its geometrical acceptance. A good MIP efficiency will also help in rejecting immediately high order multiplicity events, such as f.i.  $K^+ \rightarrow \pi^+ \pi^+ \pi^-$  decays. Moreover, the hodoscope signal will be used, off-line, to guarantee that the charged track is properly associated to the incoming particle, and for this reason the detector must also possess a very good intrinsic time resolution, better than 100 ps, given the high rate (about 1 GHz) of beam particles that will illuminate the Gigatracker. A recent technology which well matches both the above requirements is the one of the Multigap glass RPC [46] and we are planning to build the hodoscope using this technology, with a design very similar to the one used in the ALICE TOF, for which test beam results [47] show that time resolution up to 50 ps with rates up to 1 kHz/cm<sup>2</sup> [48], together with MIP efficiencies above 99.9% can be achieved. This rate is, however, about a factor of two smaller than what is expected in the hottest central region, near the beam pipe. For this reason, preliminary tests are needed to prove that the detector can really sustain up to 2

$\text{kHz}/\text{cm}^2$ , without any substantial worsening of its performance. The very schematic layout of the hodoscope we are considering is given in Figure 40.

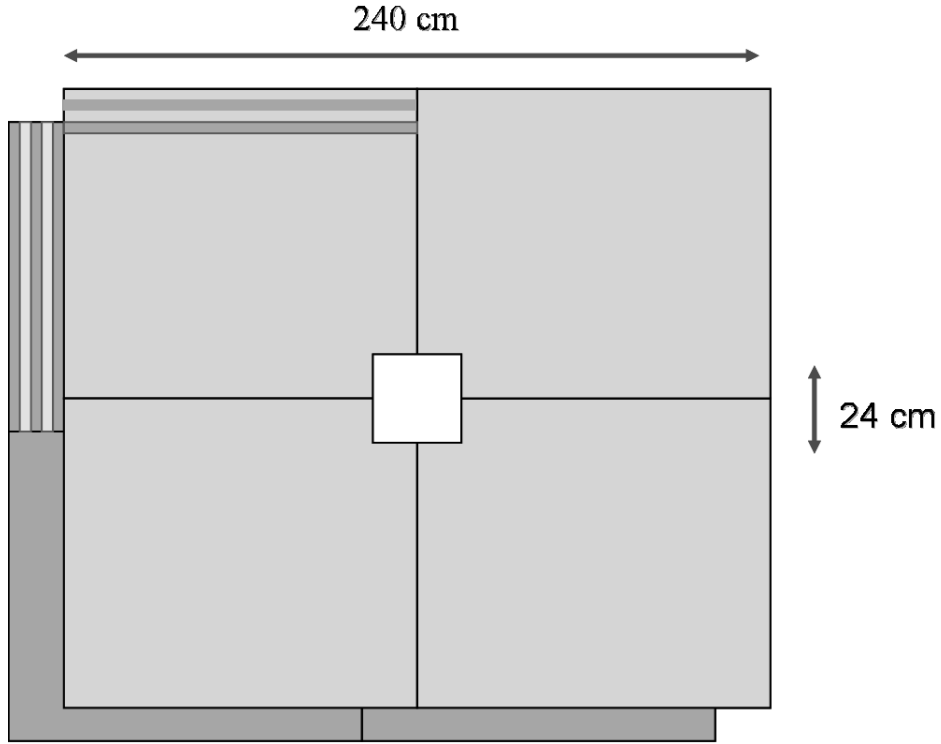


Figure 40: Hodoscope schematic view.

It consists of two planes  $2.4 \times 2.4 \text{ m}^2$  each, made by four independent modules, equipped with horizontal and vertical strips, respectively. The strips are 64 per module, 19 mm wide and 1200 mm long (apart from the central ones, only 1080 mm long, because of the central square hole), placed at 1 mm of distance from one another. The total number of strips to be read is, therefore, 480.

Each of the eight modules consists of 2 glass stacks of 5 gaps of  $250 \mu\text{m}$  each. The resistive plates are commercial "soda-lime" glass,  $400\mu\text{m}$  thick for the internal and  $550\mu\text{m}$  for the external plates. The external plates have a conductive coating ( $1 \text{ M}\Omega/\text{cm}^2$ ) deposited on one side and act as electrodes. The distance between the glass plates is kept fixed with the help of nylon fishing line used as a spacer and the necessary stiffness of the detector is ensured by two  $1 \text{ cm}$  thick aramid honeycomb panels, between which the glass stacks are sandwiched. All the detector is placed inside a tight gas box, where the gas mixture of 90%  $C_2F_4H_2$ , 5%

$SF_6$  and 5%  $C_4H_{10}$ , optimized [49] for efficiency, time-resolution and ageing, is circulated at atmospheric pressure. The estimated material budget of the detector (gas box excluded) is around 15% $X_0$ , which does not seem to be a problem. A differential high voltage of about  $\pm 6$  kV is applied between the external cathodes (in parallel) and the anode disposed is in the middle of the stack. The differential readout signal is obtained from anode and cathode pickup strips, deposited on a 1.5 mm thick standard PCB. Even if a single-strip readout might be sufficient for our purposes, we plan to test as soon as possible also a double-side readout, to verify the possibility of getting the track position along the strip with a resolution of the order of a cm [50], that could help at least as a redundancy in the global tracking and at the trigger level.

As far as the Front-End electronics is concerned, again we plan to use the one developed for the ALICE TOF, i.e. the *NINO* [51] ultrafast amplifier/discriminator 8-channel ASIC chip, especially designed to match the glass multigap RPC differential signal. The preamplifiers cards will be mounted outside from the gas box, on the outer border of the detector.

The Read-Out electronics foreseen is based on the High Performance TDC (HPTDC) [52] developed at CERN, with multi-hit and multi-event capabilities, which can work up to a time resolution of 24.4 ps and it has been especially optimised for this application [53]. Finally, we have evaluated the costs by rescaling those presented by the ALICE Collaboration (15 MCHF for about 150 m<sup>2</sup> of detector), keeping in mind, however, that our solution with read-out strips instead of pads (as in the ALICE TOF) means a reduction of about a factor 10 in the readout channels. In this way, we have estimated a total cost of the detector of about 900 kCHF, comprehensive of tooling, FE electronics, LV, HV, gas system, cables and connectors.

## 12 MAMUD

It is of prime importance for this experiment to veto the background from  $K_{\mu 2}$  decays and other decay modes containing muons. A very efficient muon veto is therefore required. It is proposed to build a highly segmented 5.25 metres long iron-scintillator sandwich which is situated behind the LKR calorimeter and also serves as hadron calorimeter. As a small angle veto calorimeter has to be installed at the very end of the beam line, the charged beam has to be deflected away from such veto counter. As space in this region is at a premium, we have opted for a magnetised muon veto and hadron calorimeter, called MAMUD (MAgnetised MUon and hadron Detector). The MAMUD detector can be considered

as a sampling calorimeter which should distinguish hadronic from electromagnetic showers, detect minimum ionizing particles and provide a bending power of 5Tm on the beam line. The longitudinal segmentation of the hadron calorimeter, together with its transverse granularity of 4 cm, is crucial to identify and reject "catastrophic" energy losses of muons from  $K^+$  decays. Catastrophic muon energy losses occur via muon Bremsstrahlung,  $e^+e^-$  pair production, high  $Q^2 \mu^+e^-$  scattering and muon decay in flight, all leading to electromagnetic showers which can easily be distinguished from hadronic showers. The ultimate limit of muon rejection power is given by muon deep inelastic scattering events where the residual energy of the muon is too small to be detected.

The proposed detector consists of 150 iron plates, 2 cm thick and of  $2.8 \times 2.6 \text{ m}^2$  transverse size, interspersed with scintillator planes of 130 strips, each 1.3 metres long. This structure is divided into 8 independent sections of 18 or 19 planes each. One section corresponds approximately to  $20 X_0$  and 2 interaction lengths, reasonably matching the LKR calorimeter thickness. At the centre a 30 by 20 cm rectangular hole allows the beam to pass cleanly through the detector.

The active detectors consist of extruded polystyrene scintillator strips, 140 and 130 cm long, 1 cm thick and 4 cm wide, read out at one end by a 1.2 mm diameter wave length shifting fiber as shown in Figure 41.

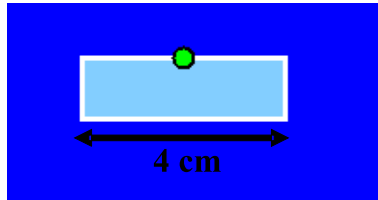


Figure 41: Cross section of one MAMUD strip of extruded scintillator with WLS.

Strips in adjacent gaps are orthogonal. Based on the MINOS experience, we expect to obtain on average 4.5 photoelectrons per strip for a minimum ionizing particle at the cathode of a photomultiplier tube optically connected to the wavelength shifting fiber glued to this strip. The strips are read by combining the signals from nine consecutive horizontal (or vertical) strips into a single 1 cm diameter photomultiplier. In the minimal configuration only half of the planes are instrumented, namely the first 55 and the last 18 planes, corresponding to 4 sections in total. In the optimal configuration, which we propose, all planes are equipped and 2080 PMT's are required for a total scintillator area of about  $1000 \text{ m}^2$ . Both tracking and calorimetric information is obtained. The magnetic field, about 1.0 T on the axis, is

provided by a system of two coils, shown in Figure 42. Each coil is divided into 4 layers of

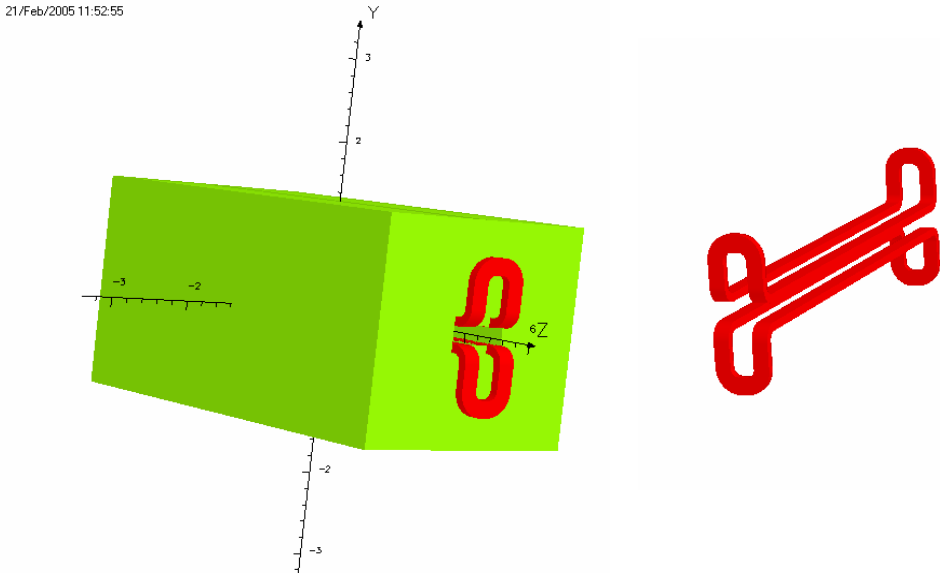


Figure 42: Sketch of the hadron calorimeter (MAMUD). The iron lamination is not shown.

8 turns each. The conductor material is certified grade Cu-OFE of section  $25 \times 25$  mm with a 12 mm diameter hole for cooling. The current is 2.7 KA, the total power dissipation is 0.3 MW. The pressure drop is about 10 bars. The magnet parameters are summarized in Table 12

The transverse field homogeneity is shown in Figure 43. The uniformity over a 10 by 10 cm<sup>2</sup> region at the centre is 3.5% and increases to about 5% at the ends of the magnet, which is adequate for our needs. The MAMUD performance has been studied by detailed GEANT simulation, taking into account the upstream detectors, i.e. straw tubes, LKR calorimeter and RICH. For  $\mu$  separation the combined information from MAMUD and the LKR has been used. The LKR information is important because its length is 2 interaction lengths and hence some 80% of pions start showering there. The  $\pi/\mu$  separation is based on a number of variables that can easily be implemented in the hardware trigger: total energy deposited and the numbers of strips hit in the different sections of MAMUD, as well as the maximum energy deposition and its position in LKR and MAMUD. This study has been

Total weight	$\approx 150$ ton
Overall Dimension	$2.8 \text{ m} \times 2.6 \text{ m} \times 5.25 \text{ m}$ (W×H×L)
Number of iron plates	150
Coil Current	$\approx 2.7 \text{ KA}$
Total power dissipation	$\approx 0.3 \text{ MW}$
Field integral on axis (from -1 to +6.2 m)	5 Tm
Magnetic Field into a "good field region" (10 cm × 10 cm)	$\approx 1 \text{ T}$

Table 12: Magnet parameters of MAMUD.

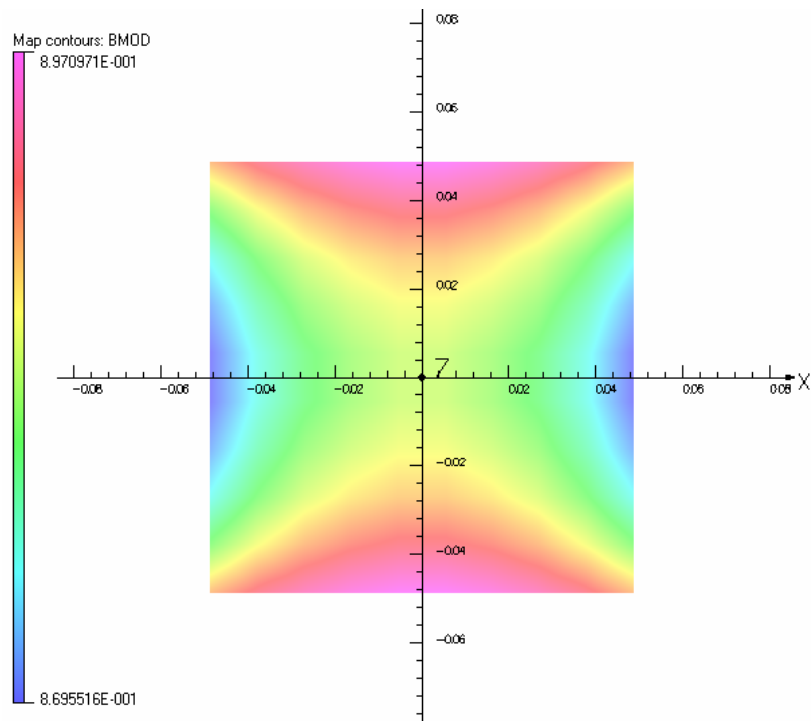


Figure 43: MAMUD transverse field homogeneity.

done for the minimal MAMUD configuration. In total 106 signal events and  $3 \cdot 10^7$   $K$  decays were generated. An example of signal background separation is shown in Figure 44, where ratio of the sum of maximal energy depositions in the MAMUD strips per section and the total energy deposited in MAMUD is shown. A muon suppression by a factor of  $1.1 \cdot 10^{-6}$  can be achieved for a pion efficiency of 47%, in case the information from the RICH is not included. Assuming additional - discrimination from the RICH, the selection criteria can be relaxed to ensure a much higher pion efficiency.

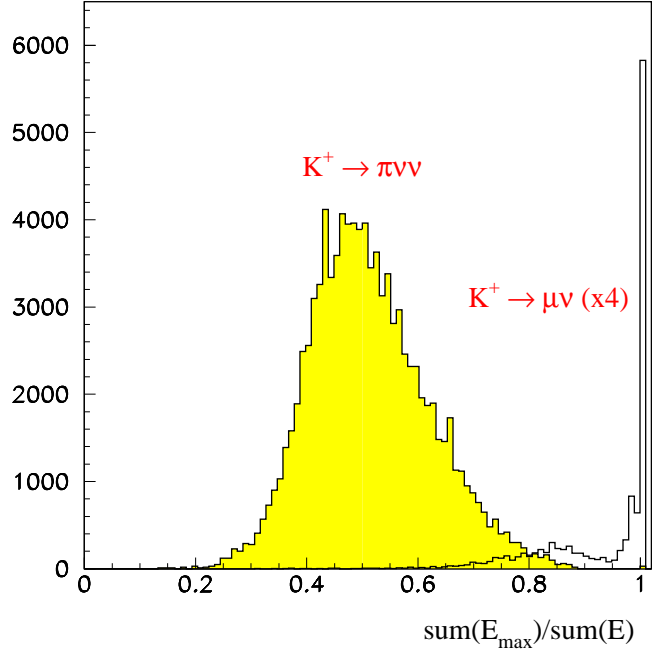


Figure 44: The distribution of the ratio of the sum of the maximum energy deposited in all MAMUD sections and the total energy deposited in MAMUD, separately for signal and  $K \rightarrow \mu^+\nu$  background events.

The cost of the MAMUD device is estimated in Table 13. We note that the design and construction of the magnetic parts of MAMUD will take three years from the moment that funding is approved.

Item	Cost (kCHF)	Comments
Iron material	450	Jebens estimate
Copper conductor	60	
Coil assembly	300	SigmaPhi
Auxilliary systems, controls	50	
Power Supplies (mods.)	20	
Contingency	40	
Manpower	4.5 FTE	
Scintillator + photomultipliers + fibers	300	
Readout electronics	300	
Total	1520 + manpower	

Table 13: Cost estimate for the MAMUD detector.

## 13 Trigger and DAQ

The existing NA48 trigger electronics was designed more than 10 years ago using (then) new technology; the design was tailored to the specific needs of the direct CP violation measurement: in particular the part dealing with calorimetric information featured innovative and successful dead-time-free pipelining techniques, but overall the system provided trigger algorithms rather focused toward the detection of two pion final states.

Such electronics can no longer be used for a new experiment, either because it is not suited to the new sub-detectors or, for those parts of the NA48 setup which will be kept, for reasons of insufficient performance with the higher beam flux and foremost lack of support.

Moreover, for a large part of the electronics, notably the calorimetric trigger system, the design is strictly coupled to the front-end or digitizing hardware, which will also have to be rebuilt for the same reasons. It seems therefore that most of the existing trigger/DAQ system will have to be rebuilt, with the possible exceptions of the KABES and Drift Chamber readout systems, which were the latest additions to NA48.

The intensity of the  $K^+$  beam for the new experiment will be roughly 30 times higher than the one due to the sum of the two charged beams used in NA48/2. The single-track rate for the NA48/2 experiment was in the MHz range, to be compared with a final trigger (and read-out) rate of order 10 kHz, as limited by the design of hardware components. For the new experiment a rate of about 11 MHz kaon decays is expected, to which a muon halo rate should be added (less than about 7 MHz), and the global reduction factor by the trigger

should be at least a factor 10 higher than in NA48.

The above considerations clear the way to considering the design of an appropriate trigger system without compromises driven by needs of re-using existing electronics. On the other hand, given the time scale for the experiment, it is clear that adopting solutions already developed for other experiments - wherever feasible - is a must. For the design of the new experiment's trigger system one should adopt a rather far-looking approach to allow also:

- adapting to the emerging requirements as the experiment design finalizes;
- future upgrades of the read-out bandwidth to allow adjusting to possible higher intensities;
- a reconfiguration to adapt the system to further kaon physics programs.

The purpose of the trigger system is to reduce the rate to a manageable level, rejecting as much as possible all main decay modes of the  $K^+$  and beam backgrounds while affecting in a minimal way the  $K^+ \rightarrow \pi^+ \nu\bar{\nu}$  signal.

In view of the difficult task of the offline analysis, which will have to exploit strong and redundant cuts to suppress backgrounds, special care has to be taken in using trigger cuts which are as simple as possible, so that they can be shadowed by tighter offline cuts allowing accurate efficiency estimation without concerns due to the imperfect knowledge of resolution effects at the hardware trigger level. Moreover, the trigger cuts should ideally not introduce any correlation between different sub-detectors, so that sets of cuts can be developed offline which are known to be effectively independent.

A satisfactory compromise has to be found between the simplicity of the trigger and the need to effectively cut down the very high rate.

In this respect, the best approach seems to be one in which the trigger cuts are performed as much as possible in software, using a system of commercial processors connected with high speed data links which process the actual sub-detector event data. This scheme, which is being adopted by most modern particle physics experiments, presents several advantages over the traditional approach of a hardware trigger tailored to the specific reaction under study.

Two of the main advantages of a software-based approach are flexibility - since the optimization of the trigger algorithms can be decoupled from their implementation in the trigger infrastructure - and scalability - since by replacing commodity processors and links with new, more powerful, ones appearing on the market, the system capability in terms of data throughput and trigger versatility can be increased without any major redesign, therefore allowing a longer lifespan for the system.

These two points are particularly important for a rare decay experiment, in which the op-

timization of the trigger can be a lengthy and delicate issue, making a big difference in the quality of the final result, and in which the capability of the sub-detectors to stand high particle rates should be well complemented by the capability of the trigger system of allowing the highest bandwidth. The fact that the events of interest are very rare does not mean, unfortunately, that a small set of data has to be collected, since very selective cuts cannot be performed safely except when the full information from the detector (in terms of granularity and calibration) is exploited, which means in the offline analysis.

The cost is also an important factor, since the need for development (and maintenance) of experiment-specific electronics is kept to a minimum. The control software of the system is in this case also more user-friendly and easily maintained than for a specific custom hardware system.

When the above concept is brought to its extremes one has the scheme of a completely "triggerless" readout, in which the sub-detectors are read-out continuously, following some strobe signal which could even be a simple periodic clock. The appeal of such a scheme lies not only in the fact that the above issues of flexibility and scalability are maximized, but also in that it allows having a single path for event data also serving for trigger purposes, in contrast to the traditional approach in which a separate and parallel "trigger branch" is required.

In the case of a high-flux fixed target experiment with a debunched beam, there is no intrinsic time strobe signal to indicate the possible occurrence of an interesting event, and continuous digitization at the frequency of an experiment clock suited to detector sampling leads to rates which are way beyond the capabilities of reasonable data acquisition systems. This means that a low level hardware trigger will be anyway required, but one would like this Level 0 trigger to be as simple as possible, and just sufficient to reduce the rate to a level which allows complete readout of the sub-detector data into PCs, where further trigger processing (possibly multi-level) is performed.

We plan to use a multi-level trigger system in which only the first level (L0) is implemented in hardware, and consists in rather simple conditions, mostly simple tight coincidences of detectors with excellent online time resolutions, some of them providing minimal hit-pattern information. The complete sub-detector data would be read-out at this L0 trigger rate, possibly after standalone zero suppression, online calibration and data compaction, to buffer memories, most likely internal PC memory banks, through high-speed point to point data-links. The following trigger stages would be performed in software by a farm of processors interconnected through a high performance switching network, reconstructing and analyzing

either data from a single sub-detector (L1) or the complete event data after event building (L2). Each of these trigger levels might be itself implemented as multi-level software processes to optimize the performance. Figure 45 shows a simplified block diagram of the proposed scheme.

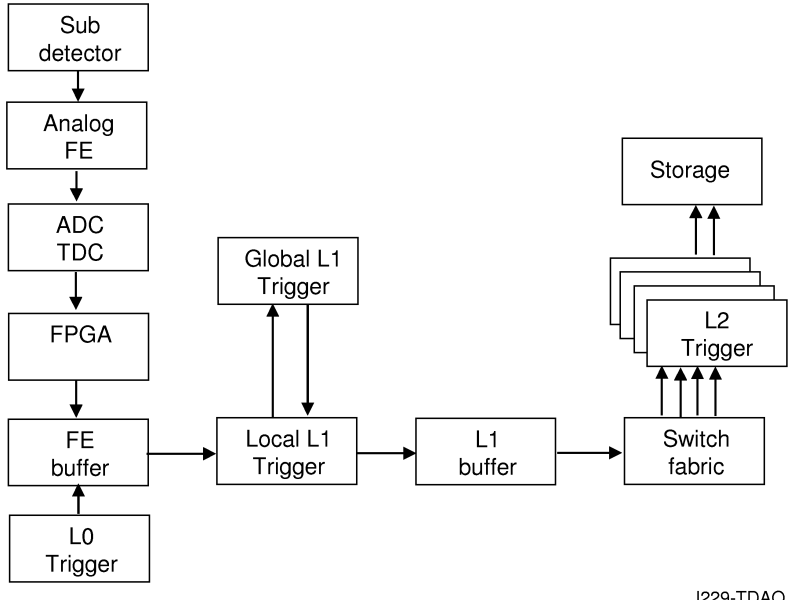


Figure 45: Simplified sketch of the trigger/DAQ electronics.

Both L1 and L2 might be performed in the same processor array or in different ones, depending on how the topology of the switching network is optimized for throughput; this is a subject of further study. One could envisage *e.g.* to have a first layer of CPUs receiving the data from sub-detectors (or parts of them) via dedicated high-speed links, and performing further “local” computations on event fragments to provide informations for a central L1 trigger decision unit, before event building, while the following part of CPU farm is used for L2 trigger based on algorithms working on complete events.

Events sitting in PC memories and surviving all trigger stages will be logged to disks and sent through links to the Computing Centre for subsequent archiving in Central Data Recording, as done for NA48. Further processing for either data reduction or monitoring might take place there, if required, before tape logging, again as was done in NA48.

For this experiment, the rate in the detector will be due to  $K^+$  decays and muons from the

beam halo, integrated over the surface of the detector.

All kaons decaying between the final collimator and the detector contribute to such rate, even if only the upstream region will be used as fiducial region for the signal. The beam intensity figures in Table 6 correspond to about 11 MHz kaon decays occurring upstream of the charged hodoscope. Such decays occur without any significant time structure due to slow-extracted nature of the SPS beam; this implies that there is no minimum time interval between decays, and also that there is no intrinsic time reference signal to indicate the possible presence of an interesting event occurring at any time (in contrast to collider experiments or experiments with bunched or micro-bunched beams). The rate indicated above assumes an effective spill length of 3s for a 4.8s flat top, as suggested by the NA48/2 experience.

The total number of channels for the experiment can be roughly estimated as 100.000 (pixels) + 13.500 (Liquid Krypton calorimeter - LKR) + 15.000 (straws) + a few thousands for the rest = about 150.000 in total. The occupancy is very low for the interesting events; for most of the channels the information is time-like and therefore reduced by the front-end TDCs. The working approach is to reduce the rate to below 1 MHz in L0 (*i.e.* something more than one order of magnitude) and read sub-detectors at this rate. Incidentally, this is the first level trigger rate for the LHC-b experiment, at which data are transferred to PCs for software triggering.

The most crucial figure is the average data bandwidth requirement for read-out, which determines the number of front-end PCs, those directly connected to the front-end, depending on the link capacity used. At a given trigger rate this depends on the event data size, which is another delicate issue for this particular experiment. The quality of the experimental result of the experiment will depend on how well one will be able to suppress backgrounds at a very high level; in final offline analysis this task would profit by the use of all sub-detector information available, meaning that for the small final event sample one would like to have the complete detailed detector information. Although some details are not yet finalized, it is clear that several sub-detectors will only provide time (TDC) information, therefore with a self-defined autonomous data rate which is bounded by the sub-detector hit rate, and is further reduced by reading them only at the (lower) trigger rate. For sub-detectors in which both time and pulse-height information is extracted through continuous signal sampling ("Flash" ADC), there is no hit self-detection, the triggerless data rate is prohibitive and also the triggered one can be very large depending on the number of channels being read.

For the present electromagnetic liquid Krypton calorimeter, with 13500 channels sampled at 40 MHz, assuming a new digitization scheme in which the sample information is compressed

to 8 bits (therefore forfeiting part of the excellent intrinsic energy resolution, since the NA48 scheme adopted a non-linear 10 bit encoding - corresponding to about 14 effective bits), at the same 40 MHz sampling frequency results in a 540 GB/s raw data rate and about 100 GB/s for a 1 MHz trigger rate assuming 8 samples are readout as in the most recent NA48 data taking periods.

Such data rate could be easily reduced by a large factor by applying zero suppression, but one would like to consider the possibility of not doing this and keeping the whole sub-detector information, at least until the data has been transferred to processor memories. The first reason for evaluating this is that zero suppression is inherently a difficult task, in that to avoid compromising the excellent energy resolution it has to be performed by a system which has an overall view of the whole sub-detector at some level, which is easy in software but requires some degree of interconnectivity among front-end read-out boards when performed there. Secondly, for this specific experiment the electro-magnetic calorimeter is mostly (but not exclusively) used as a veto, and one would like to avoid any chance of suppressing possibly significant information from it at an early stage. Still, even if hardware zero suppression is not performed before read-out, lossless data compression implemented in hardware would most likely reduce the above data rate by a significant factor, which has to be evaluated with realistic conditions and algorithms.

With respect to the above data rate from the electromagnetic calorimeter, the other sub-detectors are expected to be less demanding, either because of the limited number of channels, or because of the intrinsic data sparsification. As an example, a silicon pixel station with 43200 channels, despite the huge particle flux (1 GHit/s), considering a read-out window of 50 ns (rather large with respect to the expected sub-nanosecond time resolution) and 8 bytes for time and channel information, can be estimated to deliver about  $1 \text{ GHz} \times 50 \text{ ns} \times 1 \text{ MHz} \times 8 \text{ bytes} \simeq 400 \text{ MB/s}$ , for a 1 MHz trigger rate. Data rates from other sub-detectors are estimated to be significantly lower than this.

The size of the non zero-suppressed electromagnetic calorimeter data block would be about 110 kB per event, and an upper bound for the event data size could be estimated as 150 kB.

The total data volume written to permanent storage for a single burst depends on the data logging rate capability. In this respect it is important to note that, quite differently from collider experiments, this experiment will have a duty cycle of about 30%, dictated by the machine extraction, and this leaves a larger amount of time for data streaming. Lately, NA48 used to log to tape about  $5 \times 10^4$  events per spill, corresponding to an average 370

MB/spill, written to tape in the Computing Centre over the full 16.8 spill period. This data rate was obviously limited by the experiment read-out bandwidth and not by the data logging capability.

For the unrealistically conservative event size of 150 kB (15 times that in NA48), even a 100 kHz trigger rate (*i.e.* an unrealistically low trigger rate reduction of just a factor 10 on top of L1) would correspond to 15 GB of data for the entire spill. This shows that buffer memory requirements are not a big issue. On the other hand, a data logging rate as that for LHC experiments, around 100 MB/s (it was  $\sim$  30 MB/s for NA48) would correspond to a final event rate in the kHz range for the above large event size. From this point of view, the product of event size and trigger rate reduction in software triggers with respect to a L0 input rate of 1 MHz should therefore be bounded by

$$\frac{150 \text{ kB}}{\text{Event size}} \frac{1 \text{ MHz}}{\text{Readout rate}} \gtrsim 400$$

meaning *e.g.* a software trigger reduction by a factor 40 for a 15 kB event size.

The requirements in terms of computing power depend strongly on the hierarchical way in which the algorithms are implemented. Sophisticated high-level trigger algorithms for LHC experiments working on complete reconstructed events are benchmarked to perform in (few) ms on modern CPUs. Our events will be significantly smaller and simpler, with a vastly inferior detector occupancy. An educated guess of  $\sim$  1 ms overall computing time per event (weighted average of first and subsequent software trigger levels, involving algorithms with very different level of complexity and the use of different parts of the even data) would require  $\sim$  300 of today CPUs, and this figure would be expected to become significantly lower at the time the experiment starts. Of course the above numbers will have to be put on solid grounds by real measurements, which is however not a quick task even for existing sub-detectors, since the existing NA48 reconstruction software is definitely not optimized for online applications.

The L0 trigger will of course require a signal in the charged hodoscope corresponding to at least one track crossing it. Such signal will have very good online timing properties, allowing tight coincidences with veto systems. If such device has bi-dimensional readout capability, it could rather easily provide hit multiplicity with simple hardware look-up tables; some rougher multiplicity signal could also be available in case of mono-dimensional readout, but clearly the bi-dimensional solution (*i.e.* readout pads) is a superior choice, which could be useful at the trigger level, where track multiplicity signals from other sub-detectors (*e.g.* straws) might not be available. If real multiplicity information is available from the hodoscope,

events which are inconsistent with having more than a single track in a tight time window can be vetoed, therefore helping in reducing the rate from  $\pi^+\pi^+\pi^-$  decays.

A large fraction of  $K^+$  decays contain a muon in the final state, and so the use of a muon veto in the L0 trigger will be essential; this of course requires an appropriate online time resolution to limit the random vetoing, and will get rid of the muon halo as well. If the online time resolution of the MAMUD sub-detector is not enough to allow a tight veto coincidence window with good rejection power (efficiency), then a faster sub-detector plane might be inserted in the downstream of MAMUD for trigger vetoing purposes.

Besides  $\mu^+\nu$ , the next large decay mode contributing to the rate is  $\pi^+\pi^0$ , which can be reduced somewhat by using the large-angle photon vetos (ANTI), but in a more substantial way by exploiting the electromagnetic calorimeter. Cluster counting at the trigger level would be useful in this context, but since a signal event has at most one cluster in the electromagnetic calorimeter, simpler conditions not requiring a complex (hardware) trigger processor could be used at L0. In NA48 a dedicated pipelined trigger system was used which continuously computed the first three energy moments and performed cluster counting working on mono-dimensional projections with a 4 cm (2 cells width) granularity. While a new hardware system with those capabilities (or more) would allow a stronger rate reduction at L0, for the present purpose it seems that a fast computation of quantities which do not require clustering algorithms could be enough. Examples are the total energy deposit over the full detector as well as over quadrants; these quantities could be continuously computed online in the FPGAs which will follow the digitization stage to handle tasks such as online calibration, pedestal subtraction and data compression. A pipelined summation tree is all that is required, and one can envisage that energy sums can be available with a very short latency, well below a  $\mu\text{s}$ .

The use of small angle photon vetos and charged veto counters should also be foreseen, to help reducing further the rate from multi-body final states.

If the muon veto system has an adequate online time resolution to be used effectively in the trigger with a tight timing, most of the trigger rate will be dominated by kaon decays, and the inclusion of the CEDAR in the trigger will not be required, avoiding some difficulties due to the location of this sub-detector being far upstream with respect to the rest of the detector. On the other hand it should be kept in mind that for a 10 MHz muon hit rate a coincidence window of 5ns already corresponds to 5% dead time due to random vetoing, and at this time one should not exclude that the kaon tagging signal from the CEDAR is used in the L0 trigger to help rejecting the halo muons.

A central hardware L0 unit should take care of synchronizing the various sub-detector signals participating to L0, and the pattern (and its time history) of such signals should be recorded and made available into the event data. The time latency of the L0 trigger should be of a few  $\mu\text{s}$ , mostly dominated by the distance between participating sub-detectors and its delivery time to far devices (*e.g.* the gigatracker). For a rare decay experiment such as this one it should be clear that a significant fraction of the trigger bandwidth should be reserved to collecting down-scaled control triggers, with far less stringent conditions, which will be required for the offline study of correlations among different cuts. Such trigger down-scaling should be done both in the central hardware L0 system and (with ease) in the following higher-level software triggers. Calibration triggers should also be collected of course, and a peculiarity of this experiment lies in the need for special monitoring triggers, which should be recorded continuously in order to allow an accurate offline check of the live-state of the sub-detectors and their read-out chain: this is a crucial issue for this measurement, since a very small undetected inefficiency in just part of the system (such as a part of the veto system) could jeopardize the result. Finally, ancillary (down-scaled) triggers will also be implemented in order to collect significant samples of less rare  $K^+$  decay modes for other physics measurements: this point requires further study, but at first sight it seems that allowing a fraction of higher track-multiplicity events, corresponding to decay modes with 3 charged tracks in the acceptance, would be the most interesting possibility, with less interference with the signal trigger. MonteCarlo simulations have been performed to

estimate the rate reduction which can be expected for L0 by using simple cuts using minimal correlation among detectors. Event rates have been evaluated normalizing to a 11 MHz kaon decay rate, including all major decay modes, in the region between the last collimator (the acceptance drops rapidly to zero for decays upstream the final collimator, even when just single-track event fragments are considered) and the hodoscope.

Table 14 shows the relative data reduction which can be obtained with some of the cuts which might be performed in a rather simple hardware L0 trigger system. This is shown graphically in Figure 46.

In the above table, the “ $< 2$  EM quadrants” cut is performed in a somewhat safe way: since the hadronic shower produced by the  $\pi^+$  in the signal can extend to large distances over the calorimeter, a simple quadrant cut would be rather inefficient in some regions; the simulated cut rather checks the quadrants which are hit when the calorimeter is subdivided along two orthogonal lines either top-bottom and left-right, or along the bisectors of the former, and the condition requires that at least in one of such sub-divisions there are less

K decay rate	1.0	
>1 hodoscope hit	0.73	62% $K_{\mu 2}$ , 22% $K_{\pi 2}$
Muon veto	0.24	62% $K_{\pi 2}$ , 22% $K_{\pi 3}$ , 13% $K_{e 3}$
Large angle photon vetos	0.18	60% $K_{\pi 2}$ , 26% $K_{\pi 3}$ , 12% $K_{e 3}$
Hodoscope multiplicity < 2	0.15	-70% of $K_{\pi 3}$
EM energy < 50 GeV	0.09	-65% of $K_{\pi 2}$
No EM opposite quadrants	0.04	-86% of $K_{\pi 2}$
No EM opposite quadrants and E < 50 GeV	0.04	-87% of $K_{\pi 2}$
< 2 EM quadrants	0.03	-92% of $K_{\pi 2}$
< 2 EM quadrants and E < 50 GeV	0.03	-92% of $K_{\pi 2}$
< 2 EM clusters	0.02	-94% of $K_{\pi 2}$

Table 14: Expected rate reduction with some L0 cuts. All cuts in the upper part of the table are applied in cascade, while the lower part of the table shows the rate reduction (with respect to the total K decay rate) with only a single cut applied on top of all those in the upper part. Muon halo from upstream decays is not included.

than 2 quadrants being hit. The EM energy cut at 50 GeV is of course compatible with the cut on  $\pi^+$  momentum which is foreseen to suppress background.

From the above table it appears that a 11 MHz kaon decay rate could be reduced to well below 1 MHz without actual cluster counting in the EM calorimeter, therefore allowing to consider a rather simpler L1 hardware processor; real (bi-dimensional) cluster counting would further cut the rate by less than a factor 2 with respect to the above simple-minded cuts, and moreover the cuts considered above are examples of “local” computations which do not require exchange of information among different parts of the sub-detector, but rather just combining information computed on sub-sections of it.

The upper multiplicity cut on hodoscope hits is seen to be a rather marginal addition in terms of rate reduction.

Finally, the simulation also shows that without including the photon veto counters in the trigger the rate increases by only  $\sim 30\%$  (*e.g.* from a rate reduction factor 0.027 to 0.034 in the case of quadrants and total energy cut).

Of course all the above assumes 100% veto efficiency (which even for fast sub-detectors means neglecting time tails in their response). The effect of a reduced online veto efficiency on some of the rates discussed above is shown in Tables 13 and 13.

	Muon veto efficiency		
	0.99	0.95	0.90
Muon veto	0.24 (+2%)	0.26 (+10%)	0.29 (+20%)
EM energy < 50 GeV	0.09 (+6%)	0.11 (+27%)	0.13 (+55%)
No EM opposite quadrants	0.05 (+12%)	0.07 (+57%)	0.09 (+115%)
< 2 EM quadrants and E < 50 GeV	0.03 (+20%)	0.05 (+86%)	0.07 (+168%)

Table 15: Rate reduction with some L0 cuts as a function of the muon veto efficiency. The numbers in parenthesis indicate the increase with respect to the 100% efficiency case in Table 14. The muon halo from upstream decays is not included.

	Large angle photon veto efficiency			
	0.99	0.95	0.90	0.50
Large angle photon vetoes	0.18 (+0%)	0.18 (+2%)	0.18 (+3%)	0.21 (+15%)
EM energy < 50 GeV	0.09 (+1%)	0.09 (+1%)	0.09 (+3%)	0.10 (+12%)
No EM opposite quadrants	0.04 (+1%)	0.04 (+2%)	0.04 (+4%)	0.05 (+25%)
< 2 EM quadrants and E < 50 GeV	0.03 (+0%)	0.03 (+1%)	0.03 (+1%)	0.03 (+11%)

Table 16: Rate reduction with some L0 cuts as a function of the large angle photon vetoes efficiency. The numbers in parenthesis indicate the increase with respect to the 100% efficiency case in Table 14. The muon halo from upstream decays is not included.

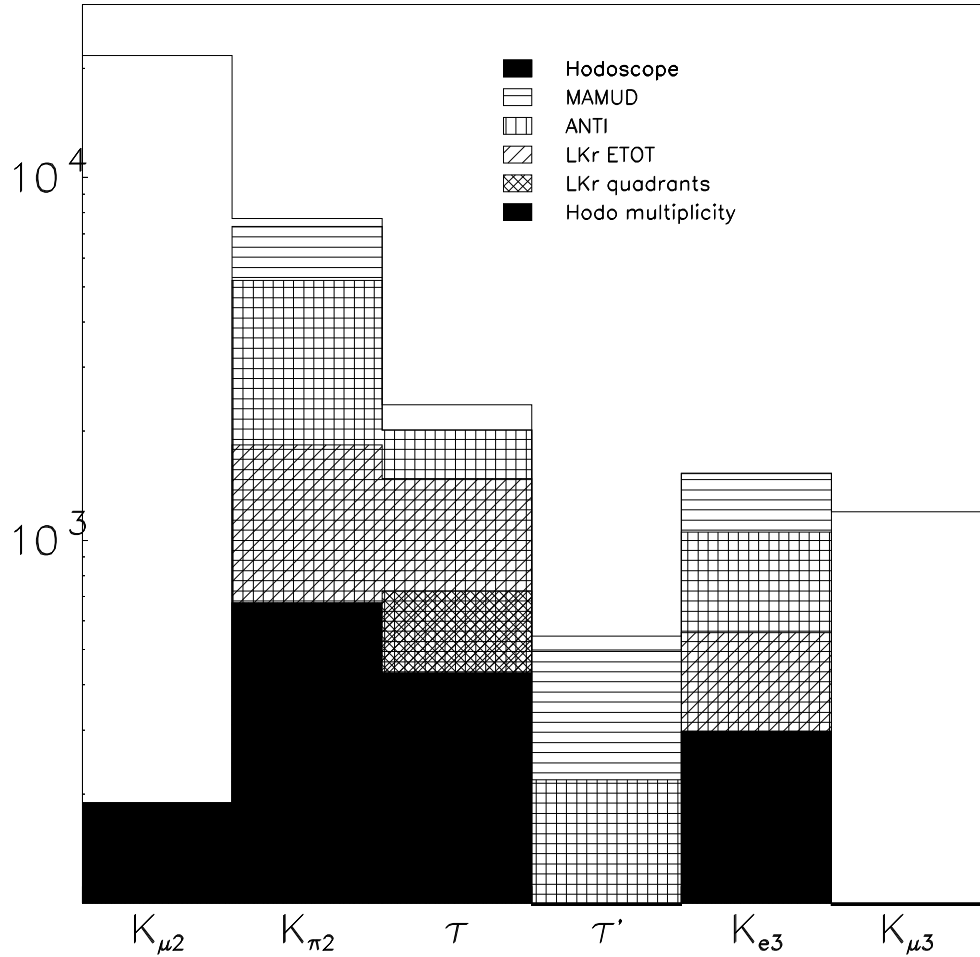


Figure 46: Cumulative reduction of different decay modes with some L0 cuts. The “LKR quadrant” cut is the “ $< 2$  EM quadrants” in Table 14.

The above tables put in evidence the fact that the online muon veto inefficiency can affect the total rate by a significant factor, while the large angle photon veto inefficiency has much less impact. Moreover, the contribution to the muon halo (estimated to be 7 MHz) from upstream decays is not accounted for in the above table, while in case of muon veto inefficiency it could contribute significantly to the rate.

The above discussion by no means exhausts the L0 trigger study, but is just meant to show that the above assumptions of a L0 trigger rate below 1 MHz seems reasonably within reach without requiring a complex hardware trigger system. Further study is required to actually

identify the best set of trigger primitives which are required to be computed online from the L0 electromagnetic calorimeter system.

Issues concerning the algorithms to be used in higher level software triggers are not discussed here, as they require deeper study, also due to their connection with the offline analysis strategy. Nevertheless, it is clear that by being able to cross-correlate sub-detector information, with the full power of software algorithms, much stronger data reduction factors can be achieved in a rather easy way.

The trigger/data acquisition scheme roughly outlined above does not seem unrealistic, and with the current understanding it appears that the most important issue for its implementation would actually be the data transfer bandwidth available from the front-end to the PCs. While it is too early to discuss realistic implementation issues at this stage, it is worth mentioning in this respect that the LHC-b experiment plans to transfer data to a trigger processing PC farm at 1 MHz rate using Gigabit Ethernet links. While network switching equipment allowing data throughputs in excess of 100GB/s are already available on the market, 10-Gigabit Ethernet is also starting to emerge on the market, and might be affordable by the time the system has to be built.

We are starting to evaluate the possibility of using hardware and solutions developed for the LHC experiments, while keeping the possibility of exploiting technology improvements which would not require architecture changes but the simple replacement of some elements with more performing ones appearing on the market.

Another important issue, concerning the wish to keep the development of specific electronics to a minimum, is the effort which we plan to make toward adopting common electronics for different sub-detectors as much as possible, even in the area between the analog front-end proper and the injection in the data acquisition system. It seems that, apart from special cases obviously requiring *ad hoc* solutions (as is the case of the silicon pixels), several other sub-detectors could profit from the use of some flexible common digitization and hardware processing board, maybe even exploiting in part systems developed for LHC experiments.

### 13.1 Detector Control System

The existing NA48 Detector Control System (DCS) was developed by CERN about 10 years ago and is now obsolete. It has to be upgraded applying new technology supported at CERN and recommended by IT/CO, using Windows and Linux PCs as hardware. The supervision

of the new system can be built using PVSS SCADA product and developed by IT/CO JCOP framework. The Front End layer should be based on commercial OPC servers as much as possible. We are presently considering the ELMBs designed by the ATLAS Collaboration as the most cost effective solution for analog measurements. Most of the NA48 existing sensors and cables can be reused for the new experiment, thereby reducing considerably the cost of the upgrade.

## 14 Resources and Schedule

The human, technical and financial resources needed to perform the experiment have been evaluated. In Table 17 we report the estimation of the cost of the detectors and associated electronics. For some items such as the RICH counter they are intended to be an indication. Sharing among the collaborationg Institutions will be defined in the Memorandum of Understanding. Human and technical resources are as important as the financial ones. We

Element	Cost (MCHF)	Comments
BEAM LINE	0.4	Modified K12 line
CEDAR	0.5	
GIGATRACKER	2.7	1.4 MCHF if 0.25 $\mu\text{m}$ CMOS technology can be used
VACUUM	1.0	Addition of 20 large diffusion pumps
ANTI	4.2	
STRAW TRACKER	2.4	
MNP33/2	2.5	1.2 MCHF + prolongation of He tank
CHOD	0.9	MGG-RPC
RICH	4.0	Indication
LKR	2.0	New supervision system + New Read-out
MAMUD	1.5	
SAC and IRC	0.4	
TRIGGER & DAQ	1.5	
TOTAL	24.0	

Table 17: Cost Estimation (Materials).

have identified most of the expertise needed to build and run the experiment. In particular we have identified the resources needed to launch the development of the Gigatracker, which

is the most innovative element and is essential to the design based on the unseparated kaon beam. This endeavour builds on the experience of the NA48 experiments. We believe to have found a fortunate combination, where a compelling physics case can be addressed with an existing CERN accelerator and employing a significant amount of infrastructure from an existing experiment. We stress that the new experiment is by no means a mere continuation of NA48 and that equipment investment of no less than 24 MCHF is needed to address the physics under study. Man-power, maintenance and operation, overheads and contingency may raise the total cost of the project towards 30 MCHF over 5 to 6 years. The working group setup more than a year ago has now evolved into a collaboration to which several new Institutions have joined. Some groups are already quite advanced in the process of requesting support from their Funding Agencies. We still seek the qualified participation of new groups. In particular we are negotiating the participation of the proponents of the CKM experiment at Fermilab which has not been ratified.

It is clear that, as far as running this experiment is concerned, there are already two approved competitors for beam time (filling LHC and running CNGS). The extent of the project proposed here leads us to request that there should be no further partitioning of beam time in ECN3 beyond these commitments at the time of data taking for this experiment. We understand that protons can be delivered for fixed target physics even when the LHC is being operated with ions. We request that these implications be taken into account when considering the project presented here. The tentative draft schedule of the experiment is indicated below:

- 2005
  - Launch GIGATRACKER R&D
  - Vacuum tests
  - Start Technical Design for the proposed detectors
  - Complete analysis of beam-test data
  - Complete specifications
  - Complete realistic cost estimation
- 2006
  - Tests in present K12 beam to validate choice of detectors
- 2007-2008

Construction, installation and tests of new beam (2007) and new detectors and new detectors (2007-2008)

- 2009-2010

Data Taking

## References

- [1] V. V. Anisimovsky et al. [E949 Collaboration], Phys. Rev. Lett. **93** (2004) 031801 [arXiv:hep-ex/0403036].
- [2] <http://www.phy.bnl.gov/e949/>
- [3] T. Komatsubara, T. Nakano and T. Nomura, Letter of Intent for Study of the Rare Decay  $K^+ \rightarrow \pi^+ \nu \bar{\nu}$  with Stopped Kaon Beam at J-PARC, <http://www-ps.kek.jp/jhf-np/L0Ilist/pdf/L04.pdf>
- [4] P.S. Cooper, Nucl. Phys. Proc. Suppl. **99B** (2001) 121;  
<http://www.fnal.gov/projects/ckm/Welcome.html>
- [5] M. Battaglia, A. J. Buras, P. Gambino and A. Stocchi (eds.),  
CERN report CERN 2003-002-corr [hep-ph/0304132].
- [6] A. J. Buras, F. Schwab and S. Uhling, arXiv:hep-ph/0405132.
- [7] W.J. Marciano and Z. Parsa, Phys. Rev. D **53** (1996) R1.
- [8] G. Buchalla and A. J. Buras, Nucl. Phys. B **398** (1993) 285; **400** (1993) 225; **412** (1994) 106 [hep-ph/9308272].
- [9] M. Misiak and J. Urban, Phys. Lett. B. **451** (1999) 161 [hep-ph/9901278].
- [10] L. Wolfenstein, Phys. Rev. Lett. **51** (1983) 1945.
- [11] G. Buchalla and A. J. Buras, Phys. Rev. D **54** (1996) 6782–6789.
- [12] G. D'Ambrosio and G. Isidori, Phys. Lett. B. **530** (2002) 108 [hep-ph/0112135].
- [13] L. Littenberg, Phys. Rev. D **39** (1989) 3322.

- [14] H.W. Atherton, et al.: Precise Measurements of Particle Production by 400 GeV/ $c$  Protons on Beryllium Targets, CERN Yellow Report: CERN 80-07 (1980).
- [15] G. Brianti, N. Doble: The SPS North Area High Intensity Facility: NAHIF, CERN/SPS/EA 77-2, CERN/SPSC/77-72, SPSC/T-18 (1977).
- [16] NA48/2 Collaboration, *Status Report on Experiment NA48/2*, CERN/SPSC-2003-033, SPSC-M-707, October 23, 2003.
- [17] C. Bovet, et al.: The CEDAR Counters for Particle Identification in the SPS Secondary Beams, CERN Report: CERN 82-13 (1982).
- [18] K.L. Brown, et al.: TRANSPORT, A Computer Program for designing Charged Particle Beam Transport Systems, CERN Report: CERN 80-04 (1980).
- [19] B. Hallgren, CEDAR readout using the LHCb TELL1 and 1 GHz ADC Mezzanine Board, NA48 Note 05-02, May 9, 2005.
- [20] K.L. Brown and Ch.Iselin: DECAY TURTLE, A Computer Program for simulating Charged Particle Beam Transport Systems, CERN Report: CERN 74-2 (1974).
- [21] Ch. Iselin HALO, A Computer Program to calculate Muon Halo, CERN Yellow Report: CERN 74-17 (1974).
- [22] M. Benedikt, R. Garoby (eds.): Report of the High Intensity Proton Working Group, CERN-AB-2004-022 OP/RF (2004).
- [23] P.Riedler et al., The ALICE Silicon Pixel Detector, Proceedings of the PIXEL2002 Conference, Carmel, USA, Sept.9-12,2002, SLAC Conference Proceedings C02/09/09.
- [24] P. Riedler et al., First Results from the ALICE Silicon Pixel Detector Prototype, Nucl. Instrum. Meth. A **501** (2003) 111–118.
- [25] M.Huhtinen, Nucl. Instrum. Meth. A **491** (2002) 194–215.
- [26] A.Kluge report from the Gigatracker WG meeting 5-4-2005.
- [27] M.Mota and J.Christiansen, “A High Resolution Time Interpolator Based on a Delay Locked Loop and an RC delay line”, IEEE Journal of Solid State circuits VOL.34 NO.10, October 1999, pp. 1360–1366.

- [28] B. Peyaud, “KABES: a novel beam spectrometer for NA48”, Draft paper of the 10<sup>th</sup> Vienna Conference on Instrumentation, Vienna (Austria), February 2004.
- [29] J. Frank et al., A Proposal for a Precision Measurement of the Decay  $K^+ \rightarrow \pi^+ \nu\bar{\nu}$  and Other Rare  $K^+$  Processes at Fermilab Using the Main Injector, June 2001.  
[http://www.fnal.gov/projects/ckm/documentation/public/proposal/ckm\\_proposal\\_2nd-edition2.7.pdf](http://www.fnal.gov/projects/ckm/documentation/public/proposal/ckm_proposal_2nd-edition2.7.pdf)
- [30] L. Littenberg, Not quite everything you always wanted to know about photon inefficiency, Kopio Technical note 071, Dec. 2003.
- [31] S. Ajimura et al., Measurements of the photon detection inefficiency of calorimeters between 185 and 505 MeV, Nucl. Instrum. Meth. A **435** (1999) 408.
- [32] A. Aloiso et al., Nucl. Instrum. Meth. A **482** (2002) 363.
- [33] A. Antonelli et al., Nucl. Instrum. Meth. A **354** (1995) 352.
- [34] A. Antonelli et al., Nucl. Instrum. Meth. A **370** (1996) 367.
- [35] G. Unal, Performances of the NA48 Liquid Krypton Calorimeter, Proceedings of the 9<sup>th</sup> International Conference on Calorimetry in High Energy Physics, Annecy, Oct. 2000, p. 355.
- [36] J. Ocariz, The NA48 Liquid Krypton Calorimeter Description and Performances, Proceedings of the 1998 IEEE Nuclear Science Symposium and Medical Imaging Conference, Toronto Nov 1998, p. 52.
- [37] G.S. Atoian et al., Development of Shashlyk Calorimeter for KOPIO, Nucl. Instrum. Meth. A **531** (2004) 467.
- [38] T. Nakano and Y. Kuno: A Study on Photon Detection Efficiency Using Real  $K_{\pi}2$  Data, E787 TN 256, 1993.
- [39] S. Ajimura, et. al., Nucl. Instrum. Meth. A **435** (1999) 408.
- [40] K. Lang et al. [BNL E871 Collaboration], Nucl. Instrum. Meth. A **522** (2004) 274. [arXiv:physics/0308047].
- [41] A. Placci, Private communication.

- [42] Y. Giomataris et al., Nucl. Instrum. Meth. A **376** (1996) 29–35.
- [43] Mota et al., A Flexible Multi-Channel High Resolution Time to Digital Converter ASIC, Nuclear Science Symposium, Lyon (France), October 2000.
- [44] KPLUS, April 2005 <http://www.fnal.gov/projects/ckm/documentation/public/ckm2-pac-apr04.pdf>
- [45] P. S. Cooper [the CKM Collaboration], "Redesign of the CKM RICH velocity spectrometers for use in a 1/4-GHz beam". FERMILAB-CONF-05-015-CD, prepared for the 5th International Workshop on Ring Imaging Cherenkov Detectors (RICH 2004), Playa de Carmen, Mexico, 30 Nov – 5 Dec 2004.
- [46] A. Akindinov et al., Nucl. Instrum. Meth. A **456** (2000) 16.
- [47] A. Akindinov et al., Nucl. Instrum. Meth. A **533** (2004) 74.
- [48] A. Akindinov et al., Nucl. Instrum. Meth. A **490** (2002) 58.
- [49] A. Akindinov et al., Nucl. Instrum. and Meth. A **533** (2004) 93.
- [50] A. Blanco et al., Nucl. Instrum. Meth. A **478** (2002) 170.
- [51] F. Aghinolfi et al., Nucl. Instrum. Meth. A **533** (2004) 183.
- [52] M. Mota, J. Christiansen, Proc. of 2000 Nucl. Science Symposium and Medical Imaging Conf., Lyon 15–20 Oct. 2000.
- [53] A. Akindinov et al., Nucl. Instrum. Meth. A **533** (2004) 178.